Theses and Dissertations

Theses and Dissertations

12-13-2008

Guest Intercalation Into Metal Halide Inorganic-Organic Layered Perovskite Hybrid Solids And Hydrothermal Synthesis Of Tin Oxide Spheres

Nilantha Bandara

Follow this and additional works at: https://scholarsjunction.msstate.edu/td

GUEST INTERCALATION INTO METAL HALIDE INORGANIC-ORGANIC

LAYERED PEROVSKITE HYBRID SOLIDS AND HYDROTHERMAL

SYNTHESIS OF TIN OXIDE SPHERES

By

Nilantha Bandara

A Thesis
Submitted to the Faculty of
Mississippi State University
in Partial Fulfillment of the Requirements
for the Degree of Master of Science
in Chemistry
in the Department of Chemistry

Mississippi State University, Mississippi

December 2008

GUEST INTERCALATION INTO METAL HALIDE INORGANIC-ORGANIC

LAYERED PEROVSKITE HYBRID SOLIDS AND HYDROTHERMAL

SYNTHESIS OF TIN OXIDE SPHERES

By

Nilantha Bandara

Approved:

_____   _____
Alicia M. Beatty   David O. Wipf
Assistant Professor of Chemistry   Professor of Chemistry
(Director of Thesis)   (Committee member)

_____   _____
William P. Henry   Stephen C. Foster
Associate Professor of Chemistry   Associate Professor of Chemistry
(Committee member)   (Graduate Coordinator)

_____
Gary L. Myers
Dean of the College of Arts and Sciences

Name: Nilantha Bandara

Date of Degree: December 12, 2008

Institution: Mississippi State University

Major Field: Chemistry

Major Professor: Dr. Alicia M. Beatty

Title of Study: GUEST INTERCALATION INTO METAL HALIDE INORGANIC-
ORGANIC LAYERED PEROVSKITE HYBRID SOLIDS AND
HYDROTHERMAL SYNTHESIS OF TIN OXIDE SPHERES

Pages in Study: 140

Candidate for Degree of Master of Science

The work presented in this thesis is divided into two research areas. In part I, the

synthesis and guest intercalation of inorganic-organic metal halide ammonium layered

perovskites is discussed. Comparisons are made between the solid matrix before and after

the intercalations, and all solids are characterized using thermogravimetric analysis

(TGA) and powder X-ray diffraction (XRD).

In part II, "template-free" hydrothermal synthesis of tin oxide spheres in the

presence of different *ortho*-substituted anilines is discussed. The aim is to determine

whether there are differences in the structures, shapes and surface morphology of the tin

oxide spheres that correspond to the identity/shape of the *ortho*-substituent on the

anilines. Solids were characterized by XRD, transmission electron microscopy (TEM)

and scanning electron microscopy (SEM) techniques.

DEDICATION

I would like to dedicate this research to the loving memory of my father,

Silmon Bandara Eraporuwa.

ACKNOWLEDGEMENTS

TABLE OF CONTENTS

LIST OF TABLES

LIST OF FIGURES

LIST OF ABBREVIATIONS

TGA   Thermogravimetric Analysis

XRD   Powder X-ray Diffraction

TEM   Transmission Electron Microscopy

SEM   Scanning Electron Microscopy

GS   Guanidinium-Sulfonate complexes

FPEA   Fluorophenethylammonium

PEA   Phenethylammmonium

UV   Ultra-Violet

BFI   Bright Field Images

SEI   Secondary Electron Images

SAD   Selected Area Diffraction

CHAPTER I

INTRODUCTION

1.1 Introduction

During the last few decades, the field of crystal engineering has grown tremendously, especially with the use of hydrogen bonding to create new structural frameworks.[1-3] Clays mimics and layered materials have been extensively studied[3-5] due to their potential for electronic,[6,7] magnetic,[8] optical,[9] and storage[10] properties. Inorganic-organic hybrid layered perovskites are an important class of crystalline materials with a range of possible applications such as transistors, semiconductors, catalysts etc.

Inorganic-organic hybrids are not new to Mother Nature. Shells, eggs, bones and teeth are known to be made of hybrids of inorganic crystalline phases {hydroxyapatite, $[Ca_{10}(PO_4)_6(OH)_2]$} and organic fibers (mainly proteins).[11] The bones can bend to some degree without breaking, and this is a fine example of an improved property in a hybrid, where the pure inorganic framework would be expected to be quite brittle, but addition of organic components allows flexibility. The nylon-layered silicate composite timing belt cover made by the Toyota Motor Company is also one of the innovative products of inorganic-organic hybrid on an industrial scale.[12] The work reported here involves metal-halide anionic layers and organo-ammonium cations, where the organic substituents are located between layers.

1

1.2 Supramolecular chemistry and crystal engineering

From the days of Johannes van der Waals (1870's), weak, non-covalent bonds were of much interest for researchers.[13] Especially in the 1950's weak interactions began to be used as building blocks for intermolecular structures, with the synthesis of ion-specified crown ethers.[14] That work was followed by cryptand[15,16] and spherand[17] types of assemblies. A new field of chemistry was developed around non-covalent interactions and was internationally recognized by awarding the 1987 Nobel Prize in Chemistry to Pedersen,[18] Cram,[19] and Lehn.[20]

Cram called this new field host-guest chemistry,[21] while Lehn addressed the broader topic as Supramolecular chemistry.[16] A "Supermolecule" is a species that is held by non-covalent interactions between two or more covalent molecules or ions.[1] Supramolecular chemistry is known as the chemistry beyond the molecule.[22] "Molecular self assembly", "molecular recognition", "host-guest chemistry" and "supramolecular synthon" are a few of novel concepts donated to the world from the field of supramolecular chemistry.[23] Supramolecular chemistry is a rapidly growing research field, especially with more research diverted towards mimicking the properties of natural occurring systems, e.g. clay mimics.

Crystal engineering is a subset of solid state supramolecular chemistry. The field of crystal engineering started with the organic solid state photochemistry work of G. M. Schmidt in 1971.[24] The photodimerization of double bonds in cinnamic acids molecules, which were held together in close proximity by the crystalline lattice, led to the beginning of a new era in chemistry.

2

The aim of crystal engineering is to control molecular assembly or network assembly (coordinate polymers) in the solid state, and to determine structure-function relationships. Therefore the crystal engineer often focuses on molecular approaches to designing new materials with desired properties through control over the structure. The modern definition of crystal engineering was given by Gautam Desiraju as "the understanding of intermolecular interactions in the context of crystal packing and the utilization of such understanding in the design of new solids with desired physical and chemical properties."[1]

Crystal engineering involves generating crystalline solid networks with various dimensionalities (1-D, 2-D, or 3-D). The work described here is based on layered perovskite inorganic/organic hybrid, so the focus was directed to synthesizing 2-D layered crystals.

1.3 Clays/Layered materials

Supramolecular concepts such as self assembly and molecular recognition have been used to develop layered materials with infinite 2-D networks. Over the years these structural networks were developed using two main bonding strategies; hydrogen bonding and coordination covalent bonding.[13,25] These layered materials have been termed "clay mimics".[4]

Natural occurring clays contain two types of structural arrangements; bilayers (ABA) and alternating layers (AB).[4,26] In the literature there are many hydrogen bonded two-dimensional lamellar structures. However, these clay mimics differ from the actual

clay materials, where the natural systems posses coordinate covalent bonds holding

together an anionic layer, with alkali metal cations and water located in the interlayer

(purely inorganic).[26] Clay mimics are built from both inorganic and organic components.

Layered organic networks made from complementary hydrogen-bonded

functionalities were first reported by Ward and co-workers in 1994 with the guanidinium-

sulfonate (GS) complexes.[27] The (guanidinium)N—H$\cdots$O(sulfonate) hydrogen bonds

provided self assembled, robust 2-D networks with the general formula of

$[C(NH_2)_3]^+RSO_3^-$.[28] Single layer and bilayered arrangements were found with these

networks and the size of the pendent organic group was the deciding factor for the

different packing behaviors, Fig. 1.1.[27,28]

(a)   (b)
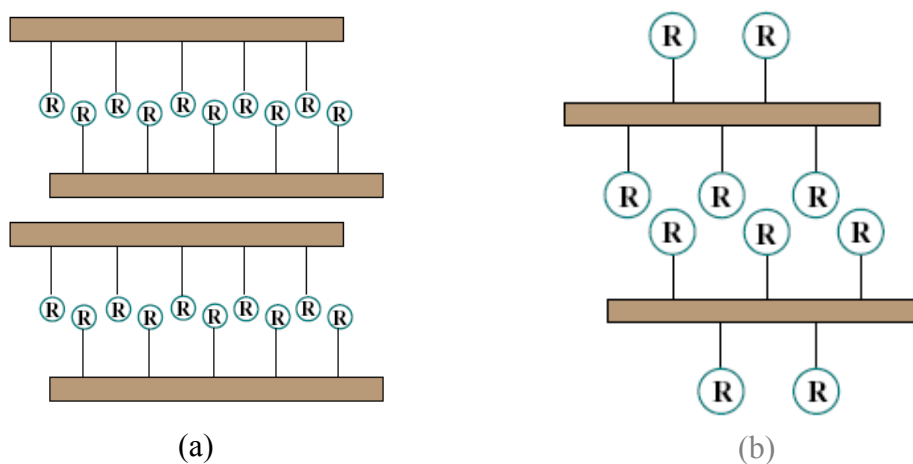
Figure 1.1   (a) Bilayer arrangement observed with small R groups, (b) single layer
arrangements observed with large R groups.[27,28]

Beatty and coworkers reported a series of organic clay mimics using 3,5-

pyrazoledicarboxylic acid with different aryl and alkyl mono amine systems.[4] The

structures containing primary ammonium ions exhibited ABA bilayer assemblies, and a

secondary ammonium cation led to an AB pattern. The sheets were obtained by carboxylic acid-carboxylate and ammonium-carboxylate hydrogen bonds, and the interlayer distance was controlled by the size of pendent group in the organic amine. Most of the structures showed an interdigitated arrangement, but some of the aryl pendent groups gave parallel arrangements, Fig. 1.2.[4]

(a)   (b)
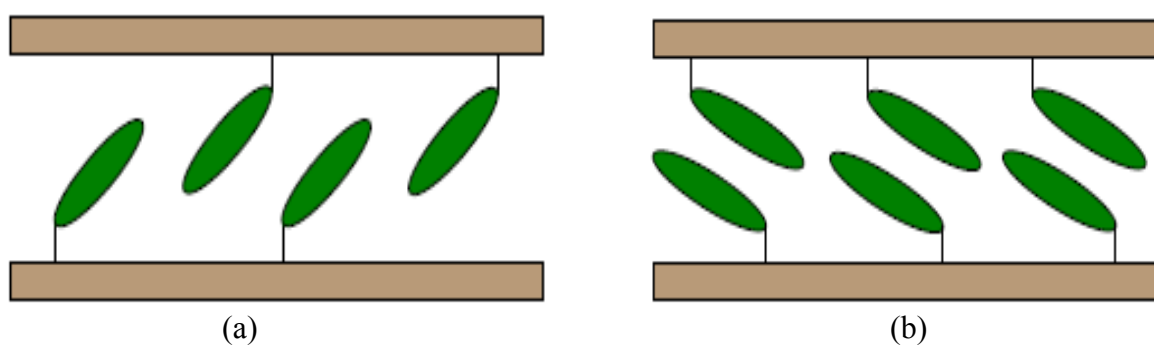
Figure 1.2   (a) Interdigitated arrangement, (b) parallel arrangement observed in aryl pendent groups.

(a)   (b)
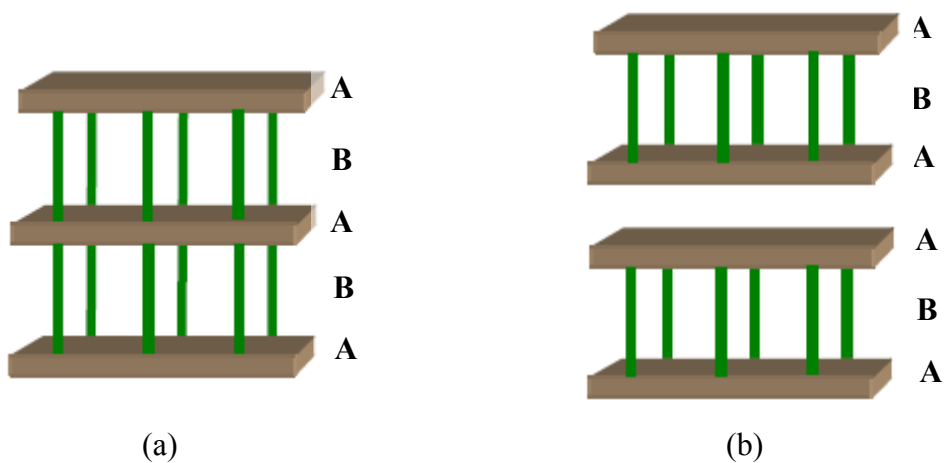
Figure 1.3   (a) Alternating layer (AB) and (b) bilayer (ABA) arrangements of pillared clay mimics.[4,26]

5

Beatty's group also used coordination compounds containing peripheral carboxylic acid substituents in combination with amines to synthesize 2-D inorganic/organic layers with, Ni(II) and Co(II) as the metal centers.[5] Charge assisted carboxylic acid-carboxylate and ammonium-carboxylate hydrogen bonds provided strong hydrogen-bonds to make a stable layered architecture. The packing of the interlayer was dictated by the nature of the primary amine used. The phenyl organic moieties were interdigitated, but a long carbon chain (e.g. octyl groups) gave a parallel arrangement.[5]

      (a)   (b)
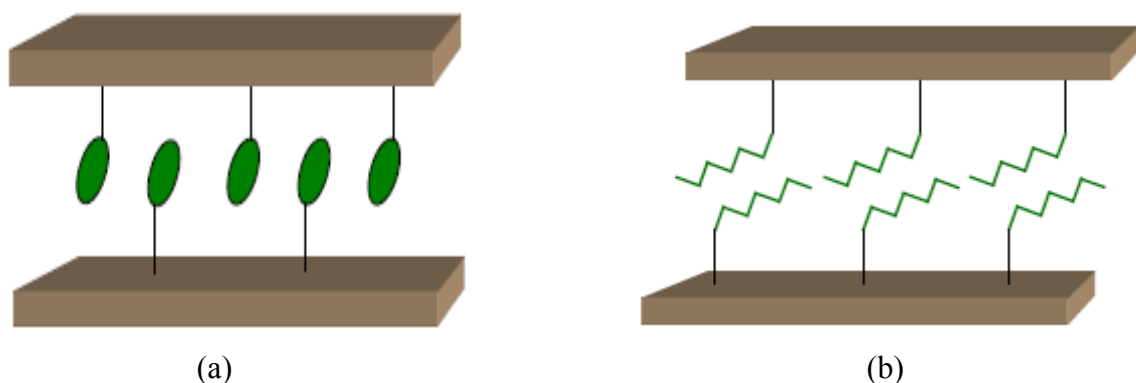
Figure 1.4   (a) Interdigitated arrangement of phenyl groups and (b) parallel arrangement of long chain groups.

Coordination polymers, with coordinate-covalent bonds in place of hydrogen bonds, have also been used to create layered crystalline architectures.[3] Clearfield and coworkers were the pioneers in using metal phosphonates (the phosphonates having organic substituents) to create inorganic/organic hybrid layered structures linked by coordinate-covalent bonds.[29] Several metal ions were used in their research, and zirconium phosphonate systems were the most successful in producing stable layered pillared structures.

6

1.4 Inorganic-organic perovskites

Inorganic-organic perovskites are the most common hybrid crystal structures, with their integrated characteristics of both inorganic and organic properties in a single composite.[30] Our interest on this unique class of materials was based on their storage capabilities and the possibility of intercalating guest molecules. Mitzi et al. of IBM have studied layered hybrid perovskite materials extensively.[6,30,31] These materials show unique electronic and optical properties.[6,32-34] The organic moieties between the hydrophilic layers create a hydrophobic interlayer, and organic guest species such as benzene can be co-crystallized between layers.

The structure of the inorganic/organic perovskites is as follows: the anionic inorganic layer is interconnected by corner sharing metal halide octahedra.[6] The organic species should be cationic to balance the charge, and in the case of ammonium counterions they can form hydrogen-bonds with the layer. The solids have the general formula $[(R-NH_3)_2]^{2+}[MX_4]^{2-}$, where $R-NH_3^+$ is an aliphatic or aromatic ammonium cation. With di-ammonium groups, the general formula is $[(NH_3-R-NH_3)]^{2+}[MX_4]^{2-}$, and the cations connect the inorganic layers as pillars, Fig. 1.5.[30]
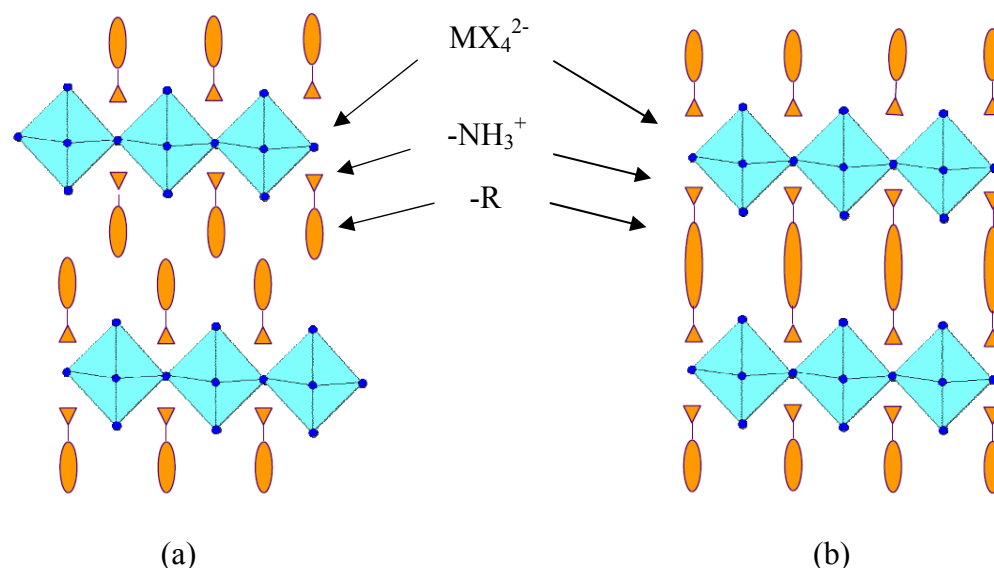
Figure 1.5   Layered perovskites (a) monoammonium (b) diammonium; X^- is
the halides and -NH_3^+ represents the ammonium counter-ions.[30]

The size of the pendant R group dictates the interlayer distance and the flexibility

of the structure. The organic interlayer is completely hydrophobic and it would be an

ideal place to store small organic molecules, if there is enough flexibility in the interlayer

to allow incorporation of guest molecules.

The work reported here is based on the (phenethylammonium)$_2$MX$_4$ family of

inorganic-organic perovskite layered compounds, where both the metal and the halide can

be varied.[30,35] The first structure of this group was reported by Willet in 1990.[36] A

phenethylammonium tin iodide perovskite was reported by Papavassiliou and coworkers

in 1994.[37] A cadmium chloride analogue was reported by Salah and coworkers.[38]
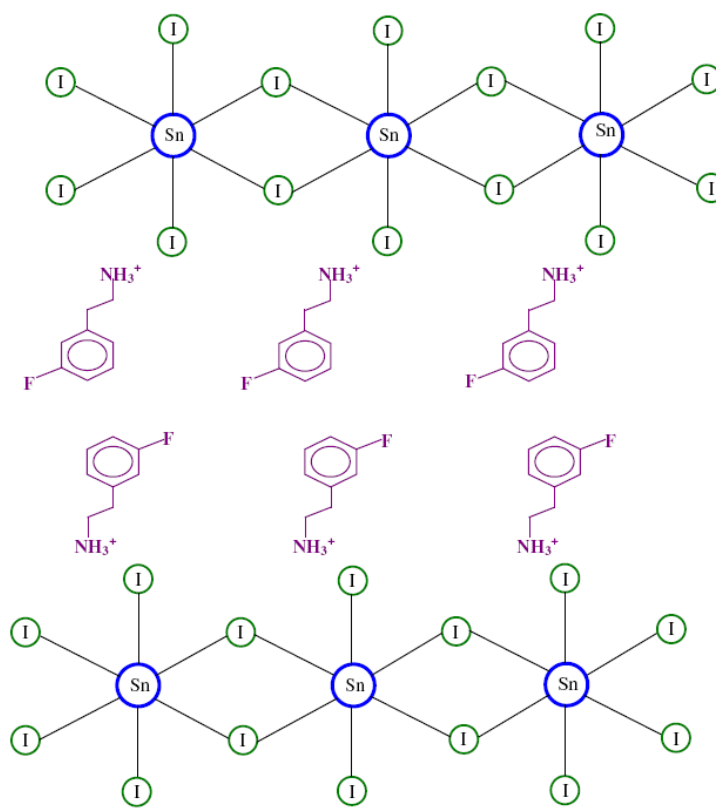
Figure 1.6   The structure of (3-FPEA)$_2$SnI$_4$ perovskite[39]

In this research, attempts to determine the mobility of molecules and/or ions between layers (i.e. intercalation) of these layered networks was explored and the results are reported in later chapters. Intercalation is described below.

1.5 Intercalation chemistry

Intercalation is the process of inserting guest molecules or ions into a pre-existing host system. Although intercalation is closely related to molecular encapsulation, inclusion compounds and co-crystallization, it differs from all of these because, in order for intercalation to occur, two conditions need to be satisfied:

- There should be a solid structure maintained, into which small molecules or ions can move. The structure should be strong enough to withstand disruption by incoming guest molecules or ions.

- The guest should have attractive interactions with the interlayer in order to provide a driving force for the guest to move into the host solid. In clays, the intercalates are water and ions (hydrophilic). In clay mimics the intercalates should be small organic molecules (hydrophobic).

        (a)   (b)
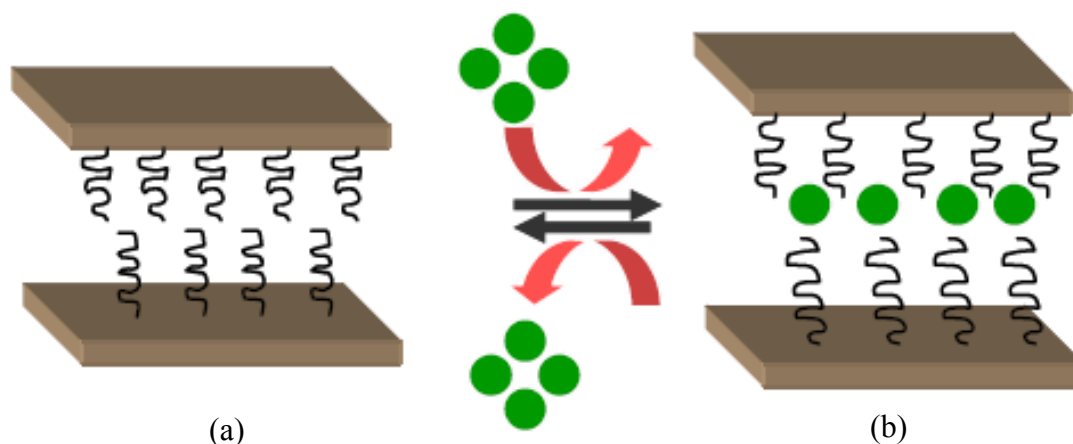
Figure 1.7   Schematic diagram representing the intercalation process (a) host system (b) host-guest complex (layers expanded to accommodate guests)

The earliest examples of intercalations involve 3-D rigid host structures with pores or channels through which guest molecules or ions travel. Zeolites are the most obvious example, where the host structures are aluminosilicate inorganic frameworks. Zeolites, like clays, can be used as catalytic agents for separation of crude oil in petroleum industry and as water softening agents in detergents and so on.[40]

Synthetic materials have been created in order to mimic the structures of natural compounds, and molecular transport in and out of porous solids has been an interesting topic in the last few decades.[22,23,41,42] For example, Kepert and Rosseinsky synthesized a zeolite-like crystal framework that retains an open framework geometry in both the solvated and desolvated forms.[43] This coordination polymer framework, $Ni_2(4,4'$-bipy)$_3(NO_3)_4$, shows remarkable structural stability upon reversible ethanol guest insertion.

In the absence of a 3-D framework, guest insertions occur with framework flexibility (e.g. graphite). The goal of the research reported here is to investigate whether hydrogen-bonded clay mimics can actually function as clays. That is, can inorganic-organic metal halide/ammonium layered networks favor the insertion of organic molecules?

1.6 Intercalation in perovskite structures

In mono-ammonium perovskites, the organic cations have weak van der Waals interactions. These van der Waals forces may be weak enough to allow the insertion of guest molecules, especially hydrophobic guests. However, then the guest molecules need to create stronger intermolecular interactions between layers than the original host, so that the driving force for intercalation exists.

(a)   (b)
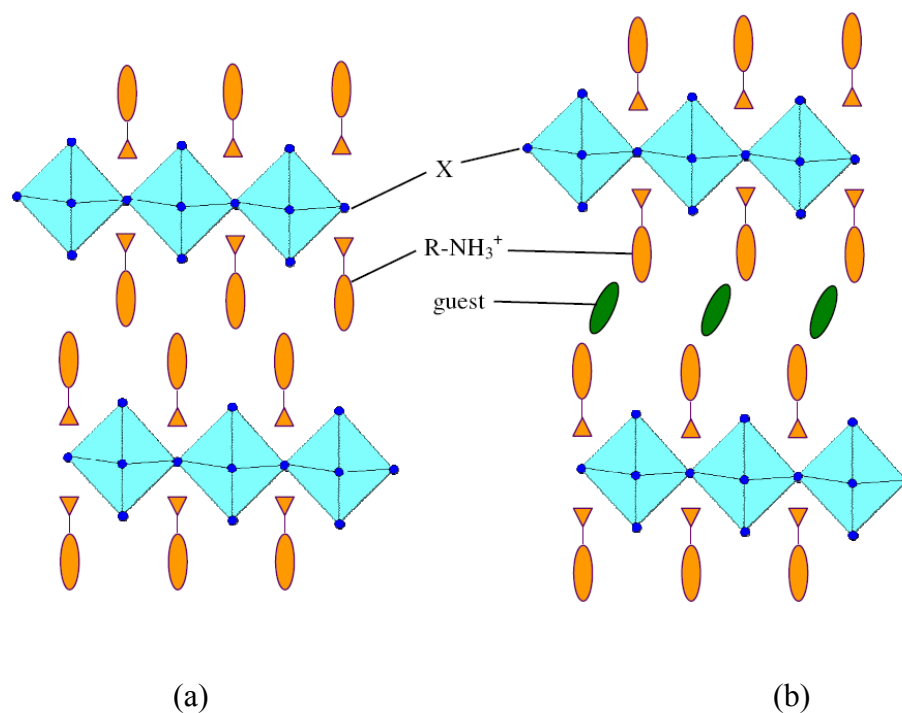
Figure 1.8   Crystal structures of momo-ammonium perovskite; (a) host only,
              (b) host-guest complex[44] (guest insertion with layer expansion)

Over the years only one report was found regarding guest co-crystalization in perovskite networks. In 2002, Mitzi and coworkers successfully incorporated benzene and hexafluorobenzene organic molecules into phenethylammonium perovskite lattices.[44] Here, the perovskite lattice crystallized around the guest species, so the guest was not transported into a solid, it was co-crystallized with the host from solution. This is not intercalation, but co-crystallization. They observed guest removal without the destruction of the host lattice through heating. However, reversible incorporation of guest molecules into the solid framework has yet to be discovered with the perovskite crystals.

The point of the research is to use the above-mentioned tin iodide and cadmium chloride layered structures to determine whether reversible guest intercalation can occur. The solids were analyzed by powder X-ray diffraction before and after intercalations, and thermogravimetric analysis (TGA) and transmission electron microscopy (TEM) analyses were also performed, and will be described in the following chapters.

REFERENCES

(1) Desiraju,   G. R. *Angew. Chem., Int. Ed.* **1995**, *34*, 2311-2327.

(2) Beatty,   A. M. *CrystEngComm* **2001**, *51*, 1-13.

(3)   Zaworotko, M. J. *Chem. Commun.* **2001**, 1-9.

(4)   Beatty, A. M.; Granger, K. E.; Simpson, A. E. *Chem. Eur. J.* **2002**, *8*, 3254-3259.

(5)   Beatty, A. M.; Helfrich, B. A.; Hogan, G. A.; Reed, B. A. *Cryst. Growth Des.* **2006**, *6*, 122-126.

(6)   Mitzi, D. B. *Prog. Inorg. Chem.* **1999**, *48*, 1-121.

(7)   Thylen, L.; Qiu, M.; Anand, S. *ChemPhysChem* **2004**, *5*, 1268-1283.

(8)   Batten, S. R.; Murray, K. S. *Coord. Chem. Rev.* **2003**, *246*, 103-130.

(9)   Shin, D. M.; Lee, I. S.; Chung, Y. K. *Eur. J. Inorg. Chem.* **2003**, 2311-2317.

(10)   Nassimbeni, L. R. *Acc. Chem. Res.* **2003**, *36*, 631-637.

(11)   Currey, J. D. *J. Mater. Educ.* **1987**, *9*, 120.

(12)   Kurauchi, T. O., A.; Nomura, T.; Nishio, T.; Saegusa, S.; Degushi, R., In *SAE International Technical Paper Ser., 910584,* 1991.

(13)   Desiraju, G. R.; Editor; John Wiley & Sons, Ltd: London, 2003.

(14)   Pedersen, C. J. *J. Am. Chem. Soc.* **1967**, *89*, 7017-7036.

(15)   Dietrich, B.; Lehn, J. M.; Sauvage, J. P. *Tetrahedron Lett.* **1969**, 2889-2892.

(16)   Lehn, J. M. *Angew. Chem., Int. Ed.* **1990**, *29*, 1304-1319.

(17)   Trueblood, K. N.; Knobler, C. B.; Maverick, E.; Helgeson, R. C.; Brown, S. B.; Cram, D. J. *J. Am. Chem. Soc.* **1981**, *103*, 5594-5596.

(18)   Pedersen, C. J. *Angew. Chem. Int. Ed.* **1988**, *27*, 1021-1027.

(19) Cram   , D. J. *Angew. Chem. Int. Ed.* **1988**, *27*, 1009-1020.

(20)   Lehn, J. M. *Angew. Chem. Int. Ed.* **1988**, *27*, 89-112.

(21)   Cram, D. J.; Cram, J. M. *Science* **1974**, *183*, 803-809.

(22)   Steed, J. W.; Turner, D. R.; Wallace, K. J. *Core Concepts in Supramolecular Chemistry and Nanochemistry*; John Wiley & Sons, Ltd.: Chichester, UK, **2007**.

(23)   Müeller, A.; Reuter, H.; Dillinger, S. *Angew. Chem. Int. Ed.* **1995**, *34*, 2328-2361.

(24)   Schmidt, G. M. J. *Pure Appl. Chem.* **1971**, *27*, 647-678.

(25) Beatty,   A. M. *Coord. Chem. Rev.* **2003**, *246*, 131-143.

(26)   Beatty, A. M.; Schneider, C. M.; Simpson, A. E.; Zaher, J. L. *CrystEngComm* **2002**, *4*, 282-287.

(27)   Russell, V. A.; Etter, M. C.; Ward, M. D. *J. Am. Chem. Soc.* **1994**, *116*, 1941-1952.

(28)   Russell, V. A.; Ward, M. D. *J. Mater. Chem.* **1997**, *7*, 1123-1133.

(29) Clearfield,   A.; Wang, Z. *J. Chem. Soc., Dalton Trans.* **2002**, 2937-2947.

(30)   Mitzi, D. B. *J. Chem. Soc., Dalton Trans.* **2001**, 1-12.

(31)   Mitzi, D. B. *J. Mater. Chem.* **2004**, *14*, 2355-2365.

(32)   Zhu, X.-H.; Mercier, N.; Riou, A.; Blanchard, P.; Frere, P. *Chem. Commun.* **2002**, 2160-2161.

(33)   Arend, H.; Tichy, K.; Baberschke, K.; Rys, F. *Solid State Commun.* **1976**, *18*, 999-1003.

(34)   Chakravarthy, V.; Guloy, A. M. *Chem. Commun.* **1997**, 697-698.

(35)   Mitzi, D. B. *J. Solid State Chem.* **1999**, *145*, 694-704.

(36)   Willett, R. D. *Acta Crystallogr., Sect. C* **1990**, *C46*, 565-568.

(37)   Papavassiliou, G. C.; Koutselas, I. B.; Terzis, A.; Whangbo, M. H. *Solid State Commun.* **1994**, *91*, 695-698.

(38)   Groh, M.; Spengler, R.; Burzlaff, H.; Zouari, F.; Salah, A. B. *Acta Crystallogr., Sect. C* **1997**, *C53*, 1199-1201.

(39)   Mitzi, D. B.; Dimitrakopoulos, C. D.; Kosbar, L. L. *Chem. Mater.* **2001**, *13*, 3728-3740.

(40)   Lee, J. D. *Concise Inorganic Chemistry. 4th Ed*; Blackwell Science Ltd: Oxford, **1991**.

(41)   Atwood, J. L.; Barbour, L. J.; Jerga, A.; Schottel, B. L. *Science* **2002**, *298*, 1000-1002.

(42)   James, S. L. *Chem. Soc. Rev.* **2003**, *32*, 276-288.

(43)   Kepert, C. J.; Rosseinsky, M. J. *Chem. Commun.* **1999**, 375-376.

(44)   Mitzi, D. B.; Medeiros, D. R.; Malenfant, P. R. L. *Inorg. Chem.* **2002**, *41*, 2134-2145.

CHAPTER II

EXPERIMENTAL DETAILS & RESULTS

2.1 Experimental details

This chapter is devoted to the experimental details of the intercalation study. The sections include a description of the synthesis of the layered hosts, a description of the intercalation experiments, and descriptions of the analytical methods and results.

2.1.1 Materials and methods

All amines and metal halides were purchased from Sigma-Aldrich, as were the anhydrous solvents. Hydroiodic acid (57%) was purchased from Aldrich and degassed by the freeze-pump-thaw method. Titanium tetrachloride was purchased from Alfa-Aesar. The tin iodide was weighed and loaded into Schlenk flasks in a dry box. All syntheses for tin iodide and cadmium chloride were carried out in an argon atmosphere using a Schlenk line. Anhydrous solvents were used as-is directly from the sure seal bottle and injected into Schlenk tubes using Sigma-Aldrich SGE gas tight syringes.

Comparisons were made between the solid layered host before and after the intercalation experiments. All products were characterized using thermogravimetric analysis (TGA) and powder X-ray diffraction (XRD) techniques.

2.1.2 Preparation of tin iodide host materials

The tin iodide perovskite crystals were obtained by slow cooling of the saturated metal halide ammonium mixture in an inert atmosphere. The synthesis of (4-fluorophenethylammonium)$_2$SnI$_4$ [(4-FPEA)$_2$SnI$_4$] (**1**), [(3-FPEA)$_2$SnI$_4$] (**2**) and [(2-FPEA)$_2$SnI$_4$] (**3**) were performed according to the published method.[1] For the early trials of synthesis, approximately 0.1-0.3 mmol of starting material was used. After reproducing the crystals with substantial yields (>90%), the reaction was scaled up by a factor of 10.

Example reaction: 1.118 g of SnI$_2$ (3 mmol, anhydrous beads, 99.999%) in 10 mL of anhydrous 2-butanol was allowed to react with with 6 mmol of 4-fluorophenethylamine (99%, 0.79 mL) in a Schlenk flask in argon atmosphere. The system was cooled down using an ice/salt bath to approximately -5 $^{\circ}$C. About 2 mL of degassed HI (57 wt %) was slowly added using a syringe. The system was thoroughly mixed and then heated above 90 $^{\circ}$C until all the starting materials were dissolved. This saturated solution was cooled slowly to obtain brown/red crystals of **1**.[1] The reaction scheme is shown in Fig. 2.1.

tin iodide   4-FPEA   (4-FPEA)$_2$SnI$_4$ layered perovskite
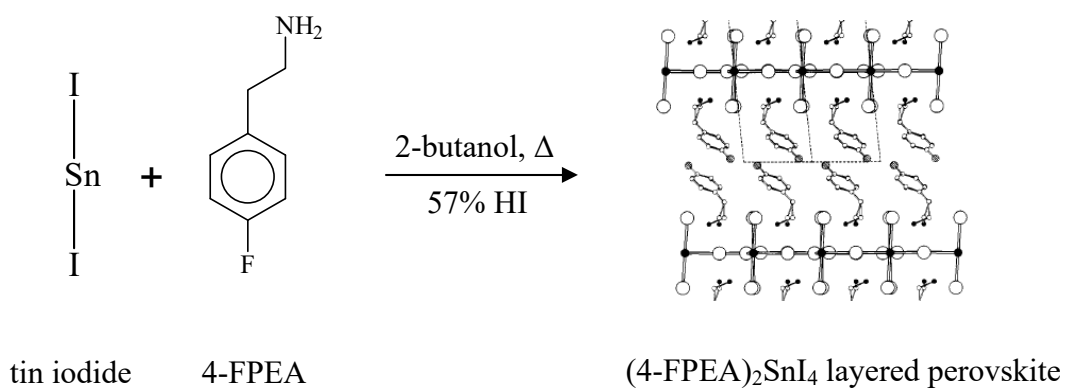
Figure 2.1 The reaction scheme for **1**.

The cooling rate used in the literature preparation was 3 $^{\circ}$C/h. In our lab, it was necessary to adjust the flow rate of argon and heating and cooling rates manually through a series of trial and error attempts to determine the most suitable conditions. The crystals were washed with CHCl$_3$ to remove starting materials. The purity of the products was tested using TGA and powder X-ray. The dried products were stored in an argon atmosphere.

The syntheses of other phenethylammmonium tin iodide compounds were performed following the procedure above with adjustment of the solvent amounts, Table 2.1.

Table 2.1

Synthesis of phenethylamine tin halide perovskites

Product	Amines	Hydroiodic acid	2-butanol
2	3-fluorophenethylamine	1 mL	6 mL
3	2-fluorophenethylamine	1 mL	6 mL
4	phenethylamine	2 mL	10 mL
5	2-(2-Chlorophenyl)-ethylamine	1 mL	6 mL
6	2-(4-Chlorophenyl)-ethylamine	2 mL	10 mL

The synthesis of tin iodide metal compounds with unbranched alkyl amines also attempted. The syntheses involving hexylamine, octylamine, decylamine and tetradecylamine did not give crystalline products. However, crystalline products were obtained when dodecylamine and octadecylamine were used as starting materials, Table 2.2.

Table 2.2

Synthesis of long chain primary amine tin halide perovskites

Product	Amines	Hydroiodic acid	2-butanol
7	Dodecylamine	2 mL	10 mL
8	Octadecylamine	2 mL	15 mL

The preparation of tin iodide perovskites was performed according to the following reaction:

$$SnI_2 + 2RNH_2 \xrightarrow[\text{HI}]{C_4H_8OH} (RNH_3)_2SnI_4$$

The following variables apply: R = C_8H_8F (**1-3**), C_8H_9 (**4**), C_8H_8Cl (**5,6**), $C_{12}H_{25}$ (**7**) and $C_{18}H_{37}$ (**8**).

Attempts were also made to create mixed amine perovskite systems. Instead of 1:2 metal : amine ratio, we used 1:1:1, meatal:long chain amine:short chain amine systems. Octadecylamine and dodecylamine were used as the long chain systems and octylamine and hexylamine were used as the short chain amines. Crystalline products were not obtained for any of these reactions.

A number of attempts were conducted to synthesize novel tin iodide diammonium perovskites with a number of different diamines, solvents, and co-solvents. However, no crystalline products were observed. The conditions used are listed in Table 2.3.

Table 2.3

Reactions involved in attempted synthesis of diammonium tin halide
perovskites

Diammine	Solvent	Co-solvents
1,4-diaminobutane	57% HI	none
3,3-dimethoxybenzidine	57% HI	none
3,3-dimethoxybenzidine	conc. HCl	none, MeOH
3,3-dimethoxybenzidine.dichloride	conc. HCl	MeOH
4,4-diaminostilbene	57% HI	none
4,4-diaminostilbene	conc. HCl	MeOH
4,4-ethylenedianiline	57% HI	none, MeOH, CH$_3$CN
4-aminophenylethylamine	57% HI	none, C$_6$F$_6$, DMSO
benzidine	57% HI	CH$_3$CN, THF, DMSO, 2-butanol
benzidine	conc. HCl	MeOH
p-xylenediamine	57% HI	none, MeOH , CH$_3$CN

The tin iodide perovskite products reacted with atmospheric oxygen and humidity
and therefore were kept under inert conditions at all times. The shiny red crystalline
product, when subjected to ambient conditions, became discolored within 5-7 days and a
black residue remained. Therefore, all reactions and intercalations involving the tin
iodide perovskites were performed with anhydrous solvents and in inert atmosphere.

2.1.3 Preparation of cadmium chloride perovskites

Cadmium chloride/ammonium perovskite crystals were obtained by slow evaporation and slow cooling techniques, as described below.

Slow evaporation: $CdCl_2$ (0.2 mmol) was completely dissolved in methanol (2 mL) with approximately 3 drops of concentrated HCl (37%). A clear solution was obtained after half an hour of stirring without heat. The primary amines (0.4 mmol) were directly added to the system and stirred another one hour until a clear solution was observed. The clear reaction filtrate was covered with paraffin film with a few holes and allowed to slowly evaporate. Crystals were obtained after 2-3 weeks. In this method, 15 different amines were used with $CdCl_2$ but only 5 systems gave crystalline products: $(C_6H_{16}N)_2CdCl_4$ (**9**), $(C_{10}H_{24}N)_2CdCl_4$ (**10**), $(C_{12}H_{28}N)_2CdCl_4$ (**11**), $(C_{14}H_{32}N)_2CdCl_4$ (**12**), and $(C_{18}H_{40}N)_2CdCl_4$ (**13**). These products were achieved from hexylamine, decylamine, dodecylamine, tetradecylamine, and octadecylamine.

The cadmium chloride perovskite products were stable compared to the tin iodides; they did not show any deterioration even with prolonged storage at ambient conditions.

To obtain bulk products of **9-13**, a *slow cooling* method was applied: $CdCl_2$ (1 mmol) was allowed to react with 2 mmol of alkyl amine in 10 mL of anhydrous 2-butanol. About 1 mL of concentrated HCl was added drop wise and the system was thoroughly mixed and heated above 70 ^{o}C until all the starting materials were dissolved. This saturated solution was cooled down slowly to obtain colorless/white crystals.

2.1.4 Intercalation experiments

A *Branson* 1510 1.91L capacity ultrasonic cleaner with 40 kHz frequency was used as the sonicator (Fig. 2.2(a)) for the intercalation experiments. In these experiments, 0.1 g of ground perovskite powder sample was placed in a glass vial with 1.0 ml of a guest and 10.0 mL of solvent (the host solid is not soluble in the solvents). The vials were then placed in the sonicator for 90 min, 3 h, 6 h, 8 h and 16 h time durations (Fig. 2.2(b)). A complete list of solvents and guest molecules are shown in Table 2.4.

(a)   (b)

Figure 2.2   The Branson sonicator (a) and the samples after sonication (b).

Table 2.4 Intercalation experiments for **1**-**8** and **11**

Product	Solvents	Guests
1-6	toluene cyclohexane hexane	benzene 1,2-difluorobenzene 1,4-difluorobenzene hexafluorobenzene benzotrifluoride 1,2-dichlorobenzene 2-chlorophenol
7, **8**	pentane hexane	hexane heptane octane octanol octylcyanide decane decanol
11	pentane hexane	hexane heptane octane octanol decane

The sonicated samples were then analyzed in two ways: to obtain XRD patterns a small amount of the sonicated sample was removed from the sonicating tube via pipette and applied directly to zero-background slides. To obtain TGA graphs the remaining sample was isolated by decanting the solvent/guest solution, rinsed with toluene and dried for 4 h. The samples were rinsed with toluene in order to remove any guest molecules that may have remained on the surface of the solid so that the weight differences upon conducting the TGA experiment were not skewed by the presence of surface "guest" molecules.

2.1.5 Thermogravimetric analysis

About 20 mg of the dry solid was used for the TGA experiments. The instrument used was a Perkin Elmer TGA 7 (Fig. 2.3(a)). The samples were run in an argon atmosphere. The rate temperature increase was 5 ^{o}C/min, over a temperature range of 25 ^{o}C to 550 ^{o}C. Starting materials and the sonicated samples were analyzed to compare the relative weight losses. These studies were repeated several times to ensure that the results were reproducible.

(a)   (b)

Figure 2.3   (a) Perkin Elmer TGA 7 and (b) Siemens D5000 X-ray diffractometer

2.1.6 Powder X-ray analysis

A *Siemens* D5000 X-ray diffractometer (Fig. 2.3(b)) with zero-background sample holders was used to examine the sonicated and non sonicated samples. For each sample two types of scans were performed. One overall scan with 2 mm slit and a 1 s step time for a range of 4° to 50° 2θ was performed in order to confirm the identity of the compound. A longer scan (5-8 s step time) was performed in the range of 4° to 20° using either 0.6 mm or 0.1 mm slits. Compounds **7-13** were scanned starting from 3° 2θ.

Initially a dry packing method was used in depositing the solids onto the sample holder. However, this method gave a high signal to noise ratio. Therefore, a "wet packing" method was used, where sonicated samples were applied directly to the sample holder using a glass pipette without a sample loss. The amount of sample needed for the testing also was significantly smaller, and the signal/noise improved significantly using this method.

2.1.7 TEM analysis

In order to further probe the products of the reactions, TEM was used to analyze the products of **2** sonicated with benzene, 1,4-difluorobenzene and hexafluorobenzene in toluene. Bright field images were taken at 10,000× and 20,000× magnifications from the JEOL JEM 100 CX II instrument with an excitation voltage of 100 kV.

2.2 Results

2.2.1 Powder X-ray results for starting materials (before sonication)

Powder X-ray was used to identify and/or characterize the products of the reactions describe in section 2.1.2. Using tin iodides with different amines the (4-FPEA)$_2$SnI$_4$ (**1**), (3-FPEA)$_2$SnI$_4$ (**2**), (2-FPEA)$_2$SnI$_4$ (**3**), (PEA)$_2$SnI$_4$ (**4**), (4-ClPEA)$_2$SnI$_4$ (**5**), (2-ClPEA)$_2$SnI$_4$ (**6**), (C$_{12}$H$_{28}$N)$_2$SnI$_4$ (**7**) and (C$_{18}$H$_{40}$N)$_2$SnI$_4$ (**8**) layered perovskites were synthesized. The XRD patterns for these samples are shown in Fig. 2.4.
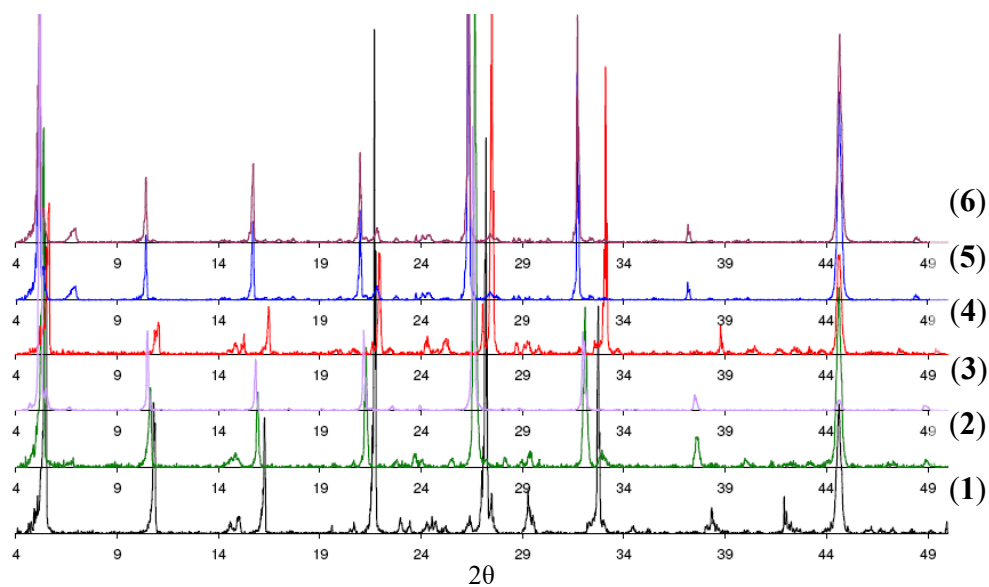

Figure 2.4   Powder X-ray patterns for **1**, **2**, **3**, **4**, **5** and **6** 4° to 50° in 2θ angle, 1 s step time, 2 mm sample slit.

XRD patterns were also collected for the cadmium chloride/alkylamine reactions. The XRD patterns for (C$_6$H$_{16}$N)$_2$CdCl$_4$ (**9**), (C$_{10}$H$_{24}$N)$_2$CdCl$_4$ (**10**), (C$_{12}$H$_{28}$N)$_2$CdCl$_4$ (**11**),

$(C_{14}H_{32}N)_2CdCl_4$ (**12**) and $(C_{18}H_{40}N)_2CdCl_4$ (**13**) perovskites products are listed in Fig. 2.5.
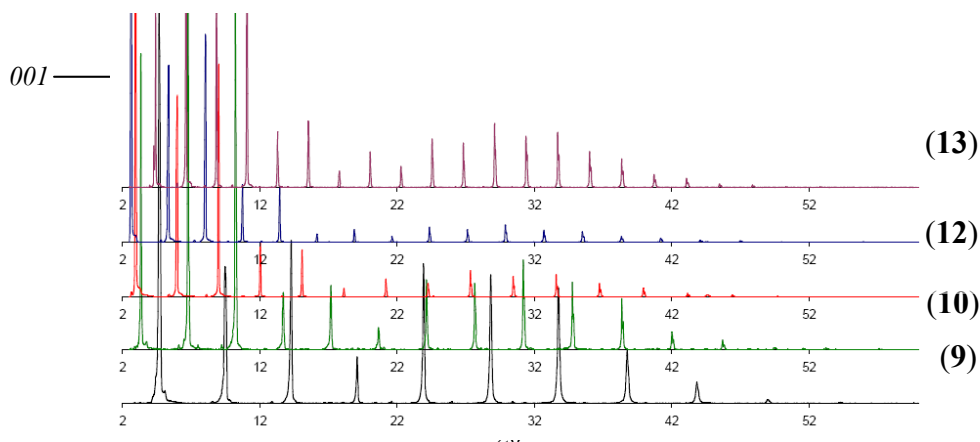

Figure 2.5   Powder X-ray pattern for **9**, **10**, **11**, **12** and **13** $3°$ to $60°$ in 2θ angle, 8 s step time, 0.6 mm sample slit.

The patterns show an increase in the interlayer distance from **9-13**, as can be seen with the decreasing 2θ value (corresponding to the *001* peak). The octadecylammonium compound (**13**) gave the largest *d* spacing, where the *001* peak shifted beyond the measuring range.

2.2.2 XRD results for "intercalated" materials (after sonication with guests)

As mentioned earlier if the sonication facilitates intercalation of guest molecules, the layer distance should change in the perovskite lattice. This can be observed from the *001* peak in powder spectrum. First, sample **1** was sonicated with solvent only (aromatic, non layer dissolving solvent) and with a presence of fluoro-aromatic guests. The powder

X-ray diffraction patterns of the sonicated samples showed the same peak positions found
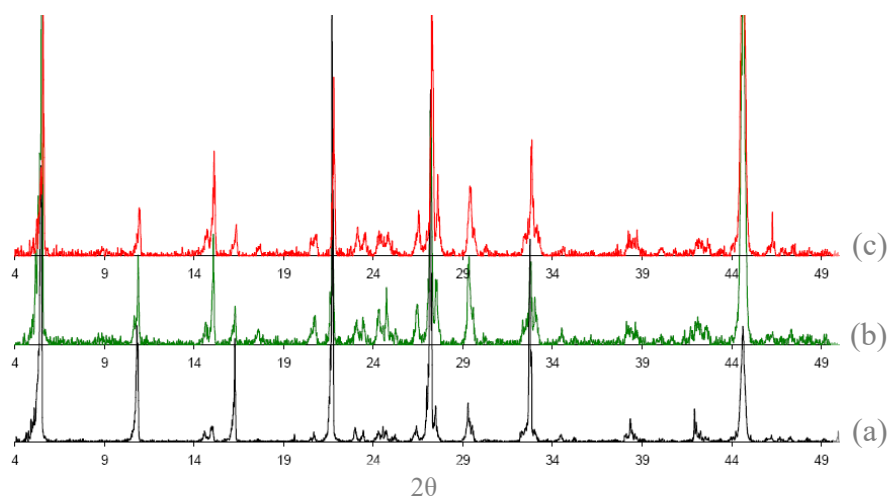in the starting materials, Fig. 2.6.

Figure 2.6   XRD patterns for **1**: (a) starting material, (b) sonicated with toluene,
(c) sonicated with 1,4-difluorobenzene in toluene.

The XRD patterns for sonicated samples **2-4** are shown in Figures 2.7 - 2.9.
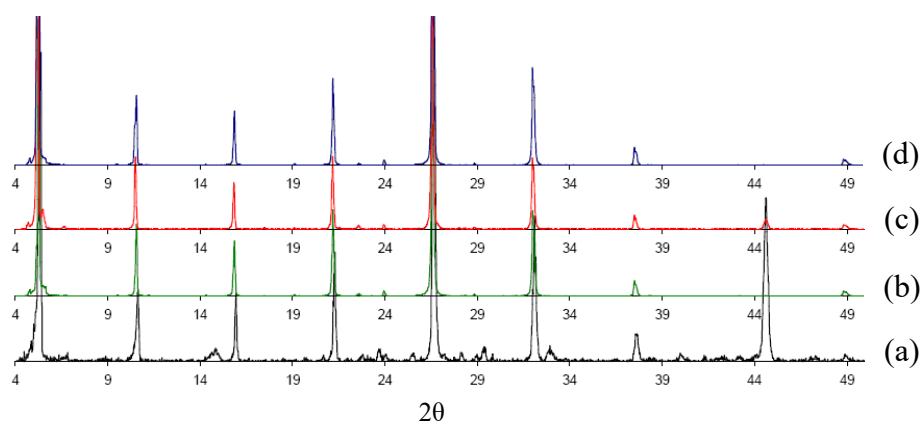

Figure 2.7   XRD patterns for **2**: (a) starting material (b) sonicated in toluene, (c)
sonicated with 1,4-difluorobenzene in toluene and (d) sonicated with
hexafluorobenzene in toluene.
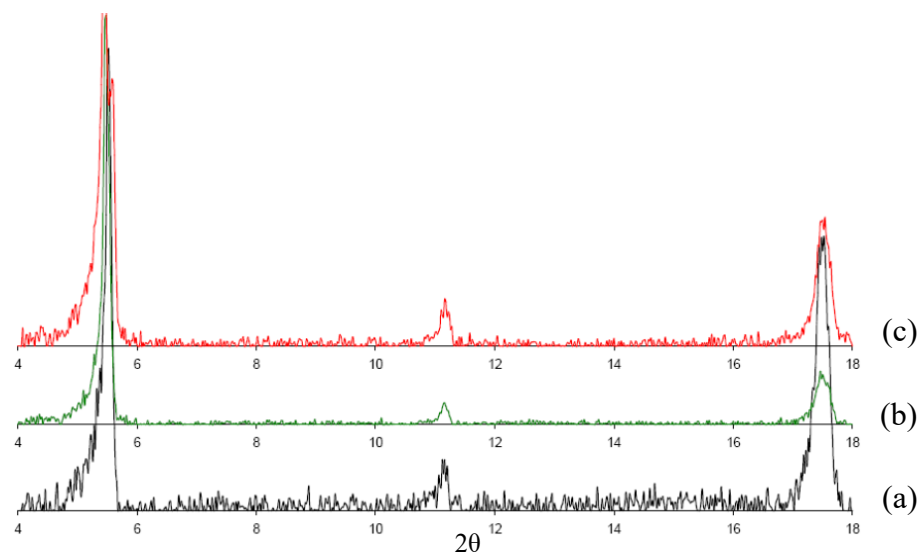
Figure 2.8   XRD patterns for **3:** (a) sonicated with toluene, (b) sonicated with 1,4-difluorobenzene in toluene and (c) sonicated with hexafluorobenzene in toluene.
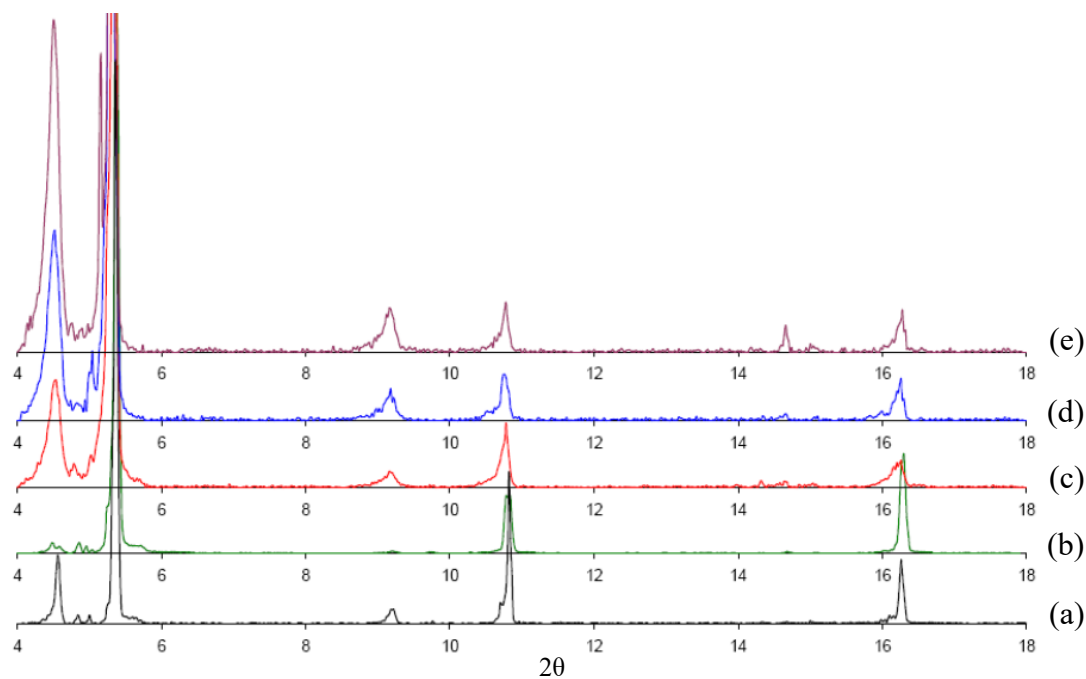

Figure 2.9   XRD patterns for **4:** (a) starting material (b) sonicated in toluene, (c) 1,4-difluorobenzene in toluene, (d) sonicated with hexafluorobenzene in toluene and (e) sonicated with benzotrifluoride in toluene.

In most cases the XRD pattern did not change when varying the sonication time. However, patterns of **2** showed a peak at 6° 2θ and a peak at 18° 2θ growing in as the sonication time increased. These peaks did not shift with a change in the guest molecule, as can be seen in Fig. 2.10. It is not clear what the source of the two peaks is.
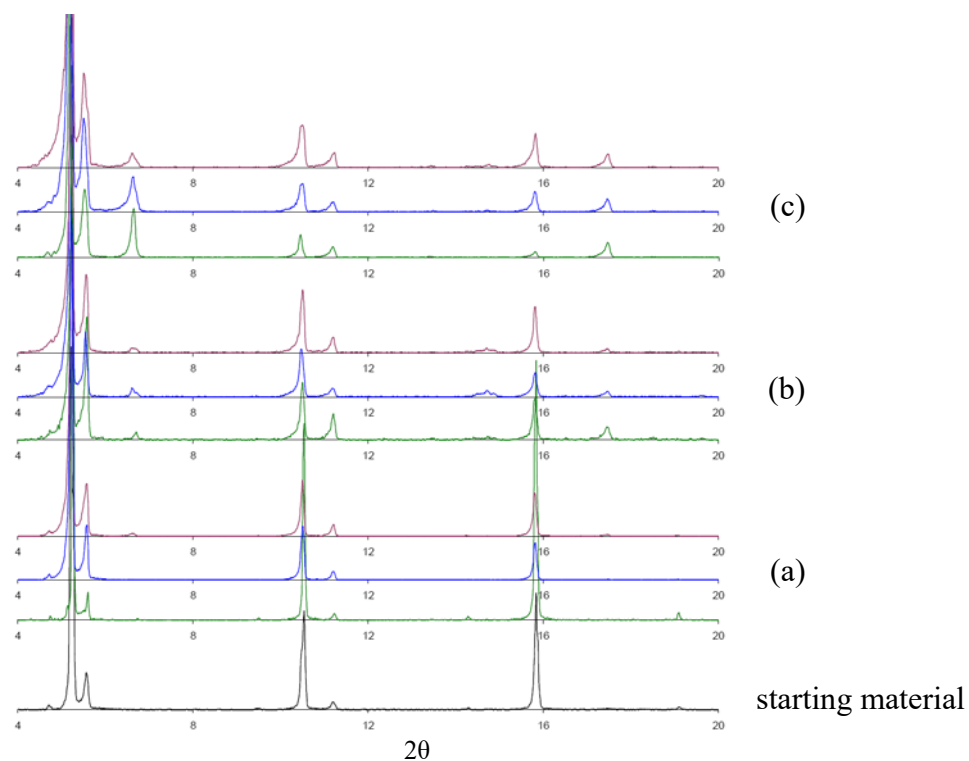

Figure 2.10   XRD patterns for **2**: sonication in toluene (green line) with (a) 30 min, (b) 3 h and (c) 8 h sonication time, sonication with 1,4-difluorobenzene in toluene (blue line) with (a) 30 min, (b) 3 h and (c) 8 h sonication time and sonication with hexafluorobenzene in toluene (maroon) with (a) 30 min, (b) 3 h and (c) 8 h sonication time.

The unbranched alkyl amine tin iodide perovskites (**7** and **8**) were sonicated with unbranched alkane solvents. The XRD patterns of the sonicated products are essentially identical to the patterns of the starting materials. (Figures 2.11 and 2.12)
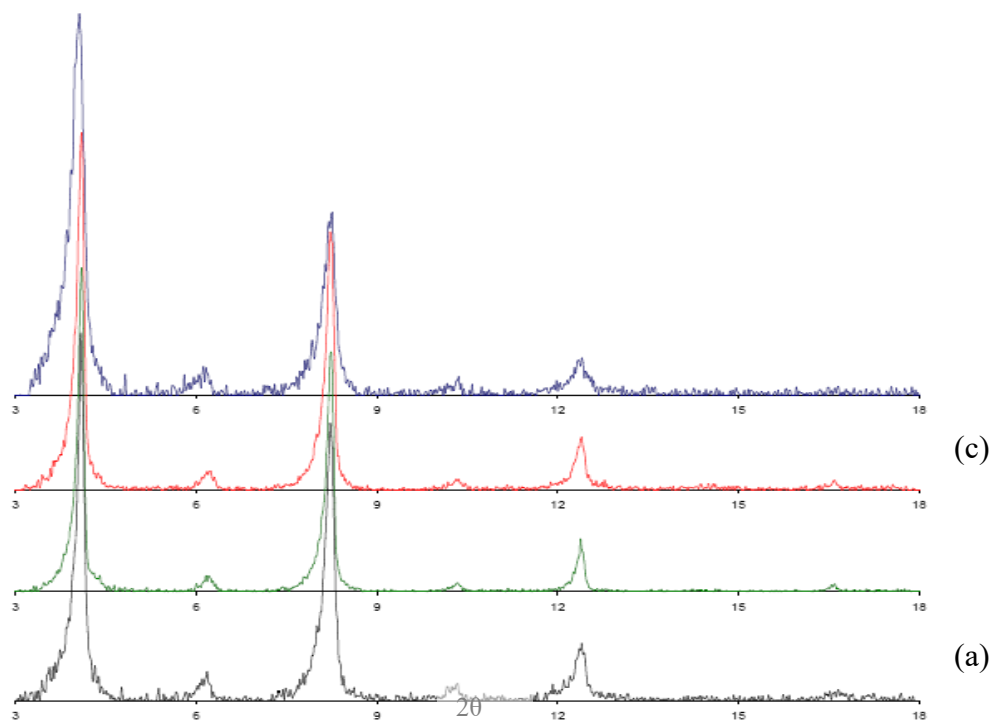

Figure 2.11   XRD patterns for **7**: (a) starting material, (b) sonicated with pentane, (c) sonicated with hexane and (d) sonicated with hexane in pentane.
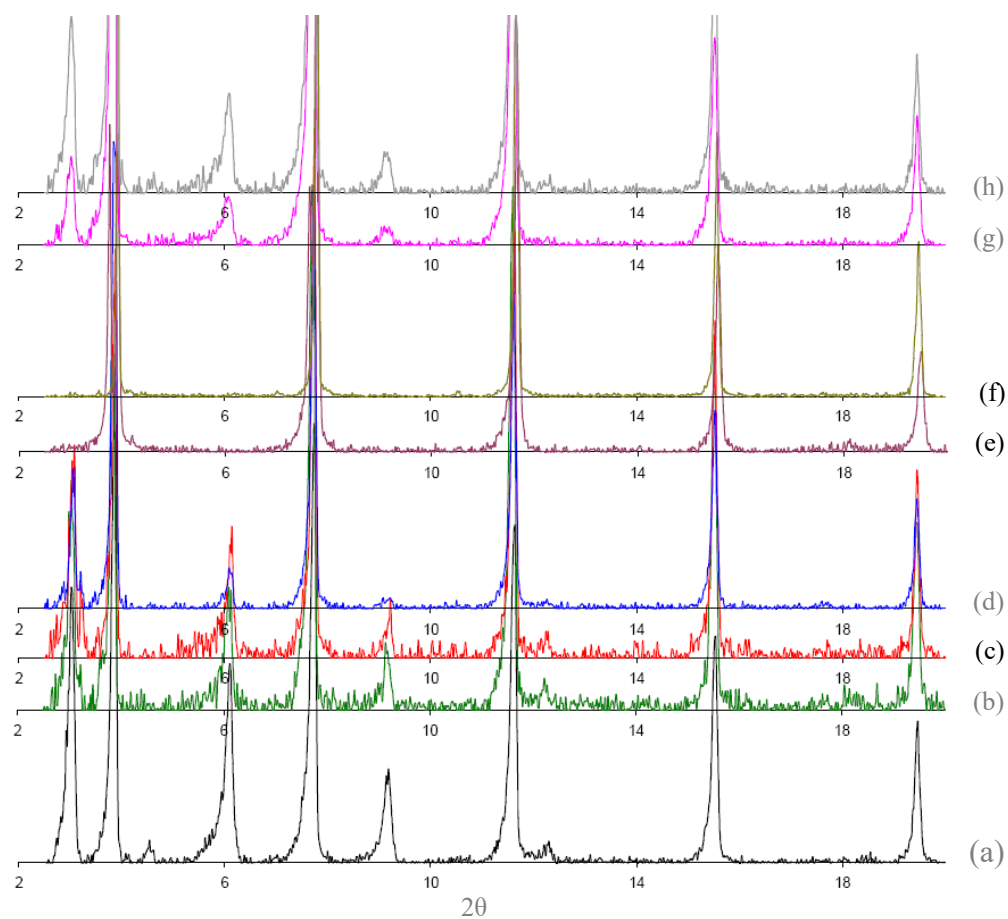
Figure 2.12   XRD patterns for **8**: (a) starting material, (b) sonicated with pentane, (c) sonicated with hexane in pentane, (d) sonicated with heptane in pentane, (e) sonicated with octyl cyanide in pentane,(f) sonicated with decanol in pentane, (g) sonicated in hexane and (h) sonicated with decane in hexane.

35

The sonications of Fig. 2.12 (b) to (h), where the alkanes are without functional groups resulted in solids that showed similar XRD patterns regardless of the solvent used. As can be seen in Fig. 2.12, the guest molecules with cyanide and alcohol functional groups [(e) and (f)] reacted with the host system during the sonication, which was indicated by the loss of crystallinity. This explains why the peaks at about 3°, 6° and 9° 2θ were not observed.

2.2.3 TGA data

The experimental TGA curves for the phenethylammonium tin iodide (**1** to **4**) intercalation experiments (Table 2.4) are shown in Figs. 2.13 to 2.16.
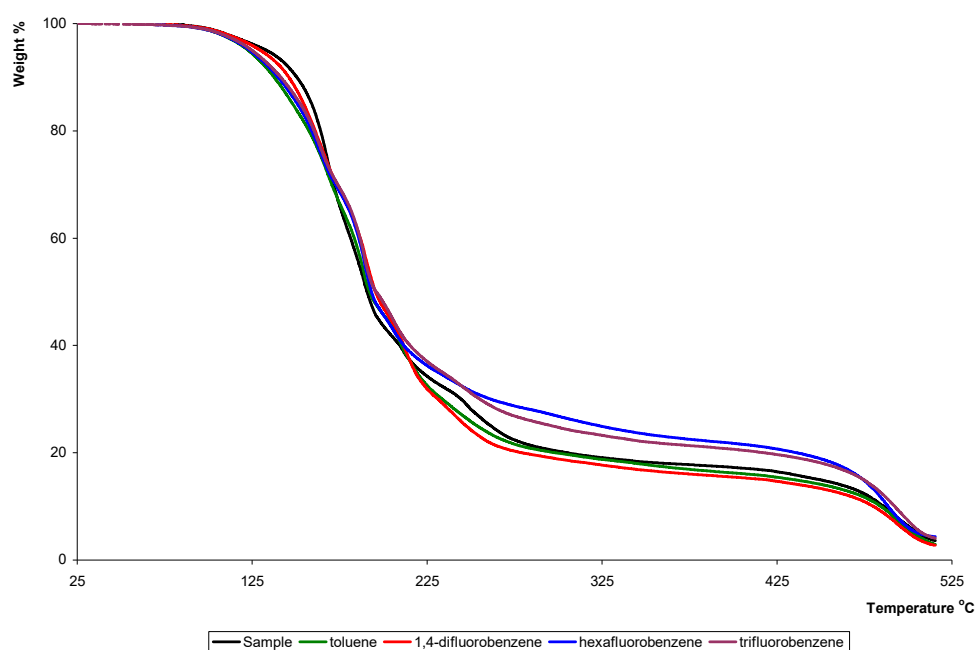

Figure 2.13   TGA of intercalation experiment for **1**.

The TGA of solids resulting from sonications of **2**, **3** and **4** were slightly different than the graphs found for sonicated solids in **1**. In **2-4**, the starting materials show increased weight losses in the 125-250 ^{o}C temperature range compared to the sonicated products, Figs. 2.14-2.16.
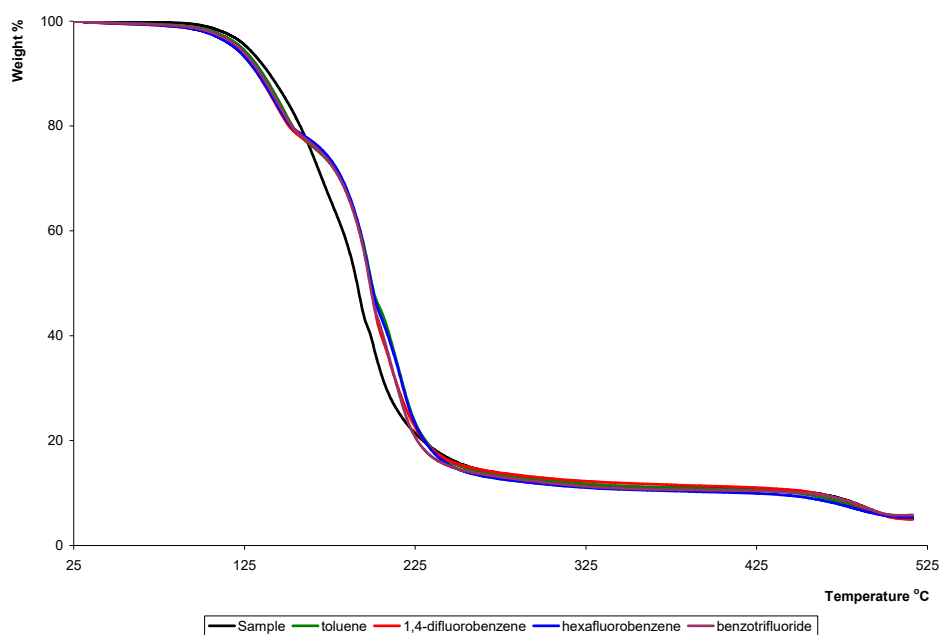

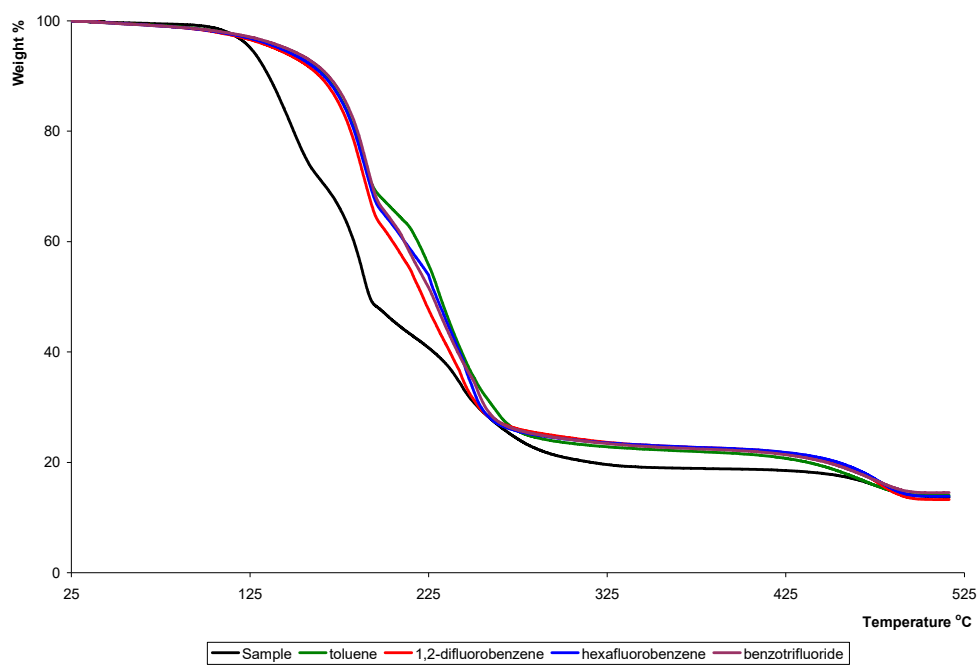Figure 2.14   TGA of intercalation experiment for **2**.

Figure 2.15   TGA of intercalation experiment for **3**.
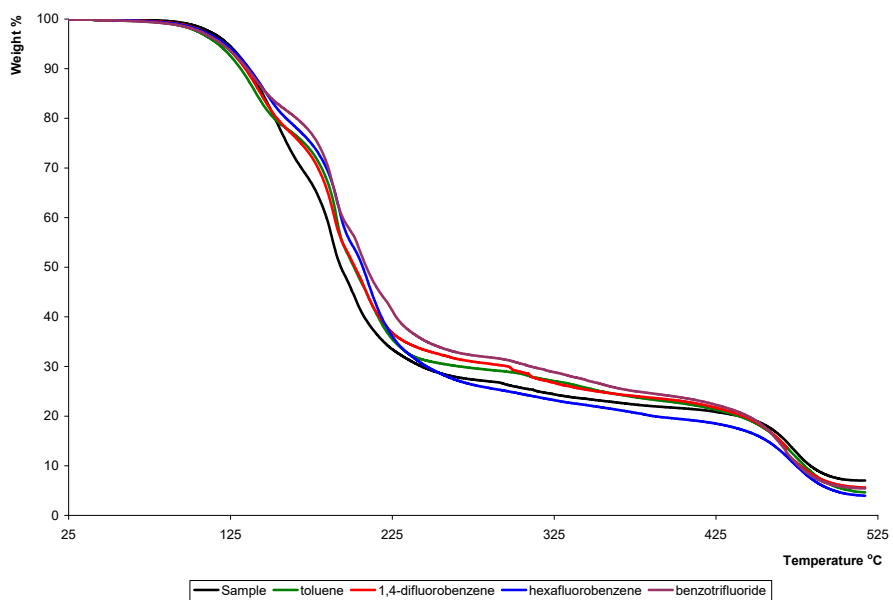
Figure 2.16   TGA of intercalation experiment for **4**.

Compound **8** shows an effect similar to compounds **2-4**, Fig. 2.17.
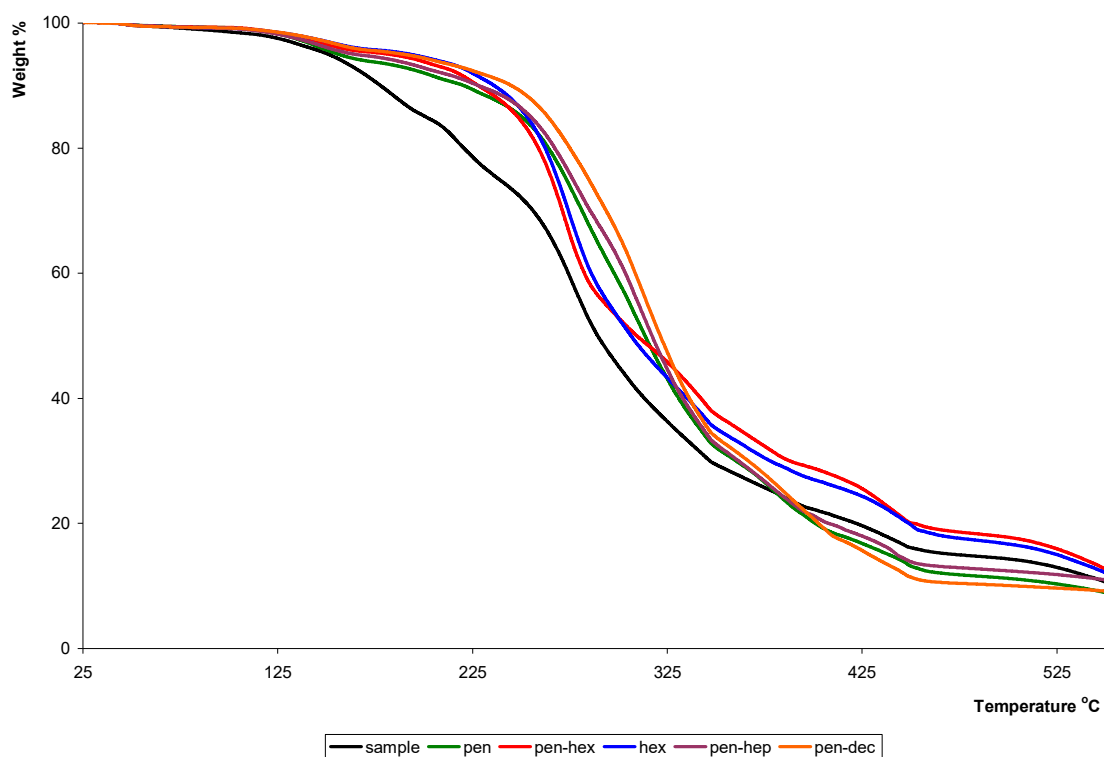
Figure 2.17   TGA of intercalation experiment for **8,** sonications with pentane, hexane in pentane, hexane, heptane in pentane and decane in pentane.

The conditions for sonication of compound **2** were varied – the amount of time for sonication in toluene, and sonication in toluene with hexafluorobenzene guest molecules was varied. The results are shown in Fig. 2.18.

Figure 2.18   TGA of **3** showing traces resulting from varying time of sonication in toluene alone and hexafluorobenzene with toluene.

The sonication experiments were repeated several times to ensure that the TGA data were reproducible.

2.2.4 TEM studies
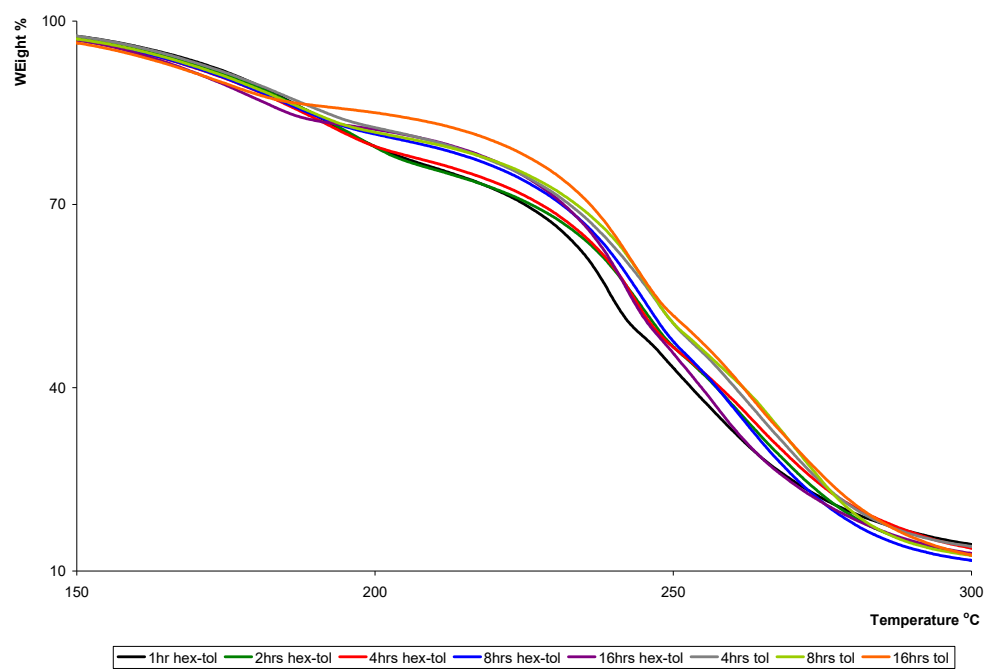
The TEM micrographs for samples of the starting material **2**, and the solids resulting from sonication of **2** with different solvents and/or guest molecules present are shown in Figure 2.19.

Significant morphological differences are apparent when comparing the starting materials with the sonicated products. It can be seen that the starting materials have a block shape, while the 1,4-difluorobenzene and hexafluorobenzene sonicated products have a smaller size and a feathered and rounded shape, respectively.
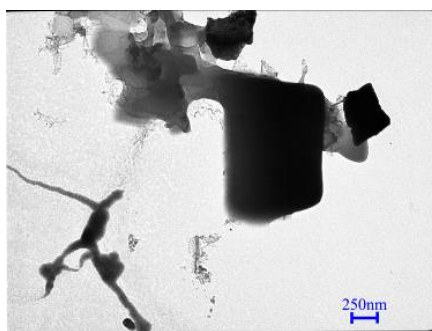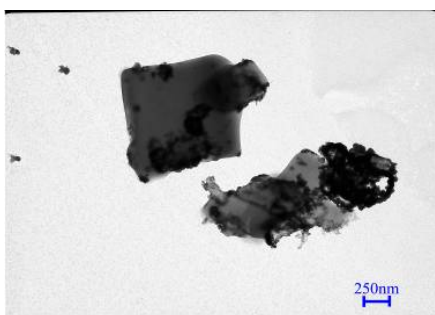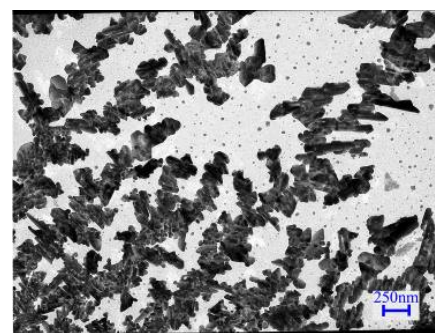
Figure 2.19   TEM bright field images of **2:** (a) starting material, (b) sonicated with toluene, (c) sonicated with 1,4-difluorobenzene in toluene, (d) sonicated with hexafluorobenzene in toluene at 20,000× mag. and (e) sonicated with benzene at 10,000× mag.

REFERENCES

(1)   Mitzi, D. B.; Dimitrakopoulos, C. D.; Kosbar, L. L. *Chem. Mater*. **2001**, *13*, 3728-3740.

CHAPTER III

DISCUSSION & CONCLUSION

3.1 Discussion

Following the work of D. B. Mitzi,[1] we have successfully reproduced the

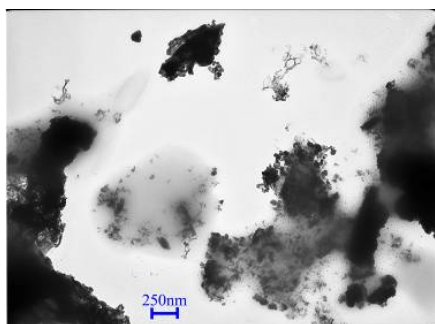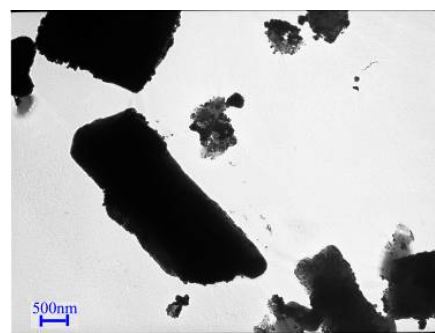synthesis of layered perovskites involving anionic tin iodide layers and organic

ammonium counterions. This includes synthesis of mono-ammonium perovskites of (4-

FPEA)$_2$SnI$_4$ (**1**), (3-FPEA)$_2$SnI$_4$ (**2**) and (2-FPEA)$_2$SnI$_4$ (**3**). We have also produced

(PEA)$_2$SnI$_4$ (**4**), (4-ClPEA)$_2$SnI$_4$ (**5**), (2-ClPEA)$_2$SnI$_4$ (**6**), (C$_{12}$H$_{28}$N)$_2$SnI$_4$ (**7**) and

(C$_{18}$H$_{40}$N)$_2$SnI$_4$ (**8**) complexes using in high yield. Cadmium chloride perovskite layers

with alkylammonium counterions were also synthesized and, as far as we know, this is

the first time the cadmium halide perovskite solids have been obtained using slow

cooling technique. Layered perovskites products of (C$_6$H$_{16}$N)$_2$CdCl$_4$ (**9**),

(C$_{10}$H$_{24}$N)$_2$CdCl$_4$ (**10**), (C$_{12}$H$_{28}$N)$_2$CdCl$_4$ (**11**), (C$_{14}$H$_{32}$N)$_2$CdCl$_4$ (**12**) and

(C$_{18}$H$_{40}$N)$_2$CdCl$_4$ (**13**) were obtained and identified using powder X-ray data.

The main point of the research was to determine if the layered materials **1-13**

would be able to intercalate and store small molecules. The challenge here is that the

perovskite system has a close packed structure, so there are no pre-existing spaces for the

intercalation of guest molecules. Therefore, significant intermolecular interactions

already exist in the crystalline structure and must be broken in order for intercalation of

the small molecules to occur. Strong lattice forces also exist in the structure, which might also prevent intercalation of small molecules. At the same time, the host structure (comprising coordinate-covalent and hydrogen bonds) must be retained. Therefore, detailed attention has been put in to selecting the guest molecules.

The guests should not dissolve the layered host, and should have attractive interactions with the hydrophobic interlayer. For the phenethylammonium perovskite solids (**1-4**), aromatic halide-substituted guest molecules were selected. Because halides are electron withdrawing, these guest electron-poor aromatic rings must be involved in attractive π-π interactions with the electron-rich aromatic rings found in the interlayer of starting materials. These attractive interactions could provide the driving force for intercalation of electron-poor aromatic guests. Further, the addition weight provided by the halide functionality could increase the dispersive forces between layers, providing another intermolecular driving force for guest intercalation.

3.1.1 Data analysis

3.1.1.1 TGA

Thermogravimetric analysis (TGA) is a technique used to determine the thermal stability and the volatility of a material by monitoring weight loss with increasing temperature. TGA can also be used to monitor an intercalation process as the weight loss percentages can be matched with removal of the guest molecules from the host structure at temperatures lower than the melting point of the host.[2] TGA results usually appear as a

continuous chart with the change of weight of the sample recorded with increasing temperature.[3]
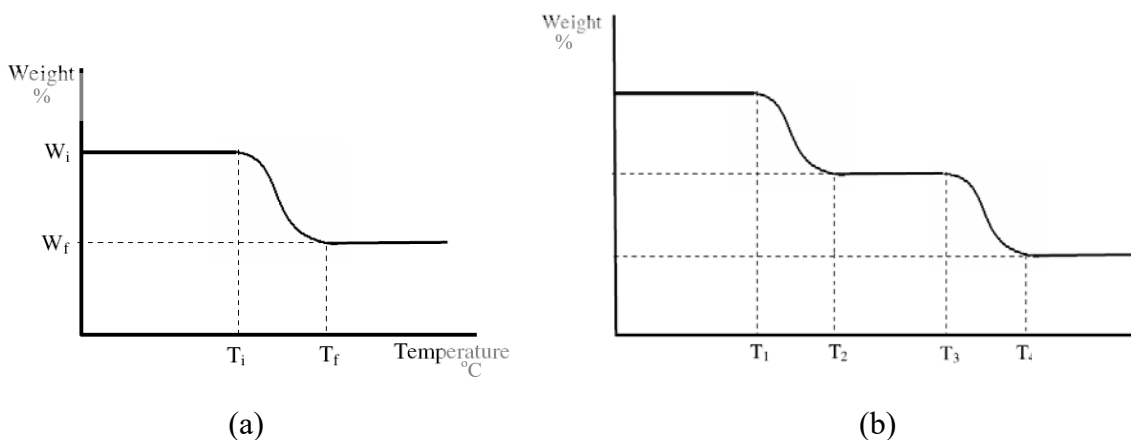

Figure 3.1   Schematic thermogram; (a) host only,[3] (b) host-guest complex

The TGA sample, usually in milligrams, is heated in a constant rate and the weight changes have been recorded. The diagram 3.1(a) shows a theoretical curve of a single step decomposition of the host material. Starting from W_i, the initial weight, the host material will lose weight upon heating and the residue remaining is W_f. The difference of weight ΔW corresponds to the temperature range of T_i to T_f, where T_i is the melting point of the host.[3] The diagram 1(b) shows a theoretical curve of host/guest complex where two step decomposition was observed with the lost of guest in the step one and the decomposition of the host in step two. T_1 corresponds to the melting point of the guest and T_2 corresponds to the melting point of the host.

A guest-intercalated complex should show an increased weight loss at lower temperatures as compared to the host starting material, because guest molecules are

46

volatile and will leave the host lattice before the host decomposes. This is due to the weak interactions between guest molecules and the host, as compared to the strong interactions of the host.

3.1.1.2 XRD

Powder X-ray diffraction is used in the identification and characterization of crystalline solids with distinctive diffraction patterns.[3] Pure crystalline materials will give sharp peaks, and when the sample becomes more amorphous peak broadening will occur. For layered materials, the *d* spacing of the layer can be determined using XRD data. For example, the interlayer distance can be determined using the peak corresponding to (*001*).
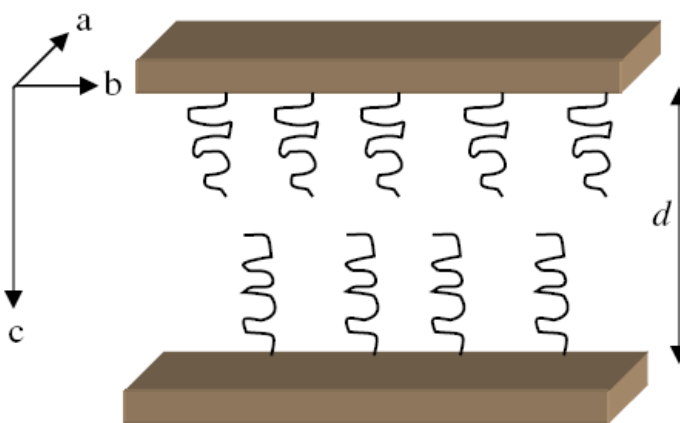

Figure 3.2   *d* spacing of a layered structure

When the guest molecules enter the host structure it leads to layer expansion of the c axis by separating the *ab* plane. This can be observed in the powder XRD patterns by the shifting of the (*001*) peak to a smaller 2θ value.
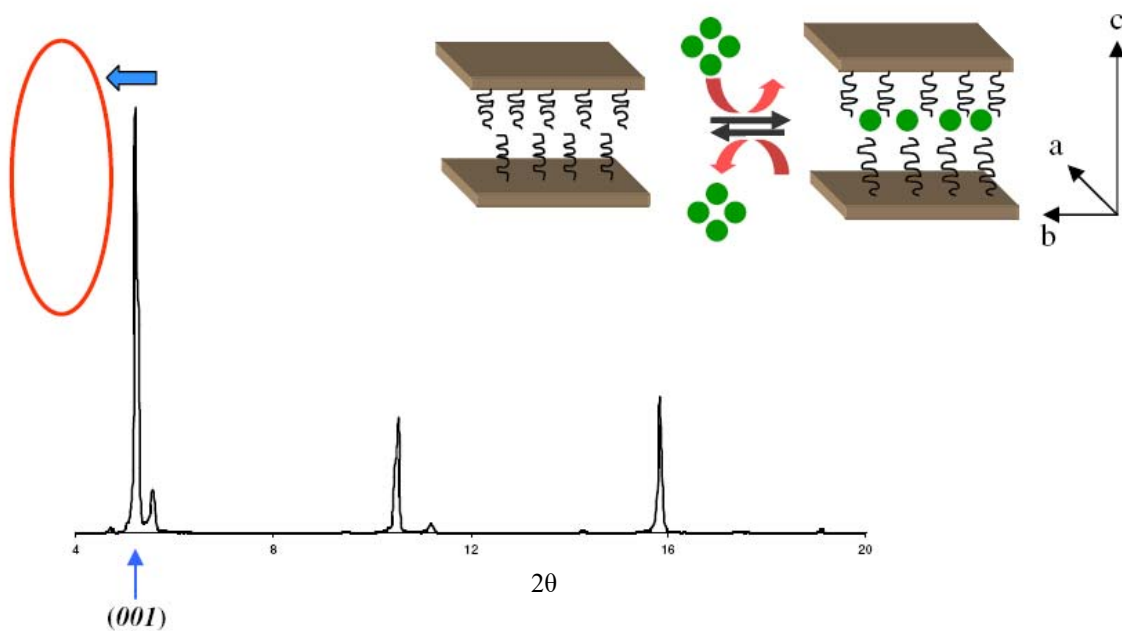

Figure 3.3   Shift of peaks with the layer expansion due to guest intercalation

3.1.2 Host-guest complexes

While Mitzi[2] incorporated the guest molecules *in solution* through co-crystallization of the solid, we wish to determine if guest molecules can be intercalated into the existing host solid lattice *via solid-solid transformation*. If guest incorporation occurred, the theoretical TGA graphs can be produced by calculating the weight loss starting from 1:1 theoretical host:guest complex with guest chosen as benzene, toluene, 1,4-difluorobenzene and hexafluorobenzene. It is assumed that the most weakly bound component (guest molecules) would be lost before the host solid decomposes.

Table 3.1

Theoretical calculations for TGA results for 1 equivalent of guest in **1-3**

Product	Molecular weight	% weight upon guest lost	% weight after loss of guest and amines	% weight after loss of guest, amines and iodides
1-3	906.47	100	69.09	13.09
1-3 w/ benzene	984.53	92.07	63.61	12.06
1-3 w/ toluene	998.54	90.78	63.02	11.89
1-3 w/ difluorobenzene	1020.5	88.82	61.37	11.63
1-3 w/ hexafluorobenzene	1092.5	82.97	57.32	10.86

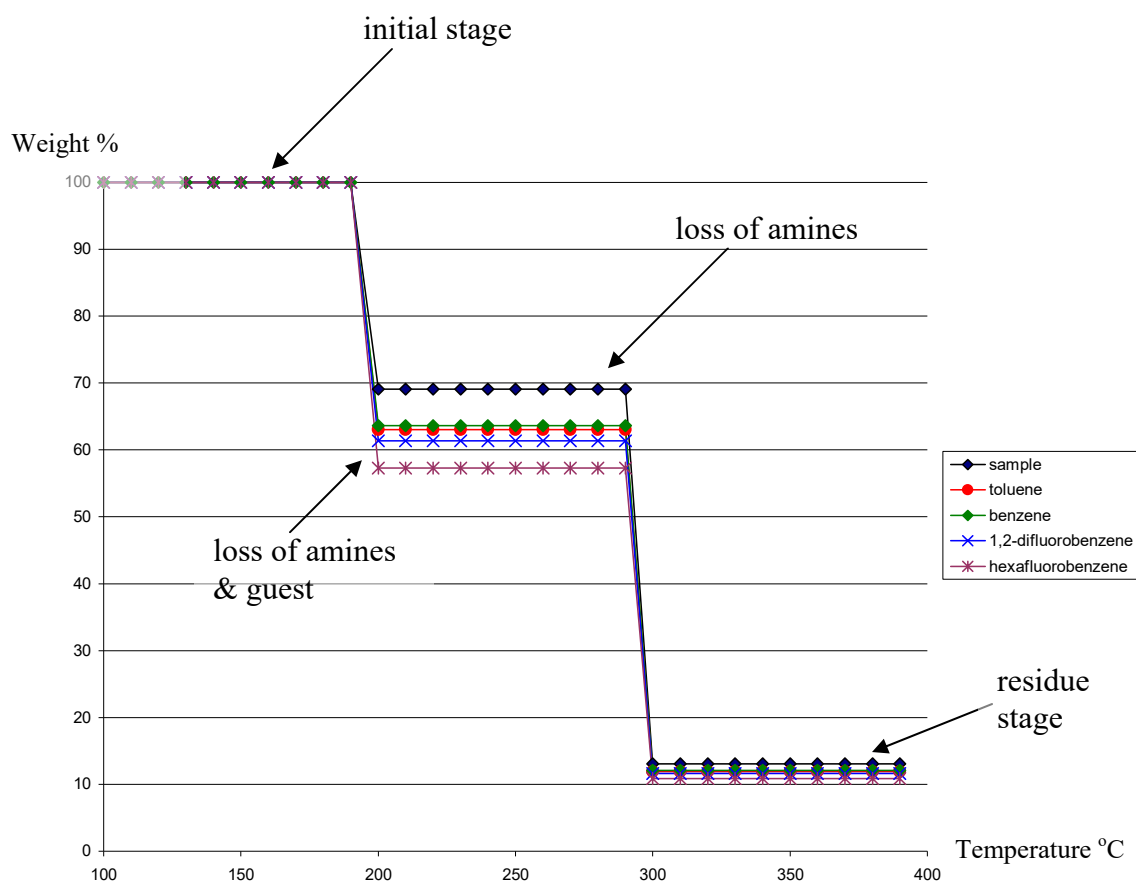A theoretical TGA curve is depicted in Figure 3.4.

Figure 3.4   Theoretical TGA curve for predicted host-guest fluoroammonium perovskite system with benzene, toluene, difluorobenzene and hexafluorobenzene as guests.

According to the theoretical calculations, heavier guests results in a larger weight loss upon heating. The hexafluorobenzene curve, with the heaviest guest, has the steepest drop upon guest loss. However, the experimental graphs shown in section 2.2.3 (Fig. 2.14 - 2.16) have indicated the complete opposite. In these graphs the control seems to have the steepest drop with lowest weight percentage, indicating the control curve having the heavier molecular weight at the start than the sonicated products.

The unusual weight loss behavior in TGA and the deterioration patterns shown in TEM was indicating that the sonicated samples were subjected to layer destruction during the mechanical stirring. The powder X-ray data of the starting materials and the sonicated products are the same (Section 2.2.2, Fig. 2.6 - 2.12). According to TEM, the particles become smaller during the sonication process, and this can be attributed to exfoliation of the layers. The mechanism for this surface layer destruction is shown in Fig. 3.5. During sonication, the guest molecules may penetrate the interlayer, and instead of the guest being retained in the layered compounds, the guest moves in and the layer peels away from the larger solid particle. This mechanism explains the fact that the TEM of sonicated particles are not only smaller but also become thin layer-like particles, Fig. 2.19.
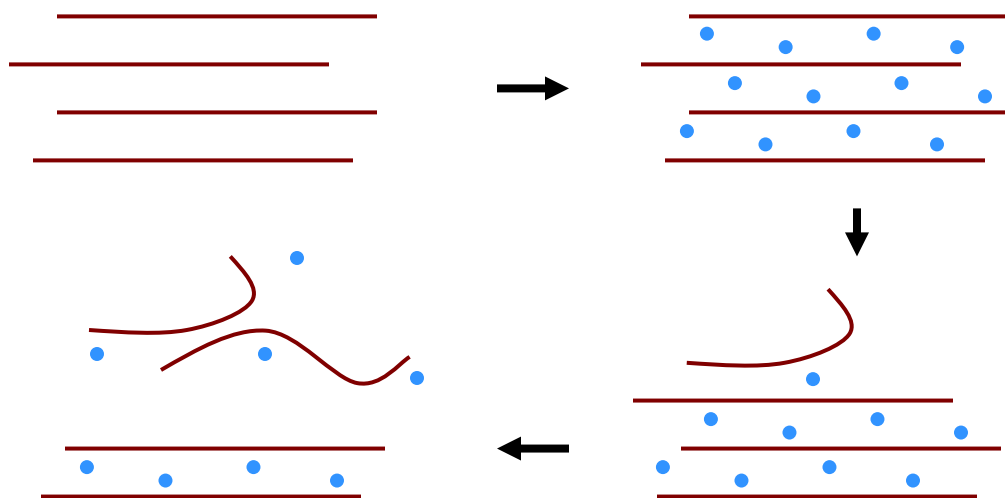
Figure 3.5   The process of exfoliation with sonication

The TEM picture taken after **2** sonicated with 1,4-difluorobenzene shows a distinctive feather type crystal morphology. Compound **2** sonicated in hexafluorobenzene showed gatherings of small particles instead of thick block particles as shown in the TEM of starting materials.

However, again the XRD spectrums did not show any difference between starting material and sonicated samples, which means the interlayer distance did not increase due to sonications, and therefore no intercalation occurred in these samples. The product **8** has the biggest interlayer distance of the given products (Fig. 2.12) and the layer distance should be more than adequate for the guest molecules to go in. However, we were not able to confirm the existence of the guest molecules in sonicated samples using XRD. The TGA also did not indicate a presence of guest molecules in sonicated samples. It was uncertain whether the guests were not retained in the lattice or the layer distance

will not further improve with guest intercalation as already the layer distance is more than 25 Å. The hexafluorobenzene was the heaviest guest molecule used in sonications but no signs of interlayer changes observed in XRD.

The XRD of product **2** for varying sonication times (Figure 2.10), resulted in changes in the intensities of the peaks at 6.6^o and 17.4^o 2θ. The peaks were also broad. It could be assumed from the band broadening that the sample loses crystallinity or becomes much smaller during the sonication process. Varying the amount of time used for sonication helped us to limit the sonication time for the maximum of 3 hours.

3.2 Conclusion

In this research we have investigated the intercalating ability of close packed inorganic-organic hybrid perovskites, to determine whether these materials would be useful as hosts for the transport and storage of organic guest molecules. According to the powder XRD data, guest intercalation has not occurred, because the same patterns are observed for both starting materials and sonicated materials TEM results showed deterioration of starting materials upon sonication, which may be explained by exfoliation of particles. TGA data shows some hard-to-explain differences between the starting materials and the sonicated products. Because there is no evidence for guest inclusion, the starting materials and sonicated products should show the same trace. However, in compounds **2**, **3**, and **4**, the TGA of starting materials show increased weight loss at low temperature, compared to sonicated materials. This is the opposite of what we would expect for guest inclusion upon sonication. The intercalation into a layered structure may sometimes lead to expansion of the interlayer separation due to weak interlayer bonding and extensive layer separations may lead to complete exfoliations.

For the future studies, the use of aromatic guests such as nitrobenzenes, to intercalate guests with very electron-poor π systems, might help secure the guest into a host containing electron-rich aryl groups. Adding substituents like NMe_2 to the aromatic ammonium counterions would make electron-rich host system. The combination of a very electron-poor guest and a very electron-rich host might help promote guest intercalation and retention through strong intermolecular interactions.

The intercalation of molecules or ions into layered solids is useful for applications such as improving lithium ion batteries. The classical graphite carbon grid in the lithium ion battery can be altered or replaced to improve the capacity and the lifetime of the batteries. Finding a suitable layered structure that can promote storage and intercalation of small molecules and ions will be important for applications such as these.

REFERENCES

(1)   Mitzi, D. B.; Dimitrakopoulos, C. D.; Kosbar, L. L. *Chem. Mater.* **2001**, *13*, 3728-3740.

(2)   Mitzi, D. B.; Medeiros, D. R.; Malenfant, P. R. L. *Inorg. Chem.* **2002**, *41*, 2134-2145.

(3)   West, A. R. *Solid State Chemistry and its Applications*; John Wiley & Sons, NY, **1984**.

CHAPTER IV

INTRODUCTION

4.1 Introduction

The technological advancements made during the last few decades have improved materials chemistry research dramatically. The synthesis of small particles is a new trend popularized with a variety of applications, especially with the origin of nanotechnology.[1] A new dimension of structural possibilities was created using these smaller particles with improved electronic, magnetic, optical, and catalytic properties.[1,2]

We became interested in tin oxides due to applications such as electrode materials.[3-6] One goal has been to improve the capacity of lithium ion batteries by using tin oxides.[7-10]

In material studies, use of template-free methods of synthesizing particles has been shown to have fewer complications in the synthesis.[1,11] Zeng and coworkers reported a one-pot hydrothermal synthesis of TiO_2 nanospheres *via* the Ostwald mechanism with urea and thiourea additives.[12] The hollow spherical particles develop after prolonged heating with inside-out ripening. Archer and coworkers applied this mechanism to obtain SnO_2 spherical nanoparticles, where they have also observed core/shell-type hollow nanospheres.[3]

With the prior experience of successfully creating metal halide clusters by steric tuning of *ortho* substituted counterions,[13] we are interested in applying it to a template free hydrothermal synthesis of particles of SnO_2.[3] The following chapter (Chapter 5) will describe our new experimental attempts to control shape and size of SnO_2 particles in a hydrothermal synthesis.

4.2 Tin oxide chemistry

The first reported growth of single crystals of tin oxides was in 1961.[14] Since then, SnO_2 particles have been studied for a variety of applications such as gas sensors,[15,16] catalysis,[17,18] transistors,[19] solar cells,[20] electrode materials[4,6] etc.

One of the goals of the research described here is to create 1-D, 2-D, and 3-D particles using substituted anilines. Reasons for synthesizing 1-D particles include the fact that they have a high surface-to-volume ratio and excellent surface activities, so they can be used in fabricating sensors. For example, Yang and coworkers reported a photochemical NO_2 sensor device based on the use of tin oxide nanoribbons.[16] The biggest problem with earlier commercial sensors was desorption of the gas molecules from the metal surface. The single crystal SnO_2 nanoribbons used in their study showed favorable adsorption and desorption of NO_2 at room temperature with the use of ultra-violet light. These nanoribbons were synthesized using a thermal deposition process.[16,21]

Wang et al. reported 1-D tin oxide nanowires made from $SnC_2O_4.2H_2O$ by mixing with poly(vinylpyrrolidone) in ethylene glycol.[15] Smooth-surfaced starting materials were transformed into highly porous structures consisting of interconnected nanocrystallites.

Unlike the earlier nanostructures, which needed elevated temperatures or UV light, these nanowires showed high sensitivity and reversibility even under ambient conditions.[15] Fahlman and coworkers reported a synthesis of tin oxide nanoparticles using CO_2 as a co-reactant and stabilized by a series of dendritic polymers.[22] Because the particle diameters measured only 3-5 nm, these are some of smallest reported tin oxide nanoparticles. Cheng et al. reported the growth of SnO_2 nanorods using a one-pot solution-based technique at low temperature, where $SnCl_4.5H_2O$ was dissolved in an ethanol-water mixture.[23]

Xin and coworkers reported a size controllable tin oxide nanoparticle preparation by using $SnCl_2$ with ethylene glycol at atmospheric pressure.[17] These tin oxide particles were used in enhancing the catalytic activity for alcohol electro-oxidation in fuel cells. The carbon-supported $PtSnO_2$ catalyst is better at promoting catalytic activity than the conventional Pt/C catalytic system.[17] Harrison et al. reported that a manganese-tin oxide catalyst system can be obtained by either co-precipitation or impregnation.[18] The purpose was for the automobile industry to catalyze the oxidation of carbon monoxide.

Vijayamohanan and coworkers reported a shape-selective synthesis of submicron-sized tin oxide wires, bipyramids and cubes using RuO_2 as a catalyst.[24] The different shapes were achieved through vapor-solid or vapor-liquid-solid progressions. Gregg and coworkers investigated a tin oxide sensitizing dye-semiconductor system with perylene derivatives,[20] which was used for water-splitting dye-sensitized solar cells.

Gedanken and coworkers studied the Li insertion potential of SnO_2 nanoparticles obtained using a sonochemical method.[6] These smaller particles were prepared by

ultrasonic irradiation of $SnCl_4$ in azodicarbonamide solution in air. The interest in tin-based materials for anode materials in lithium ion batteries developed due to their high theoretical capacity compared to graphite materials. Tin alone gives 990 mAh/g and tin oxide also provides 790 mAh/g compared to 372 mAh/g for graphite.[8] However, the biggest challenge with the tin-based electrodes was the poor cyclability resulting from large volume changes during the lithium intercalating/deintercalation process.[10,25] In early studies, by combining tin materials into a carbon matrix the cyclability was improved.[7] In 2003, Lee et al. reported that structural stability can be achieved by using hollow particles.[25] By following the above work, Archer and coworkers developed a one pot template-free synthesis of tin oxide hollow particles. These particles can be used as potential electrode materials for lithium ion rechargeable batteries due to their high storage capacity.[3]

4.3 Template-free synthesis of smaller particles

Smaller particle growth can be achieved by kinetic confinement, where the reaction is spatially confined and growth will terminate when the materials are consumed or the available space is filled.[1] This is normally achieved using template-based synthesese of e.g. nanotubes formed by filling alumina membranes,[26] or nanowires formed by mesoporous silica materials.[27]

However, a number of wet chemical methods have been developed in recent times, and these facilitate growth of small particles without physical restrictions. Guo et al. reported the growth of TiO_2 microspheres using an EtOH/H_2O solvent system.[28] In the

60

Archer synthesis,[3] tin oxides nanospheres were obtained in the presence of urea, thiourea or ethyldiamine additives. Vayssieres et al. synthesized tin oxide nanorods also using urea additives with different reaction conditions (lower reaction temperature and longer reaction time).[29] Zhang and coworkers synthesized $In(OH)_3$ and In_2O_3 nanocubes and spheres using an amine-assisted hydrolysis.[30] Several mechanisms were identified to facilitate growth of hollow particles in these template free synthetic routes, such as the Kinkendall effect,[31] corrosion based inside-out evacuation[32] and the inside-out Ostwald ripening mechanism.[3,12]

4.4 Steric tuning by *ortho* substituted counterions

In our lab, we have successfully demonstrated that network topology can be controlled using steric tuning of *ortho* substituted counterions.[13] In this case, a cadmium chloride perovskite sheet was transformed into an expanded layer and then into a 0-D cluster by changing the hydrophilic substituents in the counterion from H to CH_3 and then to CH_3CH_2.[13] It was interesting to note that the length of amine did not affect the architecture, only the size of *ortho* substituents affected cluster shape, and the larger *ortho* substituent led to cluster formation. The hypothesis for the work described in Part II is that including *ortho*-substituted anilines in the reaction mixture will change the size and/or shape of the particles, depending on the size and/or shape of the *ortho* substituent.

61

REFERENCES

(1)   Cao, G.; Editor *Nanostructures and Nanomaterials: Synthesis, Properties, and Applications*; Imperial College Press: London, **2004**.

(2)   Steed, J. W.; Turner, D. R.; Wallace, K. J. *Core Concepts in Supramolecular Chemistry and Nanochemistry*; John Wiley & Sons, Ltd.: Chichester, UK, **2007**.

(3)   Lou, X. W.; Wang, Y.; Yuan, C.; Lee, J. Y.; Archer, L. A. *Adv. Mater.* **2006**, *18*, 2325-2329.

(4)   Wang, Y.; Zeng, H. C.; Lee, J. Y. *Adv. Mater.* **2006**, *18*, 645-649.

(5)   Han, S.; Jang, B.; Kim, T.; Oh, S. M.; Hyeon, T. *Adv. Funct. Mater.* **2005**, *15*, 1845-1850.

(6)   Zhu, J.; Lu, Z.; Aruna, S. T.; Aurbach, D.; Gedanken, A. *Chem. Mater.* **2000**, *12*, 2557-2566.

(7)   Idota, Y.; Kubota, T.; Matsufuji, A.; Maekawa, Y.; Miyasaka, T. *Science* **1997**, *276*, 1395-1397.

(8)   Cui, G.; Hu, Y.-S.; Zhi, L.; Wu, D.; Lieberwirth, I.; Maier, J.; Muellen, K. *Small* **2007**, *3*, 2066-2069.

(9)   Liu, W.; Huang, X.; Wang, Z.; Li, H.; Chen, L. *J. Electrochem. Soc.* **1998**, *145*, 59-62.

(10)   Courtney, I. A.; Dahn, J. R. *J. Electrochem. Soc.* **1997**, *144*, 2943-2948.

(11)   Kinge, S.; Crego-Calama, M.; Reinhoudt, D. N. *ChemPhysChem* **2008**, *9*, 20-42.

(12)   Yang, H. G.; Zeng, H. C. *J. Phys. Chem. B* **2004**, *108*, 3492-3495.

(13)   Chen, C.-L.; Beatty, A. M. *Chem. Commun.* **2007**, 76-78.

(14)   Marley, J. A.; MacAvoy, T. C. *J. Appl. Phys.* **1961**, *32*, 2504-2505.

(15)   Wang, Y.; Jiang, X.; Xia, Y. *J. Am. Chem. Soc.* **2003**, *125*, 16176-16177.

(16)   Law, M.; Kind, H.; Messer, B.; Kim, F.; Yang, P. *Angew. Chem. Int. Ed.* **2002**, *41*, 2405-2408.

(17)   Jiang, L.; Sun, G.; Zhou, Z.; Sun, S.; Wang, Q.; Yan, S.; Li, H.; Tian, J.; Guo, J.; Zhou, B.; Xin, Q. *J. Phys. Chem. B* **2005**, *109*, 8774-8778.

(18)   Harrison, P. G.; Bailey, C.; Bowering, N. *Chem. Mater.* **2003**, *15*, 979-987.

(19)   Aoki, A.; Sasakura, H. *Jpn. J. Appl. Phys.* **1970**, *9*, 582.

(20)   Ferrere, S.; Zaban, A.; Gregg, B. A. *J. Phys. Chem. B* **1997**, *101*, 4490-4493.

(21)   Huang, M. H.; Mao, S.; Feick, H.; Yan, H.; Wu, Y.; Kind, H.; Weber, E.; Russo, R.; Yang, P. *Science* **2001**, *292*, 1897-1899.

(22)   Juttukonda, V.; Paddock, R. L.; Raymond, J. E.; Denomme, D.; Richardson, A. E.; Slusher, L. E.; Fahlman, B. D. *J. Am. Chem. Soc.* **2006**, *128*, 420-421.

(23)   Cheng, B.; Russell, J. M.; Shi, W.; Zhang, L.; Samulski, E. T. *J. Am. Chem. Soc.* **2004**, *126*, 5972-5973.

(24)   Ramgir, N. S.; Mulla, I. S.; Vijayamohanan, K. P. *J. Phys. Chem. B* **2005**, *109*, 12297-12303.

(25)   Lee, K. T.; Jung, Y. S.; Oh, S. M. *J. Am. Chem. Soc.* **2003**, *125*, 5652-5653.

(26)   Lakshmi, B. B.; Dorhout, P. K.; Martin, C. R. *Chem. Mater.* **1997**, *9*, 857-862.

(27)   Lee, K.-B.; Lee, S.-M.; Cheon, J. *Adv. Mater.* **2001**, *13*, 517-520.

(28)   Guo, C.-W.; Cao, Y.; Xie, S.-H.; Dai, W.-L.; Fan, K.-N. *Chem. Commun.* **2003**, 700-701.

(29)   Vayssieres, L.; Graetzel, M. *Angew. Chem. Int. Ed.* **2004**, *43*, 3666-3670.

(30)   Chen, L.-Y.; Zhang, Y.-G.; Wang, W.-Z.; Zhang, Z.-D. *Eur. J. Inorg. Chem.* **2008**, 1445-1451.

(31)   Yin, Y.; Rioux, R. M.; Erdonmez, C. K.; Hughes, S.; Somorjai, G. A.;
        Alivisatos, A. P. *Science* **2004**, *304*, 711-714.

(32)   Xiong, Y.; Wiley, B.; Chen, J.; Li, Z.-Y.; Yin, Y.; Xia, Y. *Angew. Chem.
        Int. Ed.* **2005**, *44*, 7913-7917.

CHAPTER V

EXPERIMENTAL DETAILS

Hollow SnO$_2$ particles were synthesized by a method modified from the Archer preparation[1] (see Chapter 4), with *ortho*-substituted aniline molecules used in place of urea. Details on the synthesis and characterization techniques of the particles are provided below.

5.1 Materials and methods

Potassium stannate trihydrate and the anilines (except biphenylamine) were purchased from Sigma-Aldrich. 2-Biphenylamine (2-aminobiphenyl) was purchased from Pfaltz and Bauer. Reagent grade ethyl alcohol from Fisher Scientific and distilled water were used as solvents. The 23 mL Parr-bombs were obtained from the Parr Instrument Company and the carefully closed stainless steal containers were heated using a programmable oven with a 120-250 ^{o}C temperature range.

5.2 Sample preparation for the hydrothermal synthesis

The samples were prepared according to the template-free synthesis of SnO$_2$ by Archer and coworkers.[1] Instead of using urea, thiourea or ethyldiamine as the additives, various *ortho*-anilines were added to control the morphology of the product. A sample

reaction is as follows: About 0.500 g of potassium stannate trihydrate ($K_2SnO_3.3H_2O$, 1.7 mmol, 99.9%) was added to 10 mL of ethanol-water 50-50% mixture in a conical flask. The amine was added slowly and mixed. The solution became slightly white and translucent after about 5 minutes of gentle shaking. The solution was then transferred carefully to the 23 mL Teflon chamber of the Parr-bomb using a glass pipette. The Parr-bomb was tightly closed and placed in the programmable oven at the desired temperature.

After heating in the oven, the Parr-bombs were allowed to cool to room temperature (2-3 h). They were opened carefully and the product was extracted by suction filtration and washed using ethanol. The white, powder-like product was collected onto a filter paper and dried in an oven at 50 ^{o}C overnight, then kept in dry glass vials for characterization.

5.3 Experimental variables

Reactions had the following variables:

- Oven temperature
- Concentration of amines
- Amount of time heated
- Nature of the amine substituents

The tables below give specific information on all variables.

Table 5.1

Variables considered in the synthesis of tin oxide particles

Sample #	Amine type	Temperature	Concentration	Time
1	-	120 °C	0.1 mmol	3 h
2-6	anilines	150 °C	0.4 mmol	20 h
7-8	alkyl amines	250 °C	1 mmol	67 h
			4 mmol	
			20 mmol	

Table 5.2

List of amine substituents used in the synthesis

Amine substituents			
Sample #	Anilines	Sample #	Alkyl amines
2	aniline	7	hexylamine
3	2-chloroaniline	8	decylamine
4	2-bromoaniline		
5	2-*tert*-butylaniline		
6	2-biphenylamine		

5.4 Transmission electron microscopy

TEM is an imaging technique used to observe smaller particles. Information can be gathered about the size, shape and morphology by using bright field images (BFI). Information about diffraction patterns and lattice parameters in crystalline materials can be obtained from selected area diffraction (SAD).

The transmission electron microscope works like a projector in microscopic or nano scale. The imaging is done using excited beam of electrons traveling from the tungsten filament (cathode) to the anode through voltage of 20~100 kV.[2] The electrons go through an opening in the anode and through a series of lenses to strike the sample. The accelerated electrons may go through the thin specimen or a part of the specimen and the transmitted portion of the electrons are enlarged and then focused onto the objective lens.[3] Then the user will be able to observe the enlarged image from a phosphor image screen.[2] TEM offers high magnification ranging from 50 to 10^6. The limitation for TEM is the depth resolution. Although the electron scattering information is achieved with three dimensionally, it was projected only to a 2-D detector.[3]

In this study, all the TEM images were taken at the Electron Microscopy Center at Mississippi State University with a JOEL JEM-100CX microscope, Fig. 5.1.

Figure 5.1   JOEL JEM-100CX transmission electron microscope

5.5 Scanning electron microscopy (SEM)

SEM was previously used in biological studies and now it has become a popular application in material studies.[3] Information about size and morphology on sample surfaces can be obtained from SEM. The main differentiation from TEM is that the electrons do not penetrate through the sample. The electron beam moves back and forth over the sample producing magnified digital images of the surface.[4] When the electron beam bombards on the sample, number of interactions taken place where electrons and photons are emitted from the sample. These electrons provide information for digital imaging. The emitted electrons are collected at a cathode ray tube.[3] The advantages of the SEM are that it provides 3-D real space images of specimens and bulk amounts of sample materials can be applied in imaging.[3] The SEM can provide magnifications from ~10 to 300,000×. Three types of images can be produced in SEM: secondary electron images (SEI), backscattering electron images and elemental X-ray maps. In this study we have taken secondary electron images of the tin oxide particles.

The images were taken at the Electron Microscopy Center at Mississippi State University with a JOEL JSM-6500F field emission scanning electron microscope, Fig. 5.2.

Figure 5.2   JOEL JSM-6500F field emission scanning electron microscope

5.6 Powder X-ray spectra of SnO$_2$

A small amount of sample was finely ground and applied to the zero background plate with a few drops of ethanol (wet packing method). Once the sample was dry the XRD pattern was obtained from 10° to 80° 2θ. Step times ranged from 10 to 25 s. Each pattern confirmed that the samples analyzed were pure tin oxide. (Appendix C, Fig. C.1)

It is important to note that with or without the presence of amines the K$_2$SnO$_3$.3H$_2$O will produce SnO$_2$ in the hydrothermal synthesis (Appendix C, Fig. C.1, product **1).** However, the spherical growth of particles is facilitated only in the presence of urea (in Archer's studies[1]) or amines (Chapter 6).

5.7 Transmission electron microscopy

5.7.1 TEM sample grid preparation

A minute amount of sample was placed in a centrifuge tube and three drops of ethanol (100%) were added and mixed with a pipette to create a dilute slurry. A small drop from the mixture was added to a Formvar-coated 200 mesh copper sample grid (Fig. 5.3 (a)) and allowed to settle for about 10 seconds. The excess solvent was carefully wicked away using a small piece of filter paper. Two grids were prepared for each sample, and the best looking sample grid was used for the imaging in the microscope. The grids were allowed to air dry for few seconds and then placed in the sample holders (Fig. 5.3 (b)) for further analysis by transmission electron microscope.

(a) **(b)**
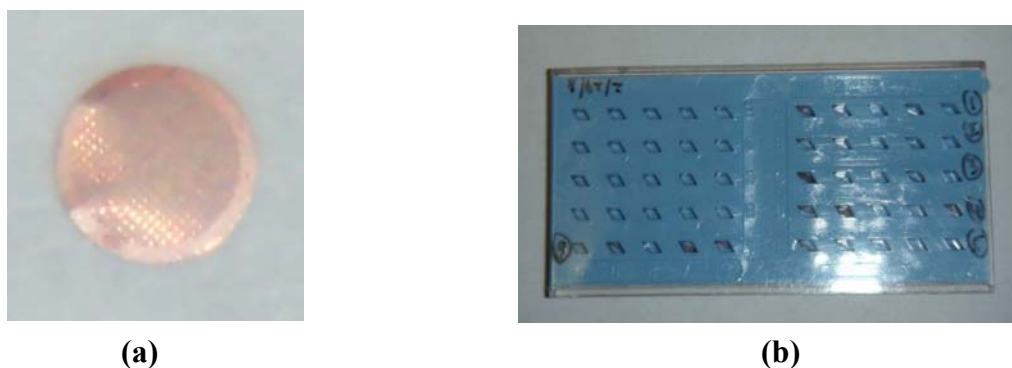
Figure 5.3 (a) Formvar coated 200 mesh copper sample grid; (b) sample holders

5.7.2 TEM analysis

TEM bright field images were obtained using a JOEL JEM-100CX II transmission electron microscope. The highest excitation voltage that can be achieved with the instrument is 100 kV. The pictures were taken with 80 kV~100 kV voltage and the camera focal length was 40 cm. The images were taken with magnifications of 10,000×, 14,000×, 27,000×, 40,000× and 67,000×. The negatives were scanned and examined using the Adobe Photoshop software.

5.8 Scanning electron microscopy

5.8.1 SEM sample preparation

Double sided round mounting tape was placed on aluminum sample stubs. A small amount of sample powder was sprinkled on top of the mounting tape and the stub was tapped to remove excess powder. The sample stubs were labeled and placed in the holders. They were sputter-coated for 10 seconds (manually) with gold and palladium using Polaron E5100 sputter coater, and were kept in the desiccators for further analysis, Fig. 5.4 (a).
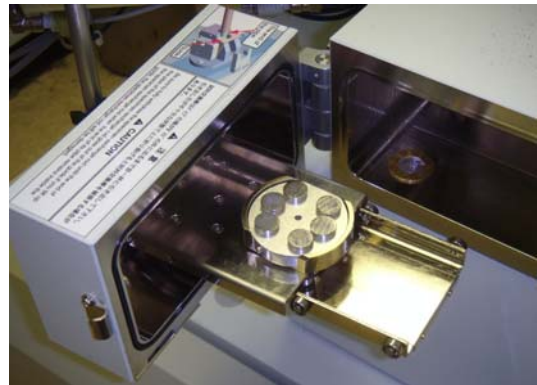
(a)   (b)

Figure 5.4   (a) sputter-coated sample stubs; (b) loading of the samples into SEM.

5.8.2 SEM analysis

SEM images were obtained from using a JOEL JSM-6500F field emission scanning electron microscope. An acceleration voltage of 5.0 kV and a working distance of 15 mm were used to obtain images. The pictures were taken with magnifications of 1,000×, 5,000× and 10,000×. The 1,000× image was taken to get an overall picture of the sample and the special images were enlarged in 10,000× images. The 5,000× images were used to compare the samples, as they gave detailed description about the samples with reproducibility.

REFERENCES

(1)   Lou, X. W.; Wang, Y.; Yuan, C.; Lee, J. Y.; Archer, L. A. *Adv. Mater.*
        2006, *18*, 2325-2329.

(2)   Weakley, B. S. *A Beginner's Handbook in Biological Transmission
        Electron Microscopy*; 2nd ed.; Churchill Livingstone: NY, **1981**.

(3)   Cao, G.; Editor *Nanostructures and Nanomaterials: Synthesis, Properties,
        and Applications*; Imperial College Press: London, **2004**.

(4)   Flegler, S. L.; John, W.; Heckman, J.; Klomparens, K. L. *Scanning and
        Transmission Electron Microscopy an Introduction*; W.H. Freeman and
        Company: NY, **1993**.

CHAPTER VI

RESULTS AND DISCUSSION

Following the works of Archer and coworkers[1] we successfully produced tin

oxide particles from $K_2SnO_3 \cdot 3H_2O$ with one pot hydrothermal synthesis using 23 mL

stainless steel Parr-bombs. The size and morphology of the products was controlled by

using variables listed in Section 5.3. (Table 5.1 and 5.2) The products were characterized

using SEM and TEM.

6.1 SEM data

We produced spherical tin oxide particles with one pot hydrothermal synthesis.

Dried products were analyzed from the field emission scanning electron microscope

(JOEL JSM-6500F) and the results are discussed in the following sections.

6.1.1 SEM of the amines at different temperatures

Tin oxide spheres were obtained in the presence of different alkyl and aryl amines

by varying the reaction temperatures from 120 to 250 $^{\circ}$C. The SEM for 150 $^{\circ}$C and 250

$^{\circ}$C are given in sections 6.1.1.1 and 6.1.1.2, respectively.

6.1.1.1 SEM of the products at 150 ^{o}C

SEM images of products were obtained at magnifications of 1,000×, 5,000× and 10,000×. The products and the sample numbers are listed in Table 6.1.
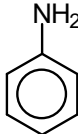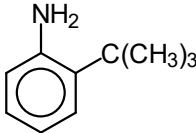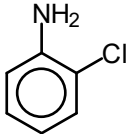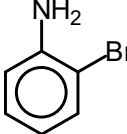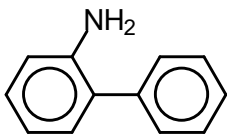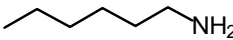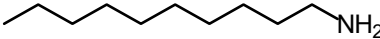
1,000× Results: Based on the images, Fig. 6.1, essentially no difference was observed for samples **2-8** at low magnification.

5,000× Results: Distinct features can be found for the samples. Images for all compounds **2-8** show spherical products with smooth, even surfaces. Average particle sizes were found to be in 3-6 μm range. The amines **2**, **7** and **8** produced similar spherical samples at 150 ^{o}C and the amines **3**, **4** and **5** produced elongated branched type products, Fig. 6.2. The samples were largely intact, that is, the spheres and elongated branched structures were not cracked or broken.

10,000× Results: Higher resolution images of compounds **3**, **4** and **5** show that the elongated particles seem to be formed by growth of spherical particles, Fig. 6.3. Round, even surfaces were observed in all samples.

Table 6.1

List of amines used in hydrothermal synthesis

Sample #	Name	Structure
1	control	no amine used
2	aniline	
3	2-*tert*-butylaniline	
4	2-chloroaniline	
5	2-bromoaniline	
6	2-biphenylamine	
7	hexylamine	
8	decylamine	
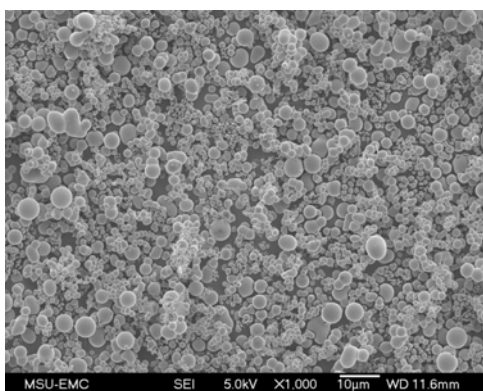
(a)
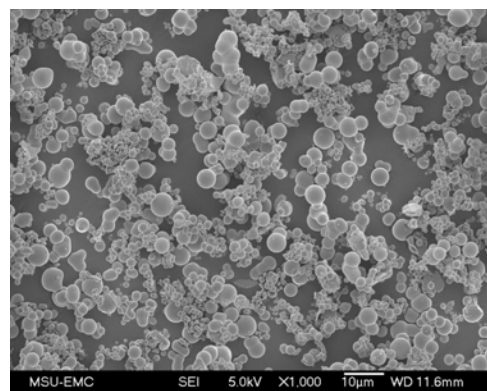
(b)
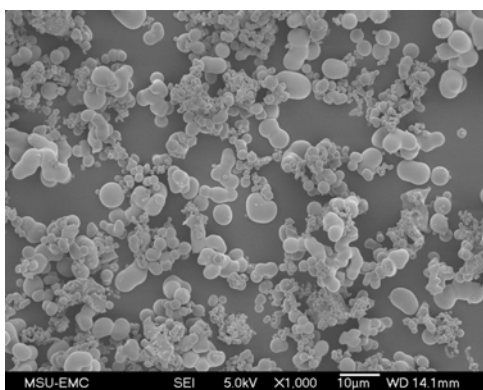
(c)
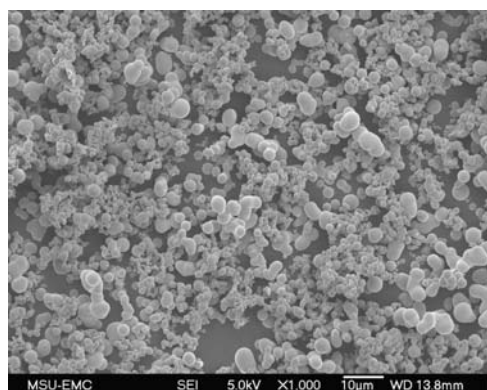
(d)
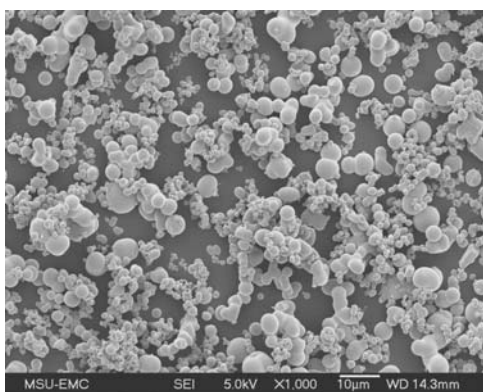
(e)
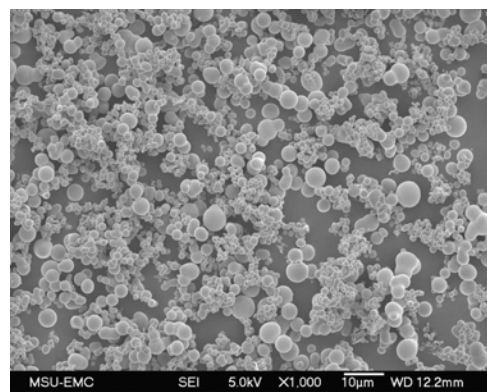
(f)

Figure 6.1   SEM pictures at 1,000× magnification with 150 $^{\circ}$C oven temperature
(a) **2**, (b) **3**, (c) **4,** (d) **5,** (e) **7** and (f) **8**
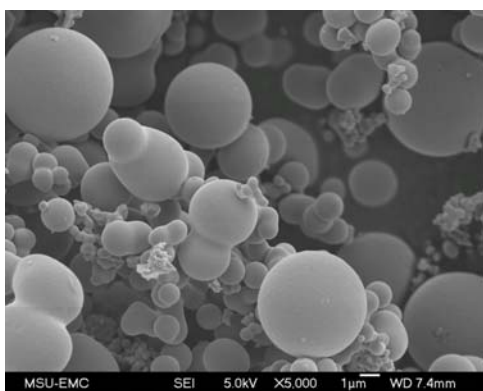
(a)
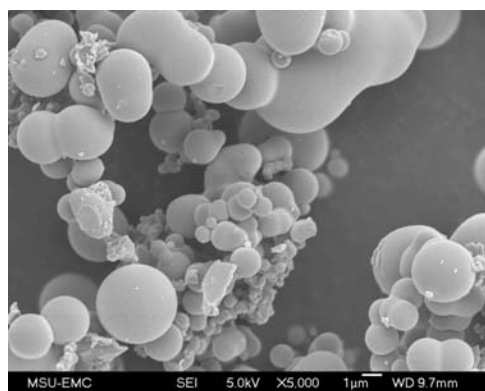
(b)
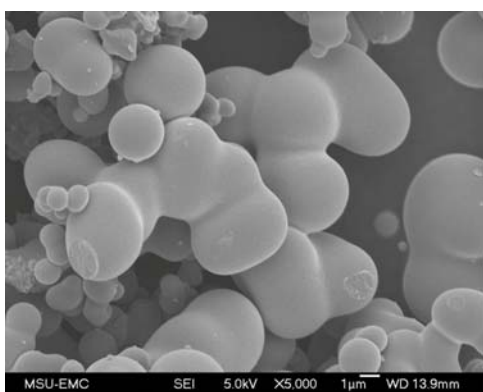
(c)
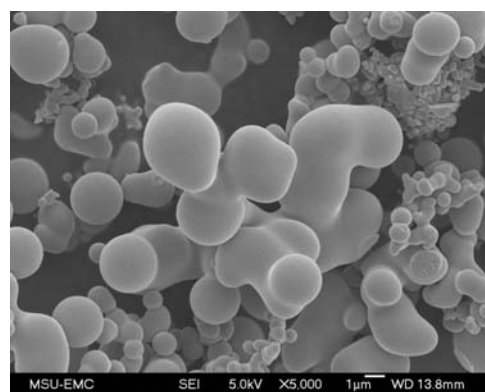
(d)
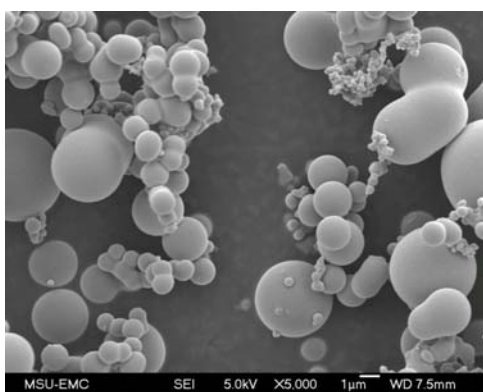
(e)
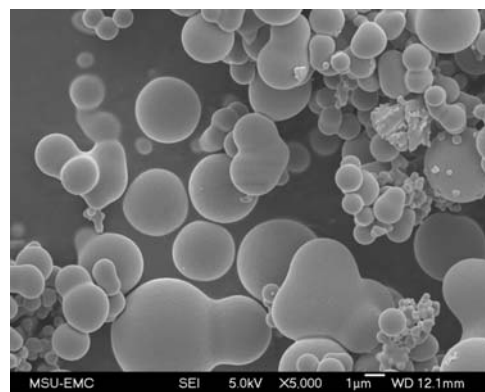
(f)

Figure 6.2   SEM pictures at 5,000× magnification with 150 ^{o}C oven temperature
(a) **2**, (b) **3**, (c) **4,** (d) **5,** (e) **7** and (f) **8**
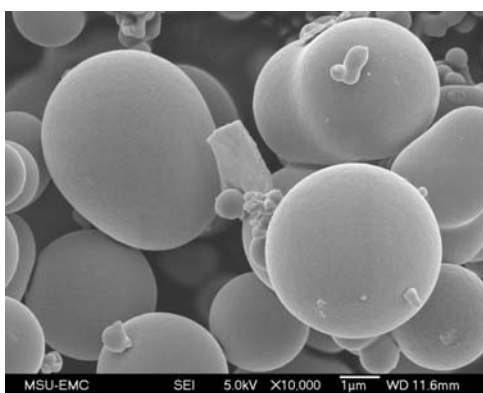
(a)
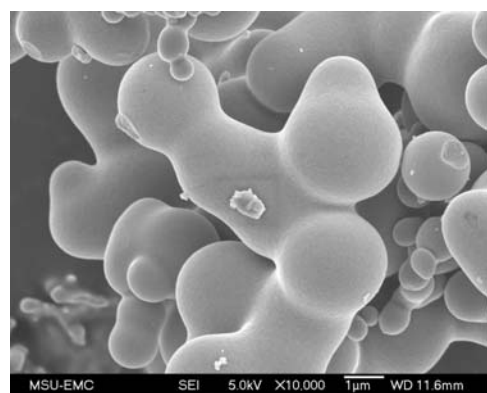
(b)
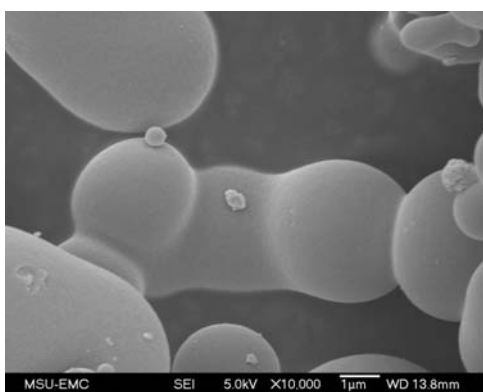
(c)
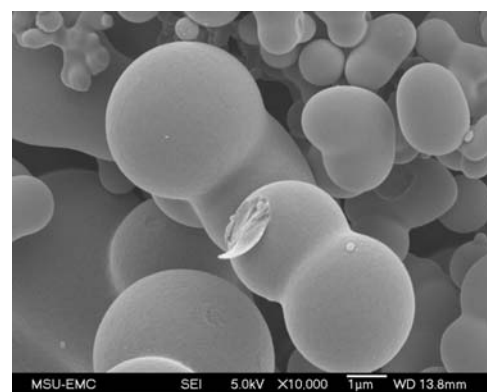
(d)
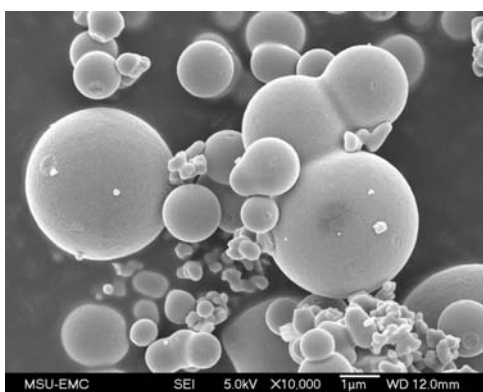
(e)
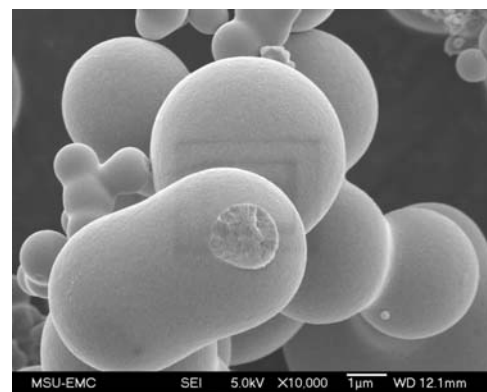
(f)

Figure 6.3　　SEM pictures at 10,000× magnification with 150 $^{\circ}$C oven temperature (a) **2**, (b) **3**, (c) **4,** (d) **5,** (e) **7** and (f) **8**

6.1.1.2 SEM of the products at 250 $^{\circ}$C

Images were obtained at magnifications of 1,000×, 5,000× and 10,000× for the products **1-6**.

1,000× Results: Based on the images, Fig. 6.4, essentially no difference was observed for samples **2-6** at low magnification. However, the control (**1**) and products **2-6** show a significant difference. Sample **1**, which was synthesized without any amine present, is a solid without a distinct shape or sample distribution. Samples **2-5** changed with temperature – at higher temperature the solids were less clumped together than the distribution found in 150 $^{\circ}$C.

5,000× Results: The smooth even spheres observed at lower temperature have changed to uneven surfaces, Fig 6.5. The control and the products show a different level of size distribution. The average size for the products dropped to a 2-4 μm range at 250 $^{\circ}$C. Small broken particles are also found in the samples. The amines **3-6** produce elongated and branched type products, while **2** maintained a spherical shape.

10,000× Results: Few spherical particles can be observed in the control. Sample **2** maintained complete spherical shapes while **3-6** show distorted figures, Fig. 6.6. Sample **6** shows an interesting surface pattern in the elongated structures. Small irregular shaped particles are deposited on the surfaces of the larger particles.
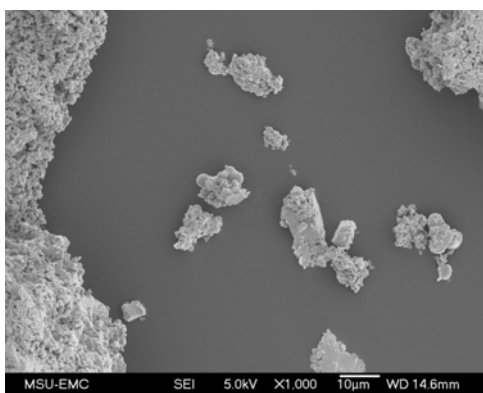
(a)
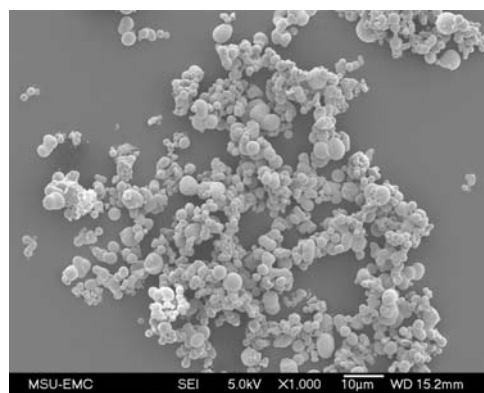
(b)
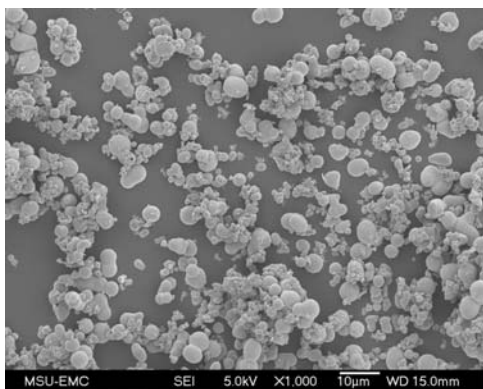
(c)
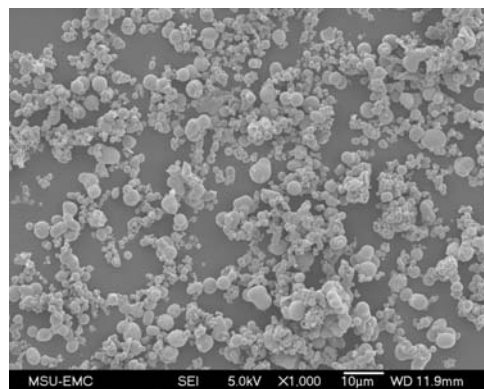
(d)
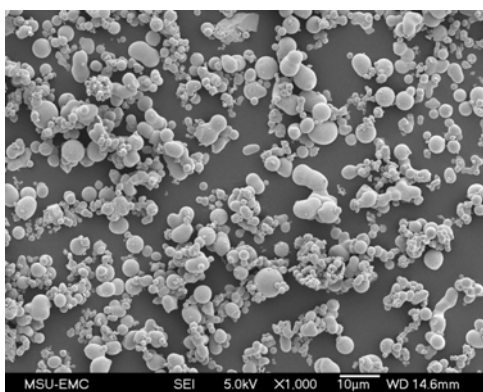
(e)
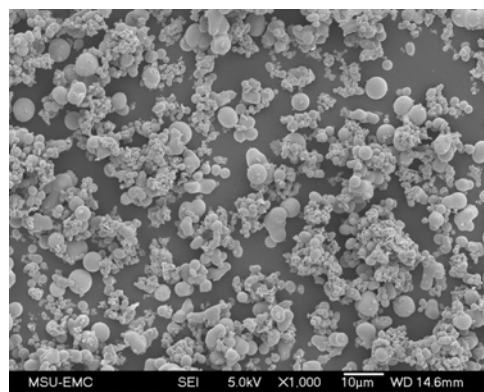
(f)

Figure 6.4   SEM pictures at 1,000× magnification with 250 ^{o}C oven temperature
(a) **1**, (b) **2**, (c) **3**, (d) **4**, (e) **5** and (f) **6**

(a)

(b)
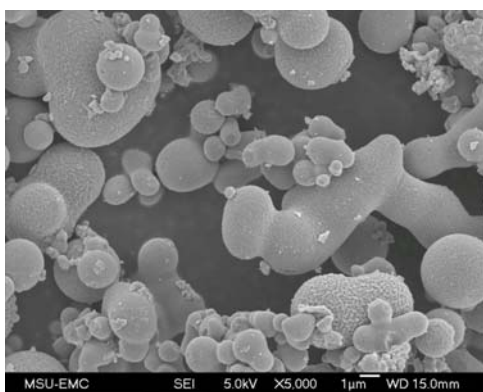
(c)
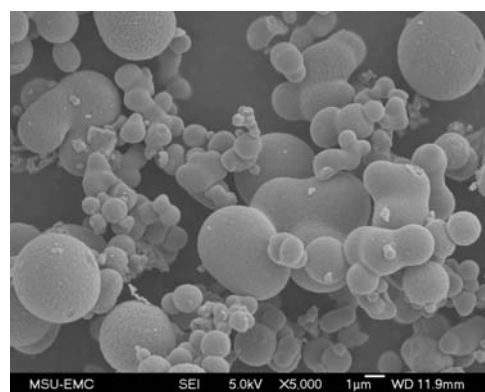
(d)
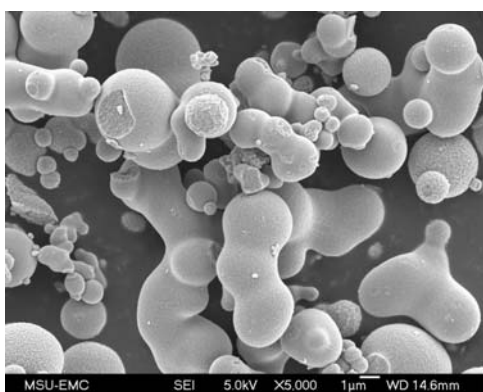
(e)
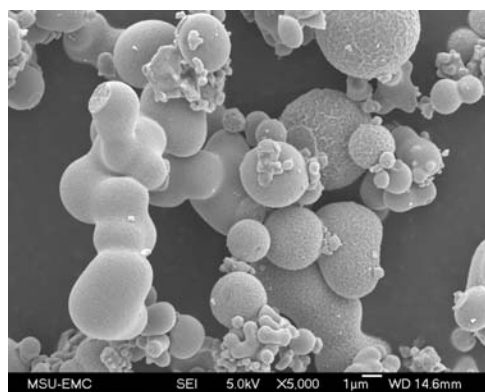
(f)

Figure 6.5   SEM pictures at 5,000× magnification with 250 ^{o}C oven temperature
(a) **1**, (b) **2**, (c) **3**, (d) **4**, (e) **5** and (f) **6**

Figure 6.6   SEM pictures at 10,000× magnification with 250 °C oven temperature
(a) **1**, (b) **2**, (c) **3**, (d) **4**, (e) **5** and (f) **6**

6.1.2 SEM of the amines at different concentrations

The differences in the growth of tin oxide particles based on amine concentrations of 0.1 mmol to 20 mmol were evaluated at 250 ^{o}C. The SEM images at 5,000× magnifications for 0.1 mmol and 20 mmol are shown in Fig. 6.7 and 6.8 respectively. The 4 mmol products were reported in the previous section ((Fig. 6.5 above). Images at 1,000× and 10,000× magnifications of 20 mmol concentration can be found in Appendix D, Fig. D.1 and D.2.

6.1.2.1 SEM of the products at 0.1 mmol amine concentration

Based on the images in Fig. 6.7, at the lower concentration of amines, most samples have retained spherical shapes. However, samples **4** and **6** show elongated structures. A range of size distribution was observed with the products. Comparing the changes from Fig. 6.5 (a) to Fig. 6.7, the size and morphology has changed significantly from the control (**1**) to the introduction of amines. This indicates that even a minute concentration of amines can affect the growth of the tin oxide spheres.
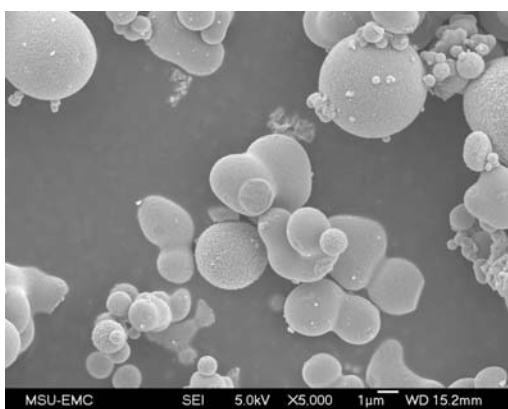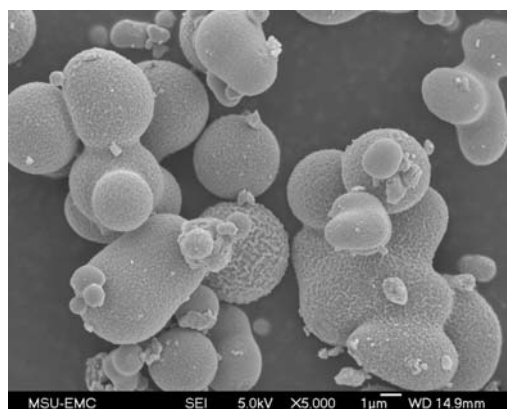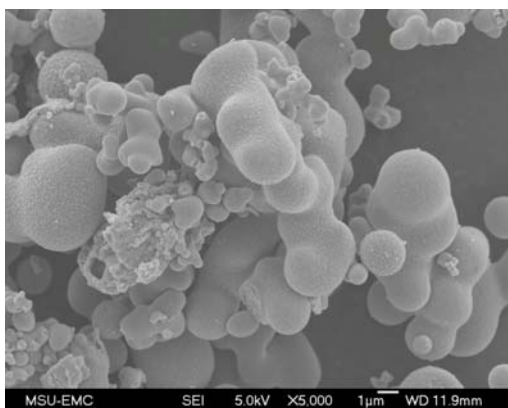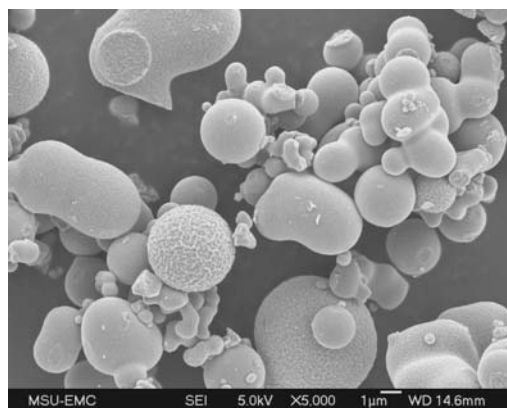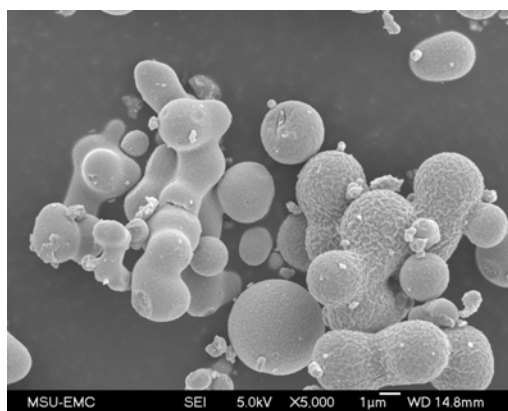
Figure 6.7   The products at 5,000× magnification with 0.1 mmol concentration
(a) **2**, (b) **3**, (c) **4**, (d) **5** and (e) **6**

6.1.2.2 SEM of the products at 4 mmol amine concentration

The size of particles did not appear to change from 0.1 mmol to 4 mmol concentration, Fig. 6.5. However, the shapes of the particles did change. As reported earlier, samples **3-6** produce elongated and branched type products, while **2** remained spherical shaped.

6.1.2.3 SEM of the products at 20 mmol amine concentration

In 20 mmol amine concentration, the particle size has dropped to 1- 2.5 μm, Fig. 6.8. The particles tend to clump together and a higher percentage of broken particles are observed. Sample **6** contains only small irregularly shaped particles, and no signs of spherical products are observed. In samples **2** and **4**, a flat growth of particles is also observed. In **4** and **5**, some opened up spheres are present and the hollowness of the particles can be observed from them.
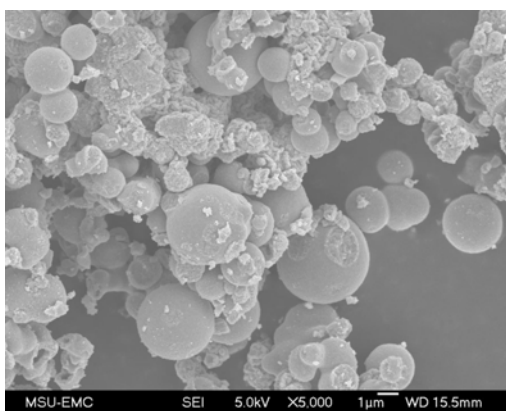
(a)
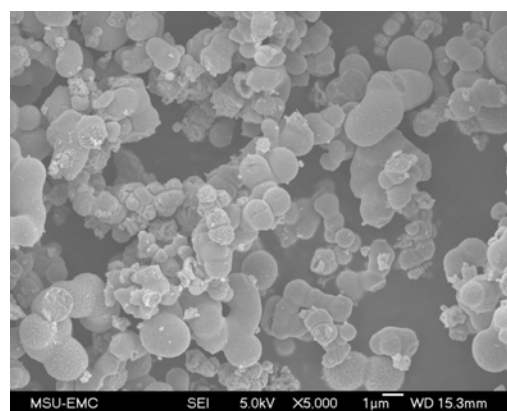
(b)
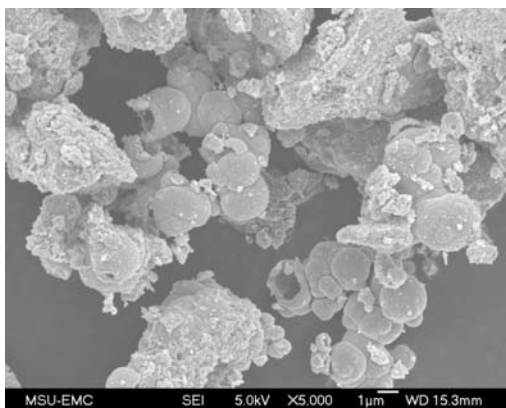
(c)
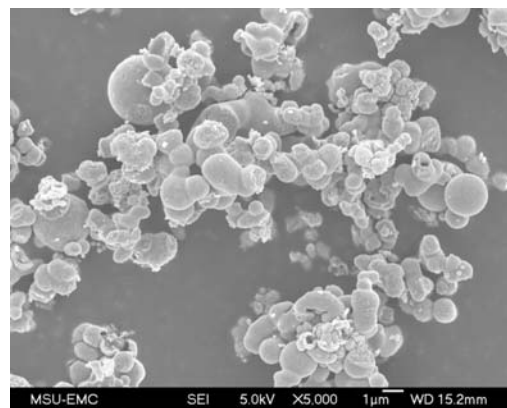
(d)
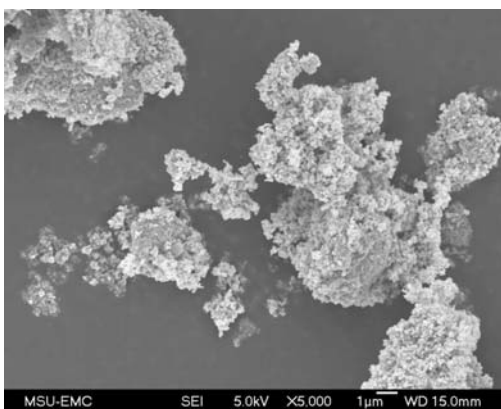
(e)

Figure 6.8   The products at 5,000× magnification with 20 mmol concentration
              (a) **2**, (b) **3**, (c) **4**, (d) **5** and (e) **6**

The gradual increase of amine concentrations (0.1 mmol - 4 mmol) has not shown difference in the size of the products. However, 4 mmol samples indicated characteristic shapes for the particles depending on the amines, where in 0.1 mmol samples remained spherical. In 4 mmol concentration aniline (**2**), the product was spherical, **3** and **6** were elongated and **4** and **5** showed a branched type growth. Dramatically increasing the amine concentration (to 20 mmol) affected the appearance of the particles significantly for all products, especially for sample **6**. The average size of the particles dropped with the increase of concentration and mostly irregular shaped products were obtained.

6.1.3 SEM of amines at different reaction times

The duration of reaction is varied from 30 min to 1 week in the hydrothermal synthesis to observe the effect for growth of particles. These results were reported at two different temperature levels (150 ^{o}C and 250 ^{o}C) and a constant amine concentration (0.4 mmol). The SEM images at 5,000× magnification for the 20 h and 67 h products are shown in Fig. 6.9 to 6.12. The 1,000×, 10,000× magnifications can be found in Appendix D Fig. D.3 - D.10. The 3hrs reaction time images for 150 ^{o}C and 250 ^{o}C are given in Fig. 6.1 - 6.6.

6.1.3.1 SEM of the products with 3 h of reaction time at 150 ^{o}C

As discussed earlier in Section 6.1.1.1, the 1,000× magnified images (Fig. 6.1) of samples reacted for 3 h at 150 ^{o}C did not show any changes with the different amines. However, from the 5,000× and 10,000× magnified images (Fig. 6.2 and 6.3) different growth patterns were observed depending on the amines used.

6.1.3.2 SEM of the products with 20 h of reaction time at 150 ^{o}C

Based on the images, Fig. 6.9, it can be seen that most samples have similar growth patterns observed for lower reaction time. The shapes and surface smoothness does not change by increasing the reaction time to 20 h.

6.1.3.3 SEM of the products with 67 h of reaction time at 150 ^{o}C

Even at 67 h reaction time, Fig. 6.10, the 150 ^{o}C temperature systems did not change significantly compared to the lower reaction time products. Few irregular shaped smaller particles were seen at samples, but overall smooth even surfaces can be observed in all samples from **2-5**.
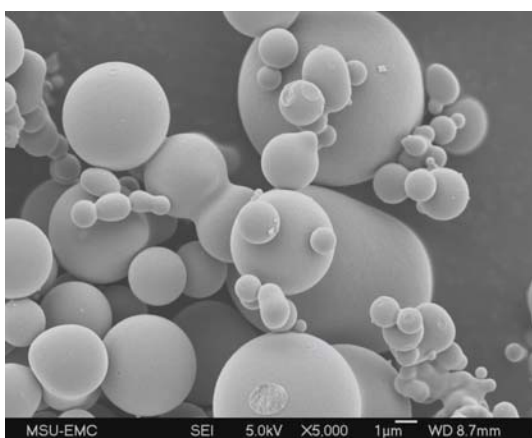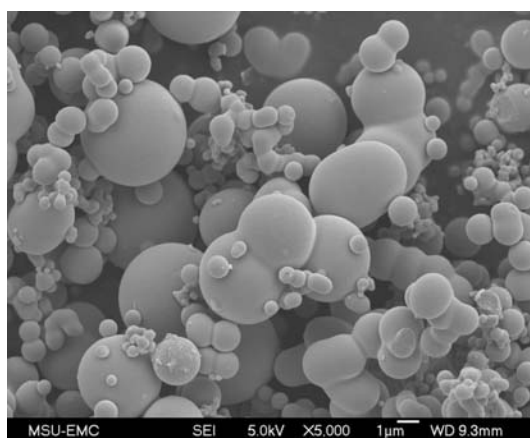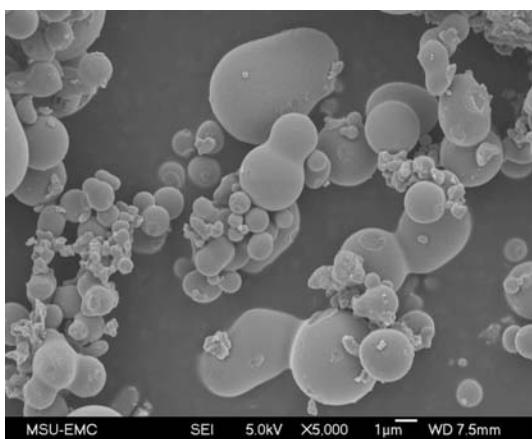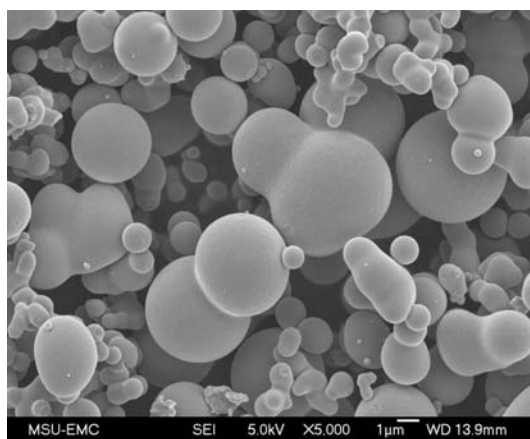
Figure 6.9   The products at 5,000× magnification with 20 h reaction time at 150 $^{\circ}$C (a) **2**, (b) **3**, (c) **4** and (d) **5**
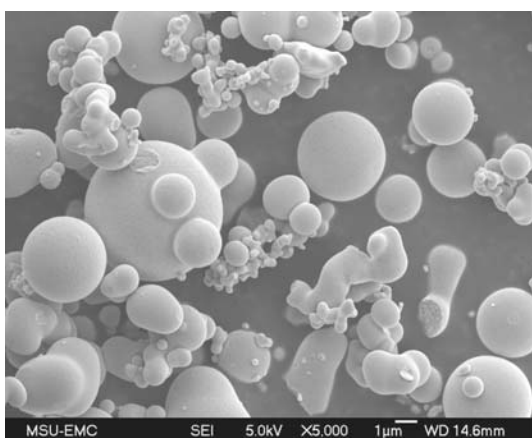
(a)
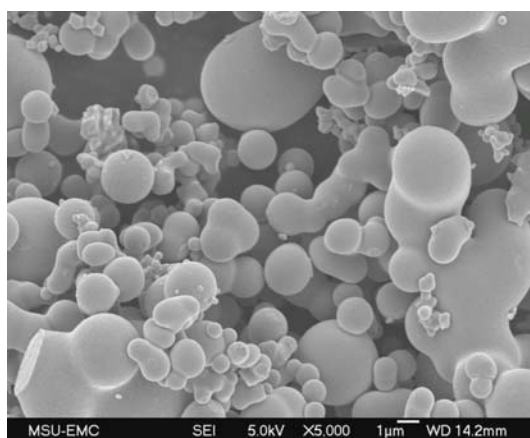
(b)
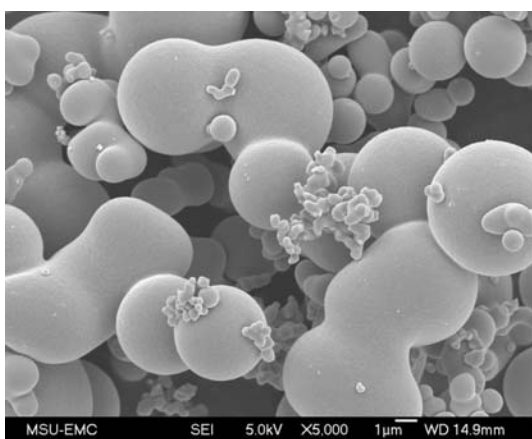
(c)
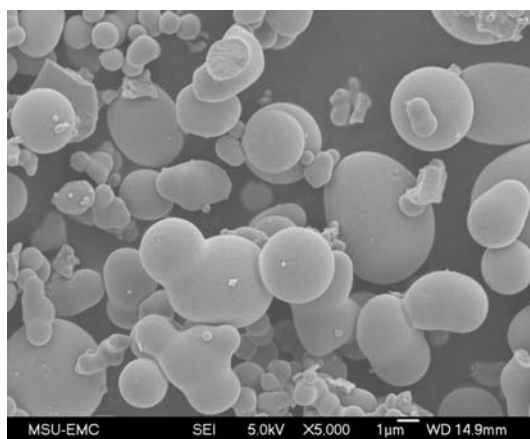
(d)

Figure 6.10   The products at 5,000× magnification with 67 h reaction time at 150 ^{o}C
(a) **2**, (b) **3**, (c) **4** and (d) **5**

6.1.3.4 SEM of the products with 3 h of reaction time at 250 $^{\circ}$C

As discussed earlier in the Section 6.1.1.2, the 5,000× magnified images of 3 h reaction time at 250 $^{\circ}$C temperature (Fig. 6.5), the smoothness of the surfaces has changed to uneven, rough patches. The amines in **3**-**6** produced elongated and branched type products, while there is a spherical shape for **2**.

6.1.3.5 SEM of the products with 20 h of reaction time at 250 $^{\circ}$C

Based on images from Fig. 6.11, the appearance of the samples changed significantly with the reaction time from 3 h to 20 h, except in **5**. In samples **3** and **4**, the spherical products were hardly recognizable, as these products were covered with small irregular shaped particles. Sample **6** showed some broken spheres, which allowed the thickness of the inner walls to be observed.

6.1.3.6 SEM of the products with 67 h of reaction time at 250 $^{\circ}$C

At 67 h of reaction time, all products except for sample **2** were covered with small irregular shaped particles. (Fig. 6.12) Characteristic growth patterns for different amines (elongated or branched) cannot be identified from these samples. Sample **3** contained the most irregularities in the products for the 67 h at 250 $^{\circ}$C reaction time, where silk cocoon type growth was indicated from the samples.
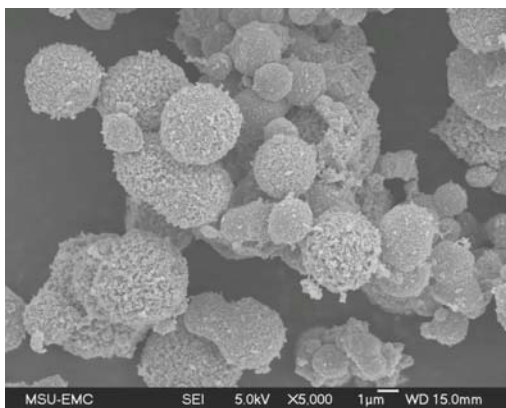
(a)
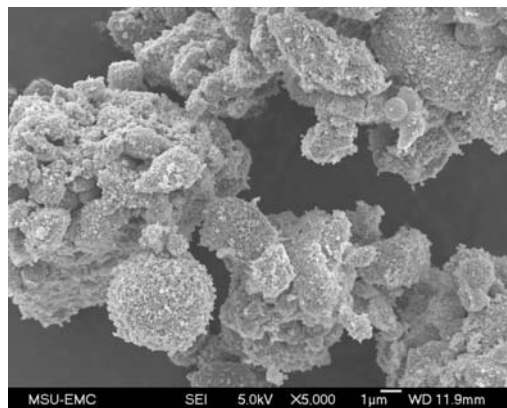
(b)
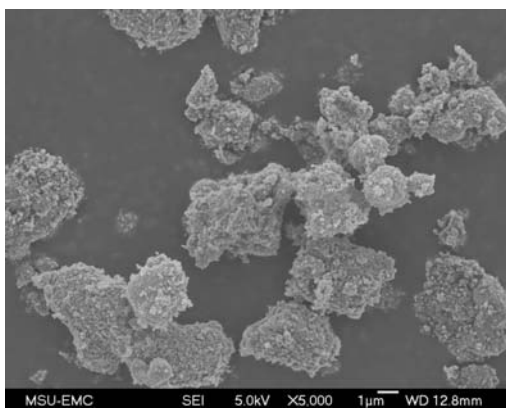
(c)
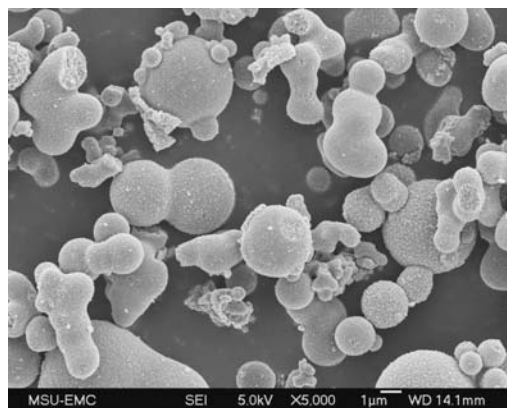
(d)
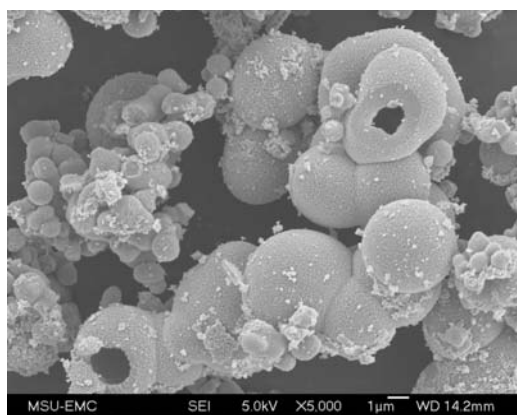
(e)

Figure 6.11   The products at 5,000× magnification with 20 h reaction time at 250 ^{o}C
(a) **2**, (b) **3**, (c) **4,** (d) **5** and (e) **6**
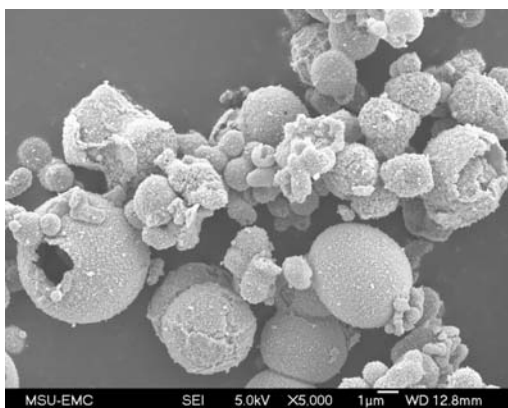
(a)
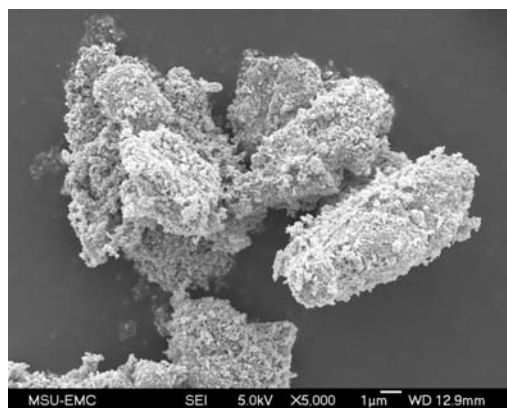
(b)
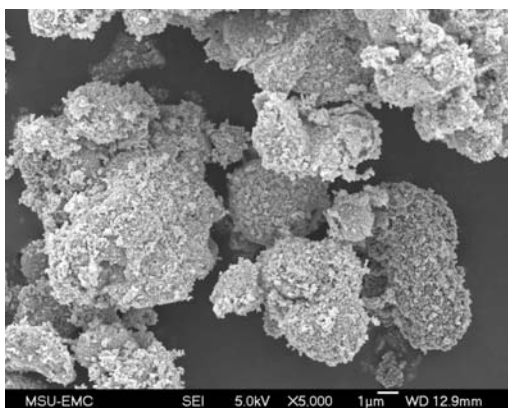
(c)
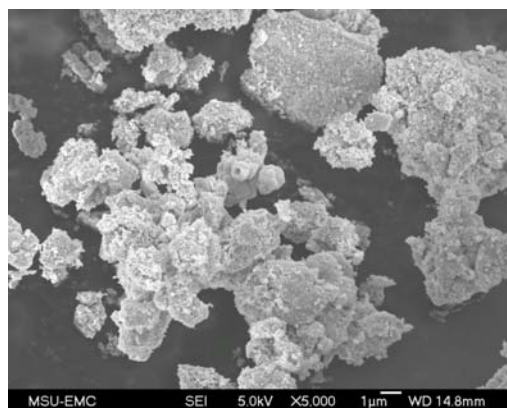
(d)
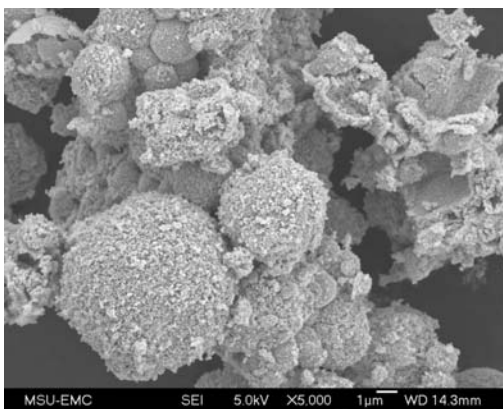
(e)

Figure 6.12   The products at 5,000× magnification with 67 h reaction time at 250 ^{o}C
(a) **2**, (b) **3**, (c) **4,** (d) **5** and (e) **6**

Overall, it can be noted that the reaction time is an important parameter for developing spherical tin oxide particles, along with the reaction temperature. At lower temperatures, longer reaction times did not seem to affect the size of the particles. However, for higher temperatures reaction time was a vital factor for particle growth.

6.1.4 Overall results for SEM of samples with different amines

The amines used in the reactions were varied according to the Table 6.1. Constant temperature of 250 °C, 3 h reaction time and 4 mmol amine concentration was maintained for all the systems.

According to the Fig 6.4 (a), 6.5 (b) and 6.6 (a), when amines are not present (the control, Sample **1**) the solid is more irregularly shaped. However, there were some spherical particles observed in SEM of sample **1**. Overall, **1** showed significant deviations from the growth patterns observed in the samples in which amines were used as additives.

Two unbranched alkyl amine systems used (hexylamine and decylamine) displayed a spherical growth of products in sample **7** and **8**.

Compounds **2-6** discussed above are based on reactions performed with anilines and *ortho*-substituted anilines, to determine the effect of the nature and size of the substituent on particle growth. While aniline (**2**, *ortho* substituent = H) gave essentially the same results as the alkyl-based amines discussed above. Some differences were observed in *t*-butyl- (**3**) *vs*. halide- (**4, 5**) substituted anilines and the 2-biphenylamine (**6**).

The SEM images of the products **3**, **4** and **6** at 1,000×, 5,000× and 10,000×

magnifications are shown below.

6.1.4.1 Tin oxides grown with 2-*tert*-butylaniline

The introduction of the *t*-butyl-substituted aniline (**3**) changed the growth of the

tin oxides dramatically. The extended tubular type growth was observed, Figure 6.13.

However, still there were about 40-50% of isolated spherical type particles. The diameter

of the spheres remained in 1-3 μm range, and the extended tubular structures had the

lengths of 10-15 μm.
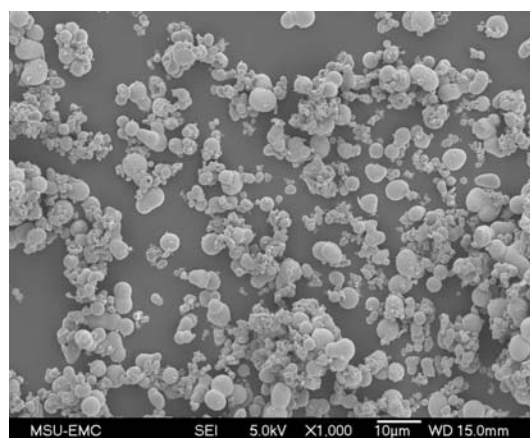
(a)
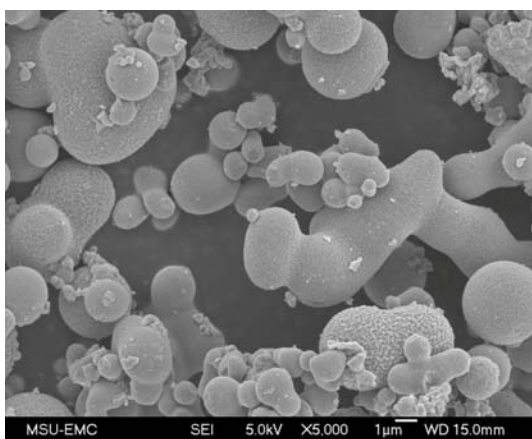
(b)
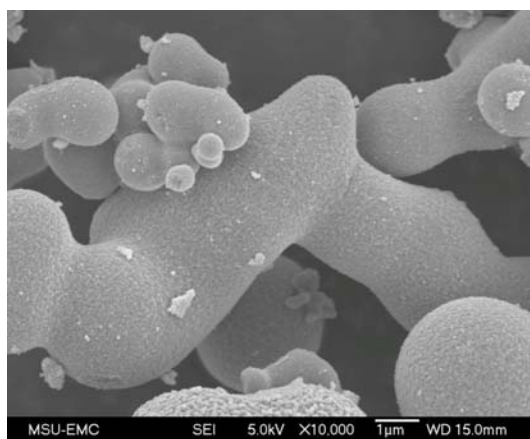
(c)

Figure 6.13   SEM images of **3**; (a) magnification of 1,000×, (b) 5,000× and (c) 10,000×

6.1.4.2 Tin oxides grown with halide-substituted anilines

The introduction of *ortho* chloro- or bromo- groups has encouraged a distorted spherical growth of tin oxide particles. A high percentage (60-70%) of triangular and branched type particles were observed in the samples and only a small number of completely round particles were seen. Large oval- and star-type species were also observed. Representative images from particles grown in the presence of chloro-substituted aniline (**4**) are shown in Figure 6.14.

6.1.4.3 Tin oxides particles grown in the presence of 2-biphenylamine

Biphenylamine had the most bulky *ortho* functional group. The phenyl ring at the 2-position has changed the growth of the tin oxides remarkably – Fig. 6.15 shows the long, twisted, unbranched type of particles seen in the sample. There was a considerable amount (15-20%) of irregularly shaped small particles seen in the sample. Therefore, a wide range of particle distribution (50 nm-10 μm) was observed. The long chain-like particles (15-25 μm) observed in these samples were much larger than the ones in product **3** (with the bulky *t*-butyl group).
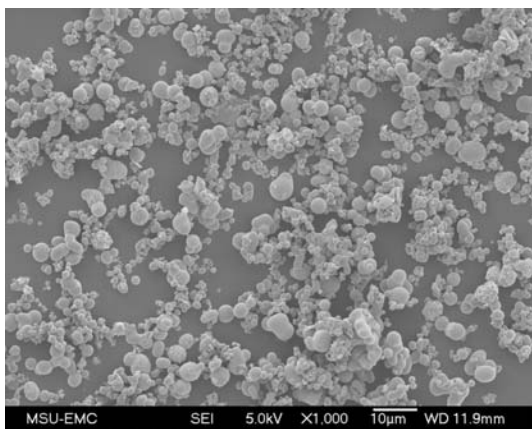
(a)
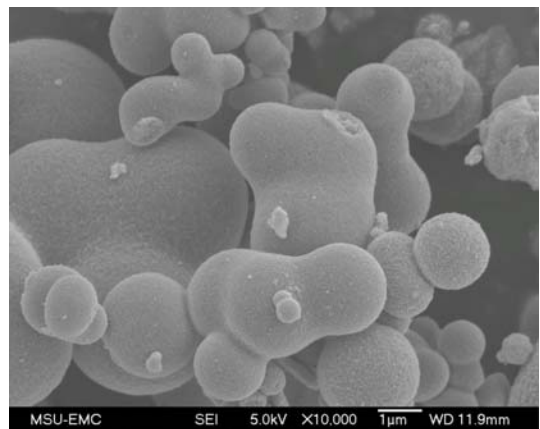
(b)

Figure 6.14   SEM images of **4**; (a) magnification of 1,000×, and (b) 10,000×
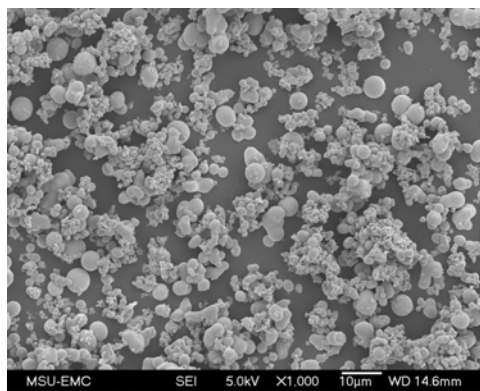
(a)
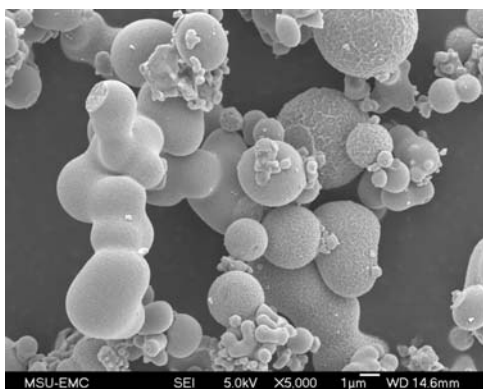
(b)
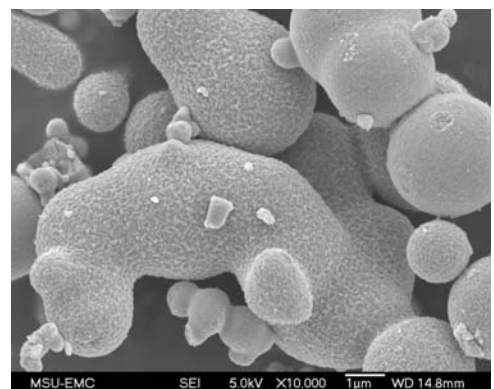
(c)

Figure 6.15   SEM images of **6**; (a) magnification of 1,000×, (b) 5,000× and (c) 10,000×

We have demonstrated that the growth of the tin oxide particles can be changed by using different amines in the synthesis. Especially the steric tuning of the *ortho* functional groups proved to change growth behavior in tin oxide particles, as the samples **3-6** clearly deviated from the aniline sample (**2**). In the presence of bulkier *ortho* groups [*tert*-butyl (**3**) and 2-phenyl (**6**)], elongated connecting structures were observed. With the use of halogen functional groups in the 2-position [chloro (**4**) and bromo (**5**)], branched and triangular type growth is promoted. The results were consistent for a number of trials.

6.2 TEM data

The surface characteristics can be thoroughly explored from SEM. The TEM experiments were done to get answers for three main questions regarding the growth of tin oxides: 1.hollowness of the particles, 2.wall thickness of the spheres and 3.the connectivity of the inner walls. Bright field images of products were obtained from JOEL JEM-100CX II transmission electron microscope at magnifications of 10,000×, 14,000×, 20,000×, 40,000× and 67,000×.

Unfortunately, the electron beam was unable to penetrate the sample walls even at the maximum voltage of 100 kV. Therefore, we were not able to gain information about the inner structure in the samples. However, the preferred shapes and sizes of the particles with the presence of different amines can be viewed from TEM (Fig. 6.16) and confirmed the observations in SEM.
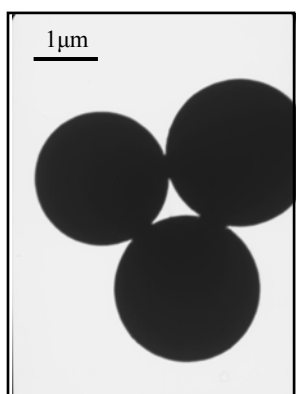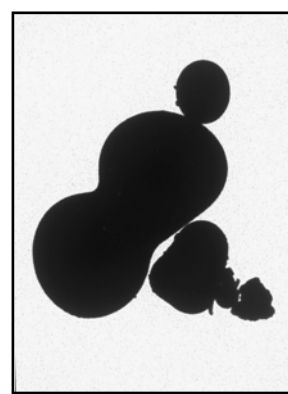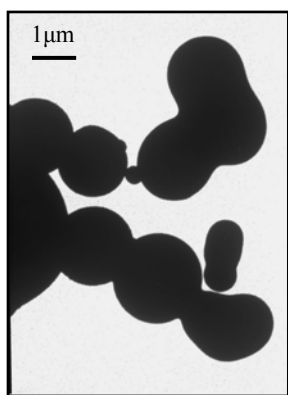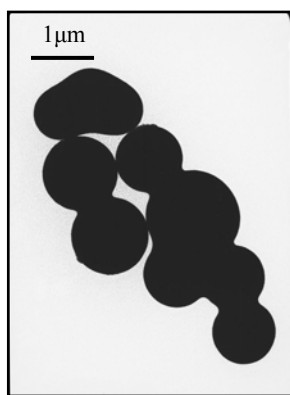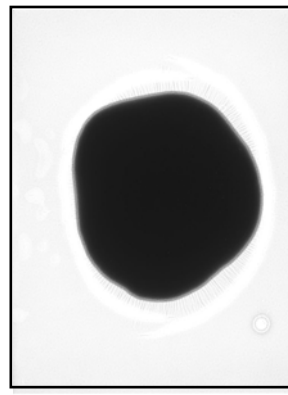
Figure 6.16   TEM bright field images of samples:
(a) **2** (14,000×), (b) **3** (20,000×), (c) **4** (10,000×), (d) **5** (10,000×),
(e) **7** (14,000×) (f) **8** (14,000×).

According to the TEM micrographs, the spherical shapes of samples **2**, **8** and the extended structures of samples **3-5** can be observed, Fig. 6.16.

6.3 Evidence for the hollowness of the products

TEM was not able to penetrate the outer surface of the particles. Treatments were done during the imaging to improve the penetration. Samples were exposed with longer time frame and high temperature to allowing the particles to break. Representative images for these over exposed samples are shown in Fig. 6.17. Evidence was not obtained from TEM micrographs with regard to the hollowness of the particles.

(a)   **(b)**
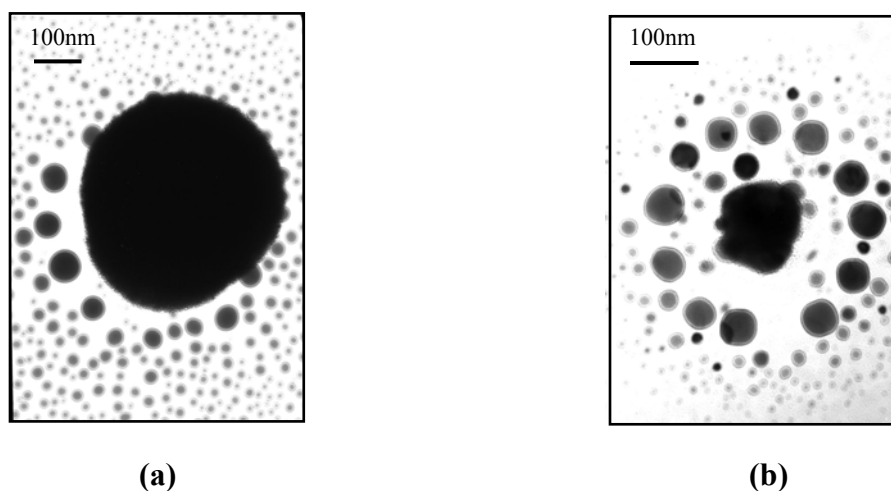
Figure 6.17   Overexposed TEM images of **4**: (a) at 100,000×, and (b) 140,000×.

However, SEM images taken at harsher conditions (high temperature, long reaction time and high concentration) have created openings in the spherical products, Table 6.2. Sample **3**, did not show any sphere breakage under any conditions. Representative images for these **2** and **4** are shown in Figure 6.18.

Table 6.2

Samples which produce evidence for hollow cavities

sample	temperature	concentration	reaction time
2	250 ^{o}C	4 mmol	20 h
2	250 ^{o}C	4 mmol	67 h
2	250 ^{o}C	20 mmol	3 h
4	250 ^{o}C	20 mmol	3 h
5	250 ^{o}C	4 mmol	67 h
6	250 ^{o}C	4 mmol	20 h
6	250 ^{o}C	4 mmol	67 h
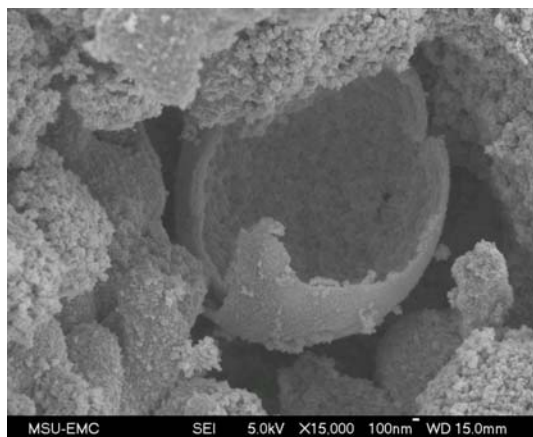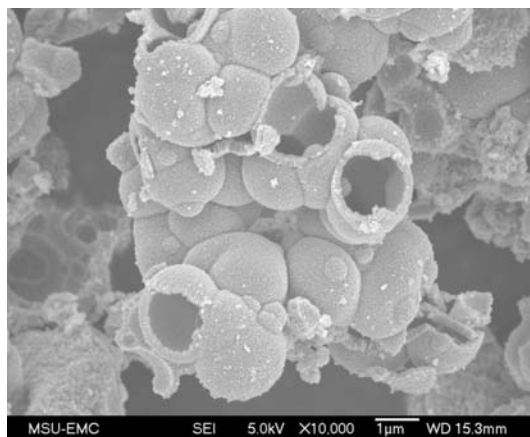
(a)   **(b)**

Figure 6.18   SEM pictures with hollow cavities (a) **2** (250 $^{\circ}$C, 4 mmol, 20 h)
              (b) **4** (250 $^{\circ}$C, 20 mmol, 3 h)
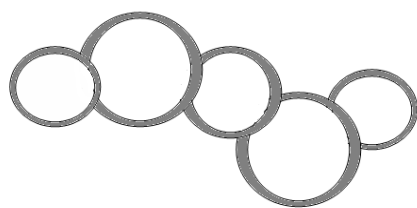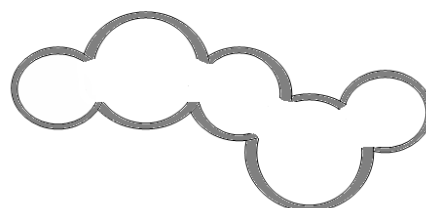
(A)   **(B)**

Figure 6.19   Two possible ways for hollow spheres to connect

The images of Fig. 6.18 show hollow particles with rough inner surfaces. The inner wall thickness can be estimated be in 50-200 nm range, which evidently is too thick to for a TEM electron beam of 100 kV to penetrate. In the literature, evidence of hollowness for smaller particles were reported using TEM instruments with 120 kV or higher.[2,3]

The connectivity of the particles can not be predicted from the existing data. Whether the elongated structures contain walls in between the spheres, Fig. 6.19 (A), or they remain hollow throughout the structure, (Fig. 6.19 (B)) is a question to be answered in the future using a TEM instrument with a high-voltage electron beam. However, it is clear that forming tin-oxide particles in the presence of anilines containing bulky *ortho* substituents do change the particle morphologies.

REFERENCES

(1)   Lou, X. W.; Wang, Y.; Yuan, C.; Lee, J. Y.; Archer, L. A. *Adv. Mater.* **2006**, *18*, 2325-2329.

(2)   Zha, L.; Zhang, Y.; Yang, W.; Fu, S. *Adv. Mater.* **2002**, *14*, 1090-1092.

(3)   Caruso, F.; Caruso, R. A.; Moehwald, H. *Science* **1998**, *282*, 1111-1114.

CHAPTER VII

CONCLUSION

We have successfully synthesized tin oxides particles in high yield using "template-free" one pot hydrothermal synthesis. The products were analyzed by SEM and TEM techniques. The SEM images provided an overall picture with detailed information about surface morphology, size and thickness. TEM analysis was not successful due to the inability to penetrate the samples from the electron beam. For future work use of a high voltage (>120 kV) TEM device is recommended.

The growth of tin oxide particles was affected by the change of reaction temperature, reaction time, starting material concentration and the nature of the amine substituents used in the hydrothermal synthesis. Higher temperature and longer reaction time resulted in smaller size particles with uneven surfaces compared to the smooth spheres observed at lower temperatures. The dimensionality of the spheres decreased from 3-6 μm to 2-4 μm when the temperature increased from 150 to 250 ^{o}C. The amine concentration becomes an influencing factor for the particle growth only after increasing the concentration (>20 mmol). The increase in concentration results in small, irregularly shaped pieces rather than spherical particles.

The nature of the amines played a vital role in this "template-free" synthesis. Aniline (**2**) and alkyl amines (**7** and **8**) facilitated spherical growth of tin oxides. The change of functional groups in *ortho* position in aniline created a variety of different

110

shaped tin oxide products. The halogen groups promoted a branched and triangular type growth (**4** and **5**), where *tert*-butyl and phenyl groups have produced elongated and twisted type tin oxide particles (**3** and **6**). This has shown that the original hypothesis, that the steric tuning of *ortho* substituted anilines can affect the size/shape of micron-sized metal oxide particles similar to the effect observed in metal halide cluster synthesis.

The different shapes and sizes of tin oxide particles produced here can be studied for developing molecular sensors, storage devices and electrode materials. An electrochemical study to evaluate the relationship between size and morphology *vs.* electrode potential can be suggested as a future work.

APPENDIX A

THERMOGRAVIMETRIC ANALYSIS
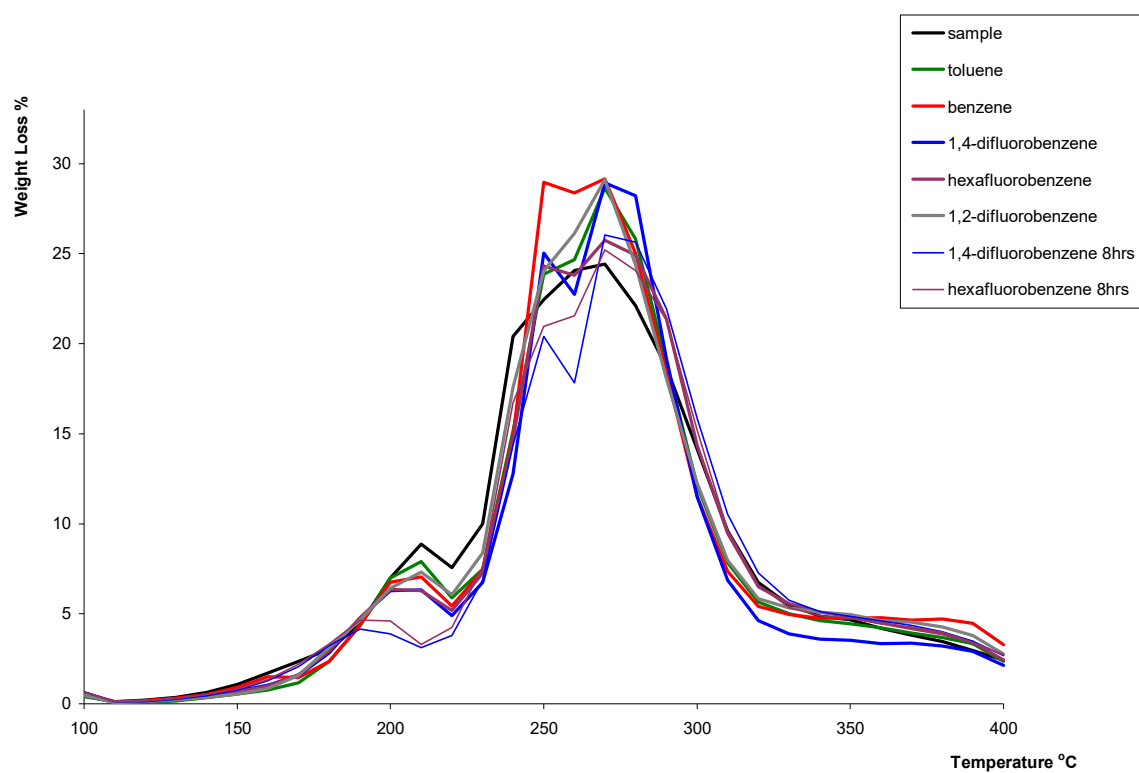
Figure A.1　　Partial weight loss percentages of **2** with 3 h and 8 h sonications of toluene, benzene, 1,4-difluorobenzene in toluene, hexafluorobenzene in toluene and 1,2-difluorobenzene in toluene.
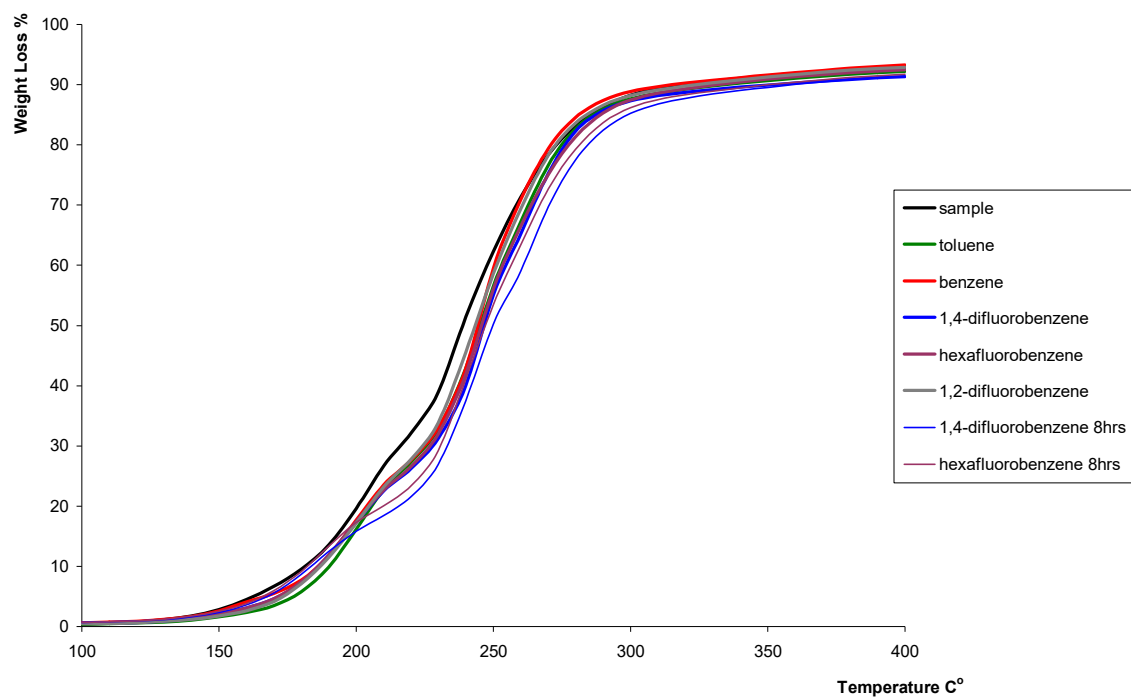
Figure A.2   Total weight loss percentages of **2** with 3 h and 8 h sonications of toluene, benzene, 1,4-difluorobenzene in toluene, hexafluorobenzene in toluene and 1,2-difluorobenzene in toluene.
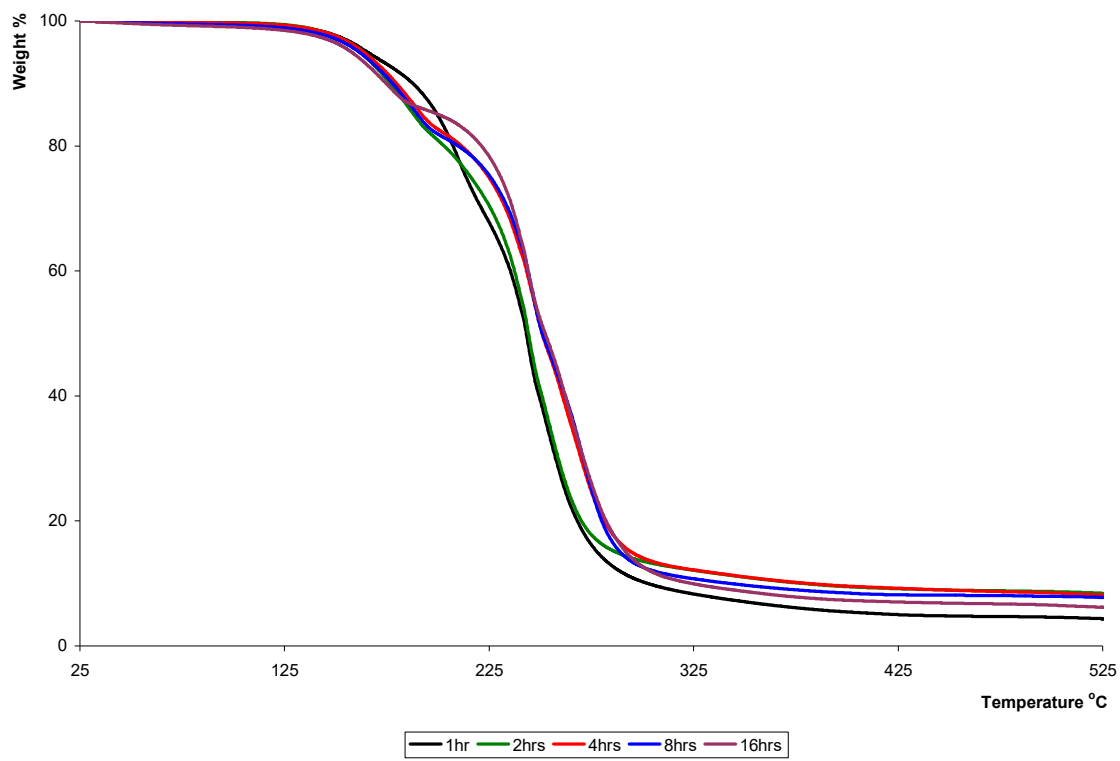
Figure A.3   TGA of **2** sonicated with toluene for 1 h, 2 h, 4 h, 8 h and 16 h.
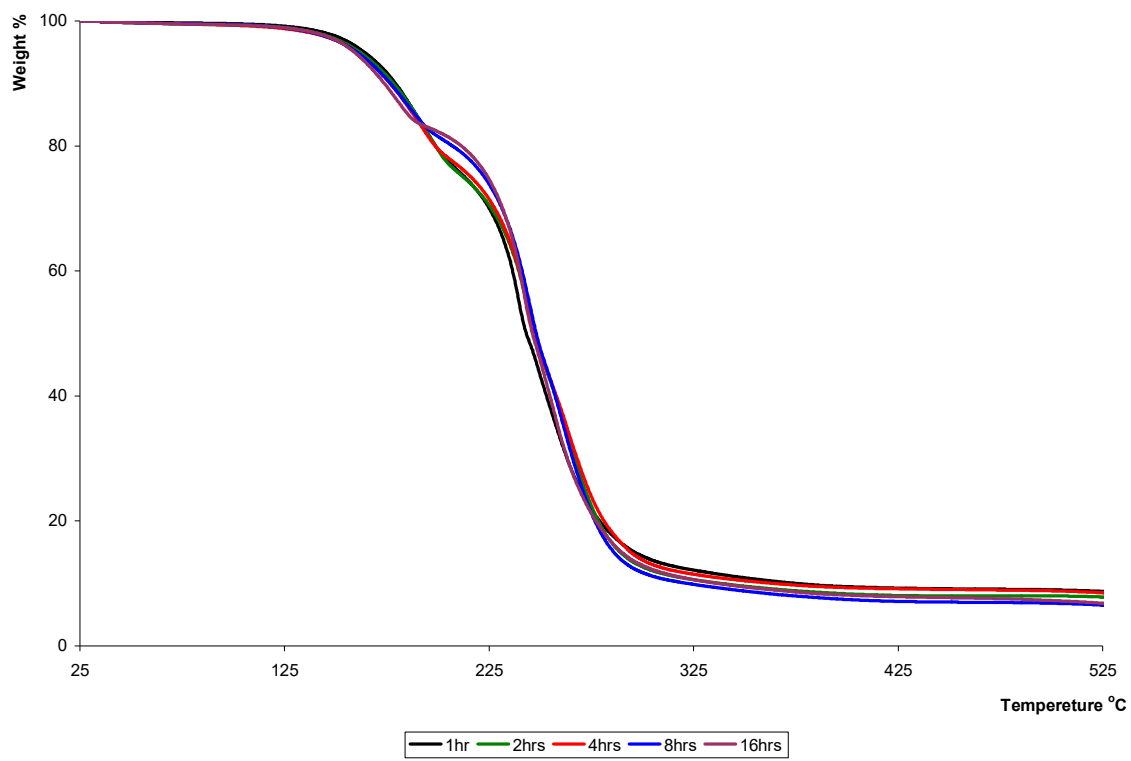
Figure A.4   TGA of **2** sonicated with hexafluorobenzene in toluene for 1 h, 2 h, 4 h, 8 h and 16 h.
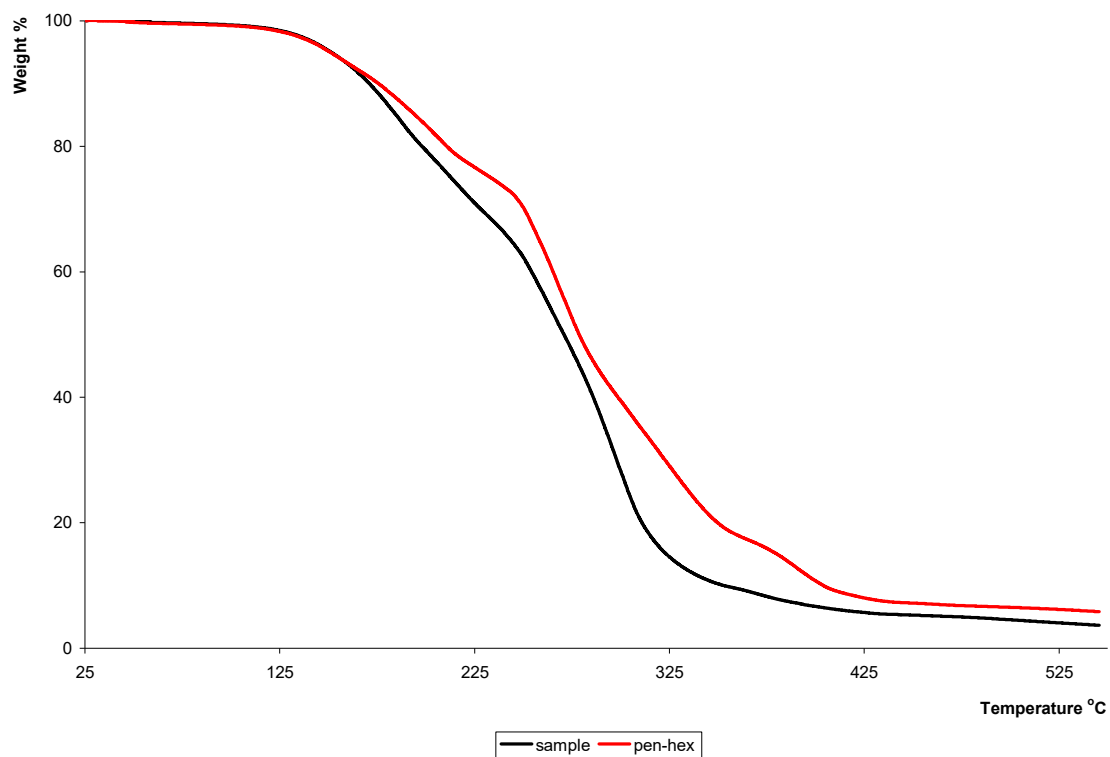
Figure A.5   TGA of **7** sonicated with hexane in pentane.
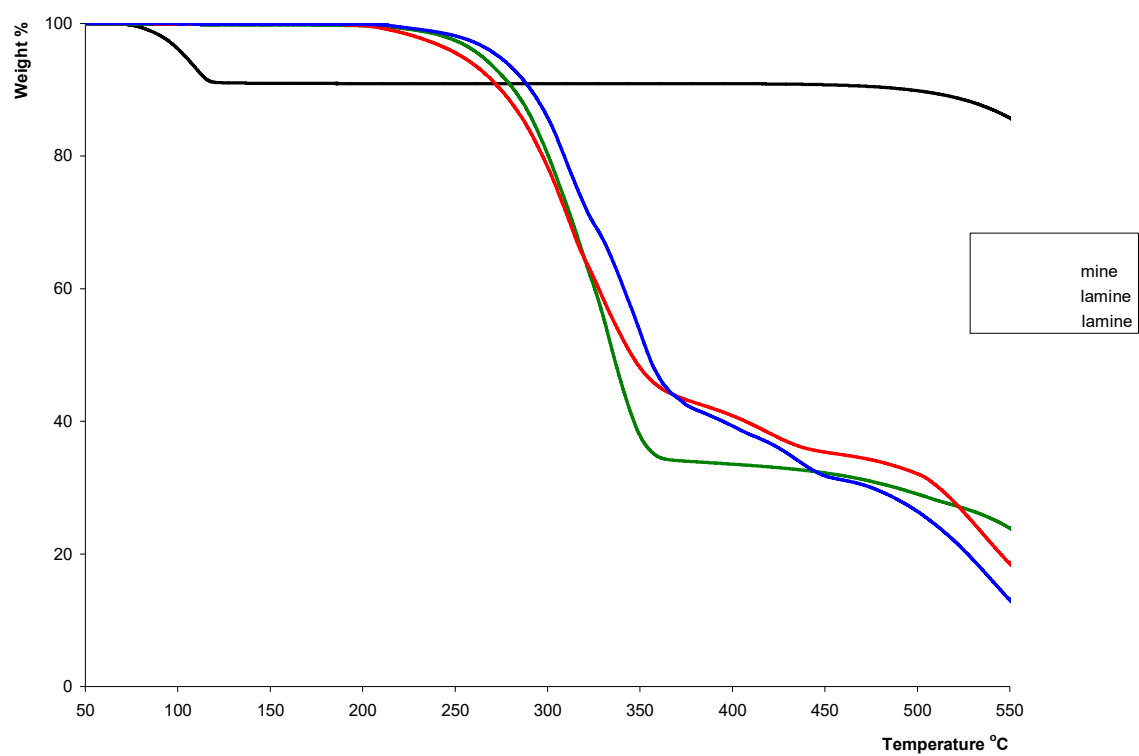
Figure A.6   TGA of **11**, **12** and **13**.

APPENDIX B

BRAGG'S LAW

Bragg's Law[1] was derived from the diffraction studies conducted by Sir William Lawrance Bragg in 1912. It is a widely used equation in X-ray diffraction studies to calculate the d-spacing of the layered materials. Bragg's equation can be denoted as;

$$n\lambda = 2d \sin \theta$$

Where,

θ - glancing angle,

d - layer separation

λ - wave length

n - order of the reflection

REFERENCES

(1)   Atkins, P. W. *Physical Chemistry. 6rd Ed*; Oxford university Press: Oxford, 1998.

APPENDIX C

POWDER X-RAY SPECTROSCOPY
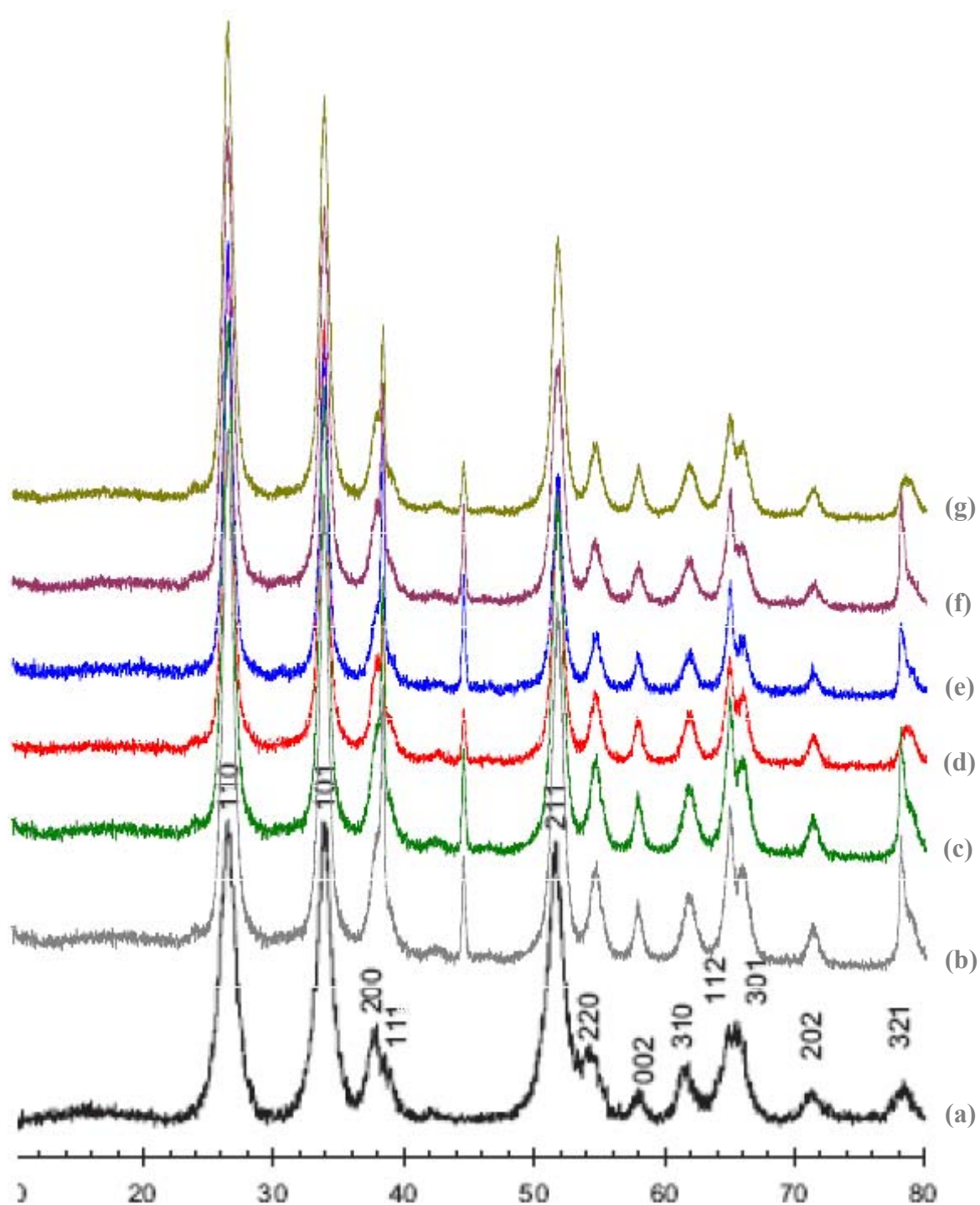
Figure C.1   Powder X-ray spectrums of (a) tin oxide theoretical curve, (b) absence of amines (**1**), (c) **2**, (d) **3**, (e) **4**, (f) **5** and (g) **6**.

APPENDIX D

SCANNING ELECTRON MICROSCOPY

The theoretical limit of the instrument's resolving power (R) can be determined by:[2]

$$R = \frac{\lambda}{2NA}$$

Where,

λ -   wavelength of electrons used

NA   -   numerical aperture

         (a measure of the e^n gathering ability of the objective
         or the e^n providing ability of the objective:
   normally engraved on each objective and condenser)
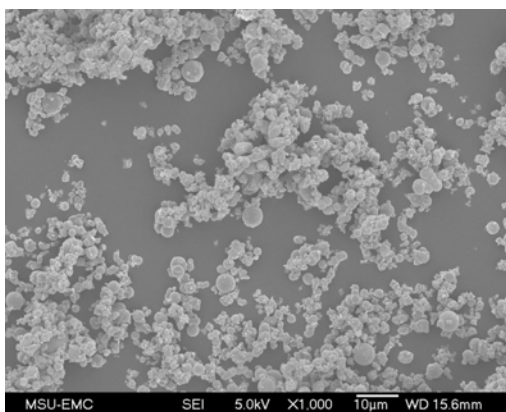
(a)
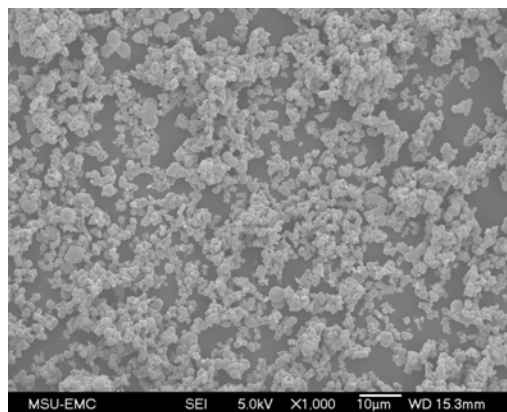
(b)
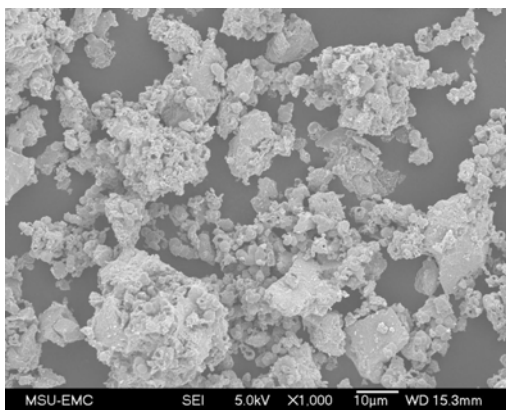
(c)
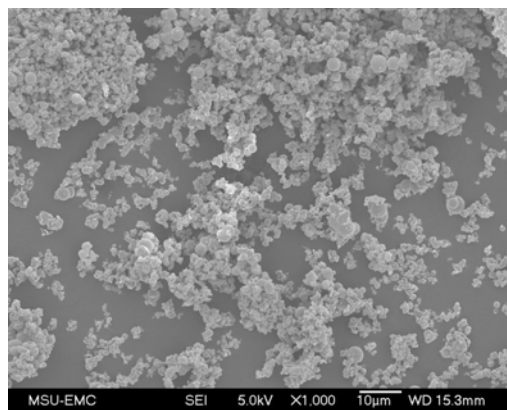
(d)
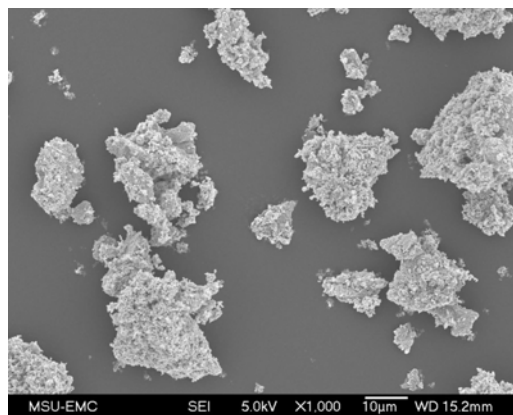
(e)

Figure D.1   SEM of products at 1,000× magnification with 20 mmol concentration, 250 °C temperature and 3 h oven time: (a) **2**, (b) **3**, (c) **4**, (d) **5** and (e) **6**.
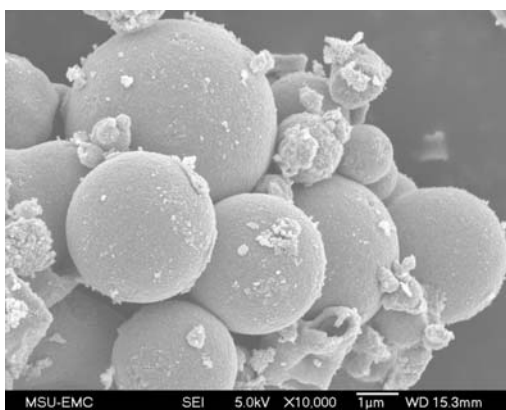
(a)
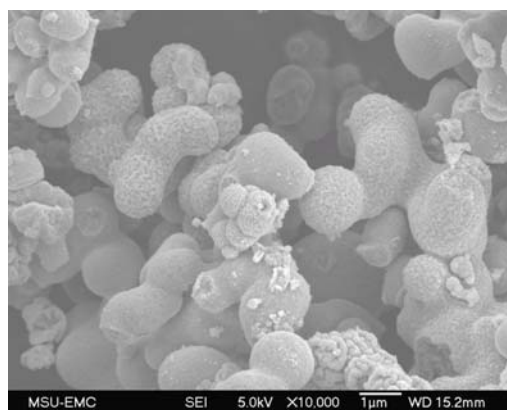
(b)
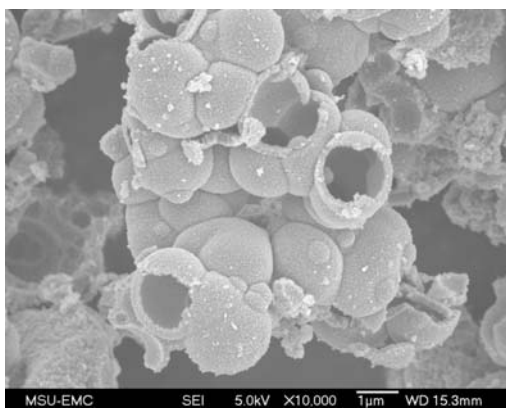
(c)
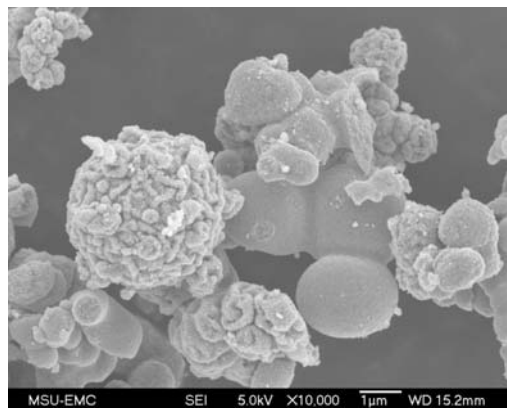
(d)
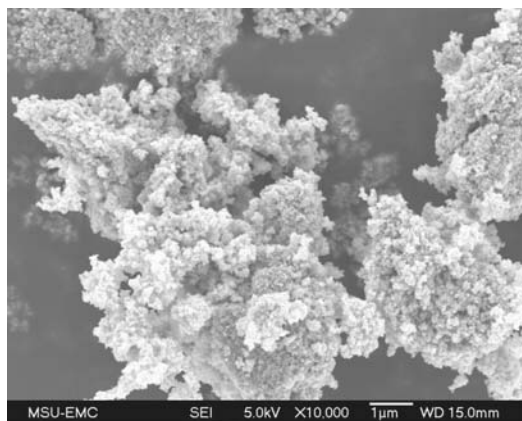
(e)

Figure D.2   SEM of products at 10,000× magnification with 20 mmol concentration, 250 ^{o}C temperature and 3 h oven time: (a)**2**, (b) **3**, (c) **4**, (d) **5** and (e) **6**.
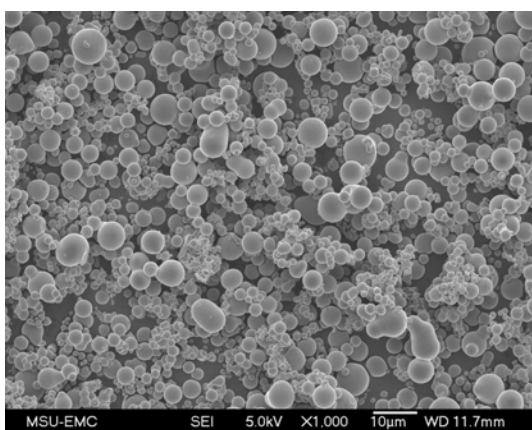
(a)
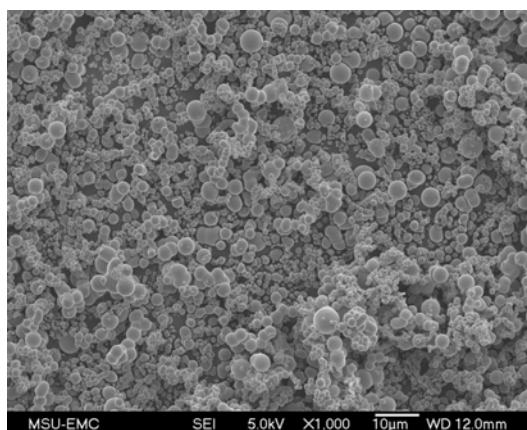
(b)
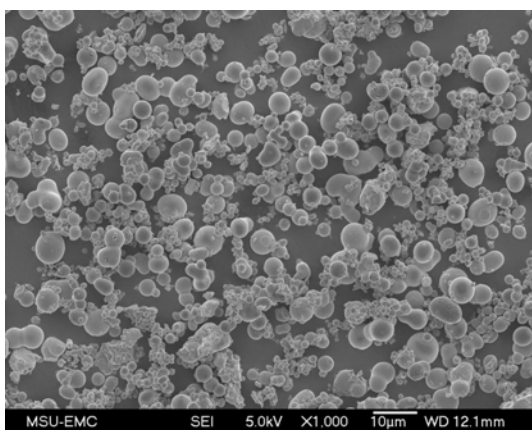
(c)
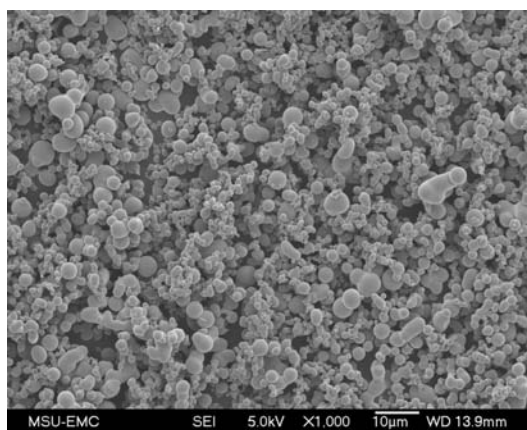
(d)

Figure D.3   SEM of products at 1,000× magnification with 20 h oven time, 4 mmol concentration, and 150 ^{o}C temperature: (a) **2**, (b) **3**, (c) **4** and (d) **5**.
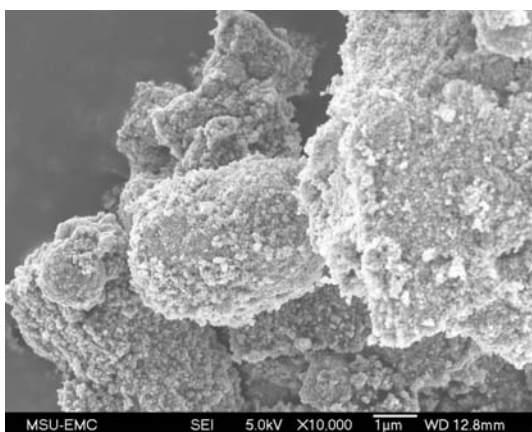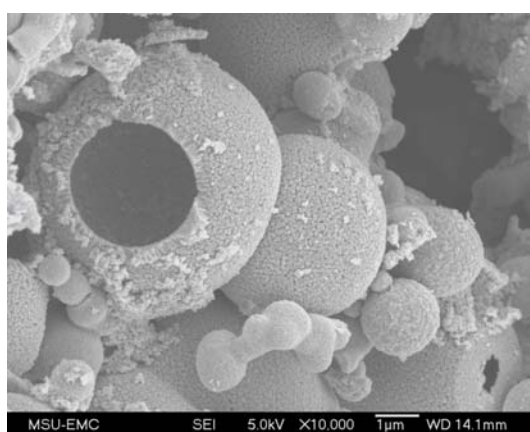
(a)

(b)

(c)

(d)

Figure D.4   SEM of products at 10,000× magnification with 20 h oven time, 4 mmol concentration and 150 ^{o}C temperature: (a) **2**, (b) **3**, (c) **4** and (d) **5**.
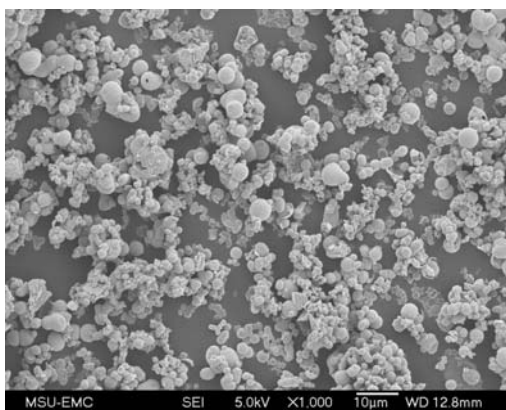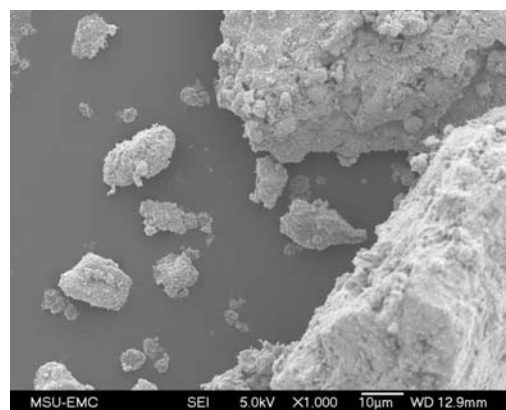
(a)

(b)

(c)

(d)

Figure D.5   SEM of products at 1,000× magnification with 67 h oven time, 4 mmol
concentration and 150 $^{\circ}$C temperature: (a) **2**, (b) **3**, (c) **4** and (d) **5**.
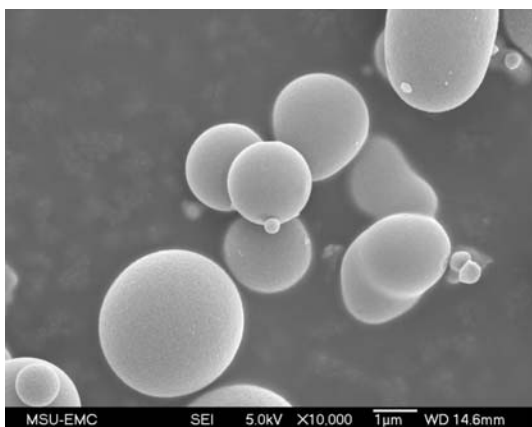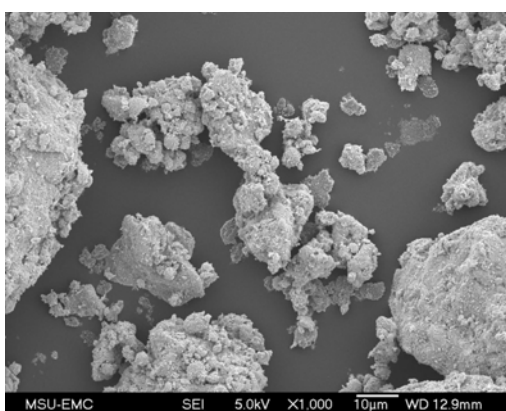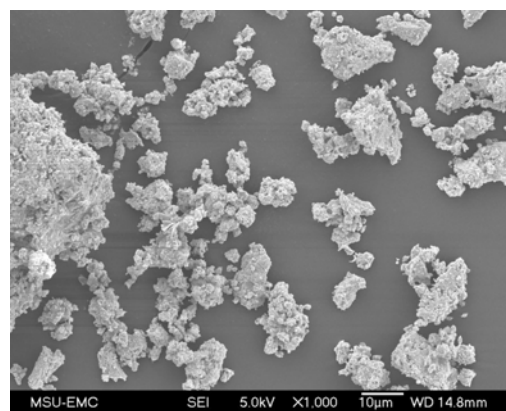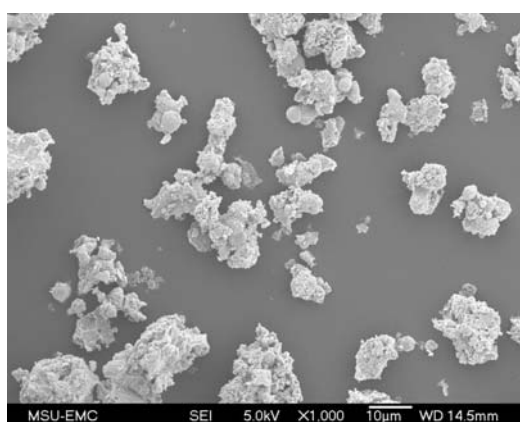
(a)
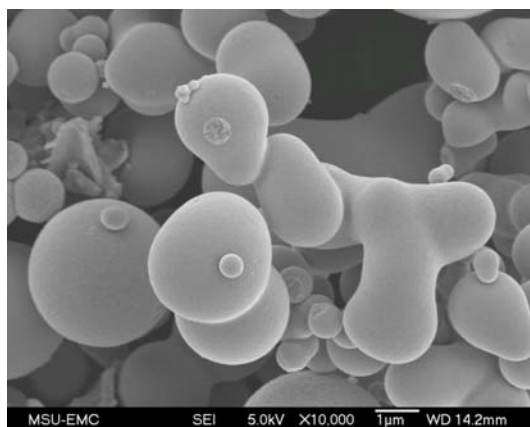
(b)
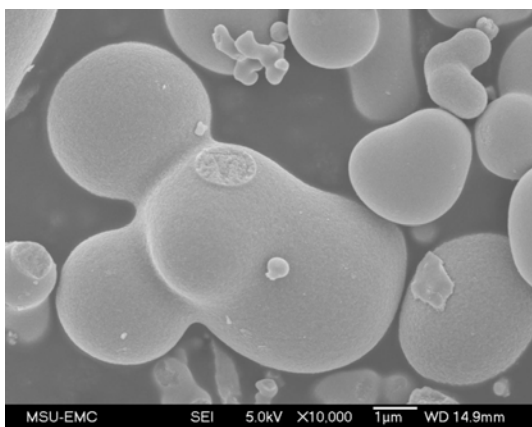
(c)
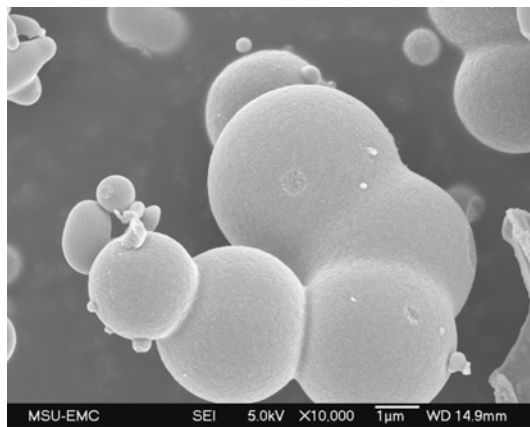
(d)

Figure D.6   SEM of products at 10,000× magnification with 67 h oven time, 4 mmol
             concentration and 150 ^{o}C temperature: (a) **2**, (b) **3**, (c) **4** and (d) **5**
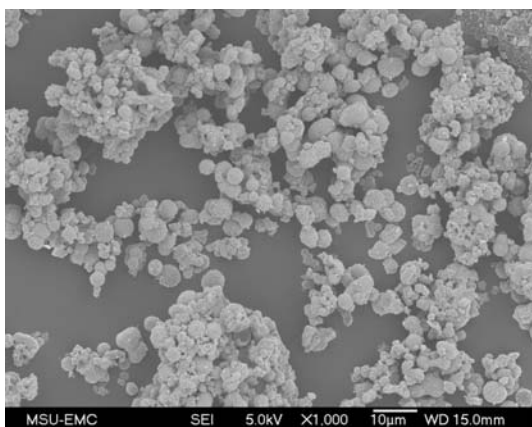
(a)
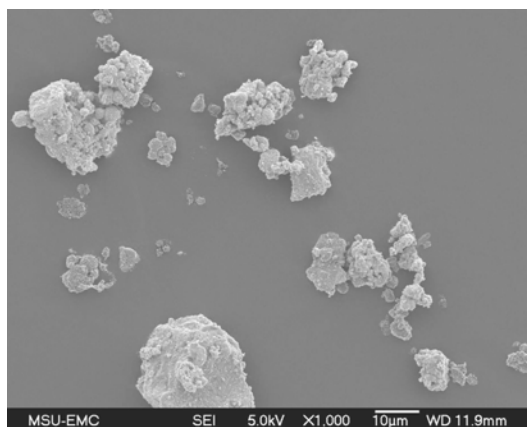
(b)
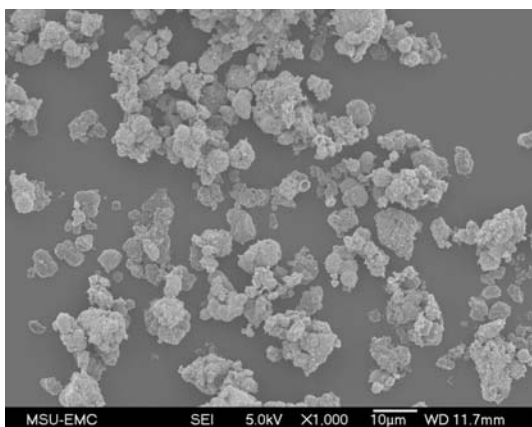
(c)
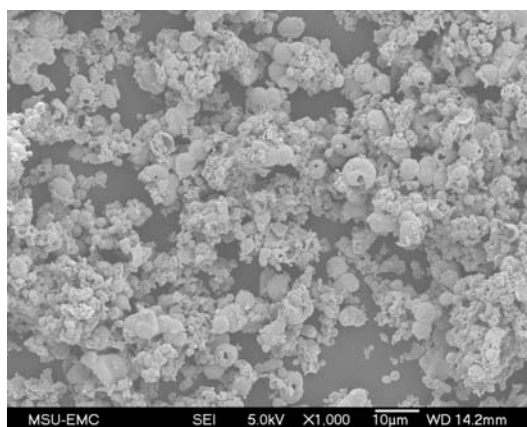
(d)

Figure D.7   SEM of products at 1,000× magnification with 20 h oven time, 4 mmol
            concentration and 250 ^{o}C temperature: (a) **2**, (b) **3,** (c) **4** and (d) **6**.
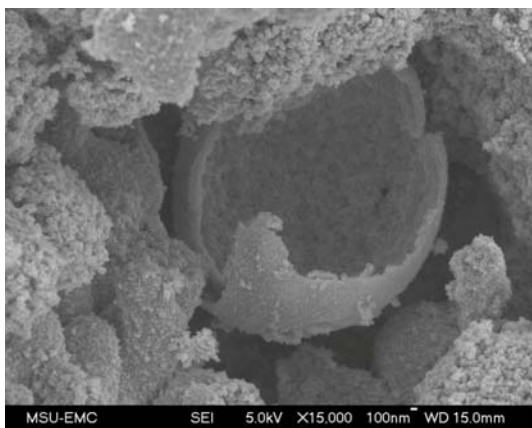
(a)
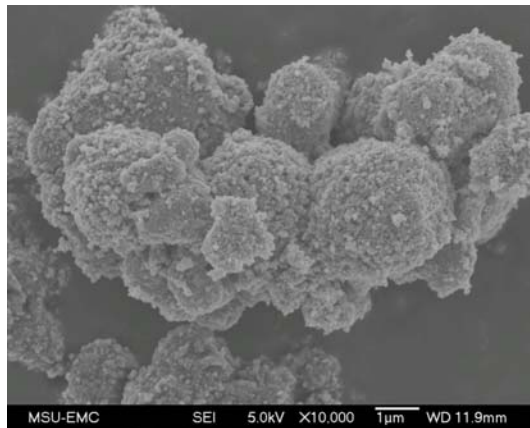
(b)

(c)

(d)

Figure D.8　　SEM of products at 10,000×/15,000× magnification with 20 h oven time, 4 mmol concentration, 250 ^{o}C temperature: (a) **2**, (b) **3,** (c) **4** and (d) **6**.
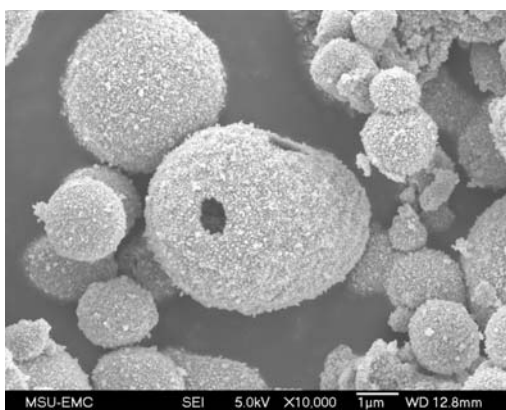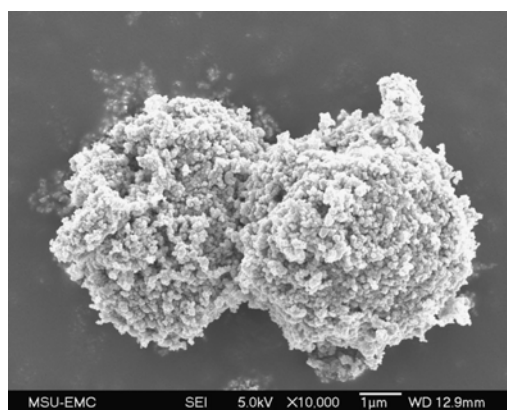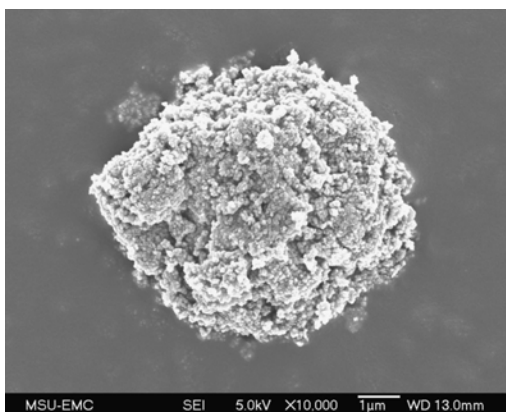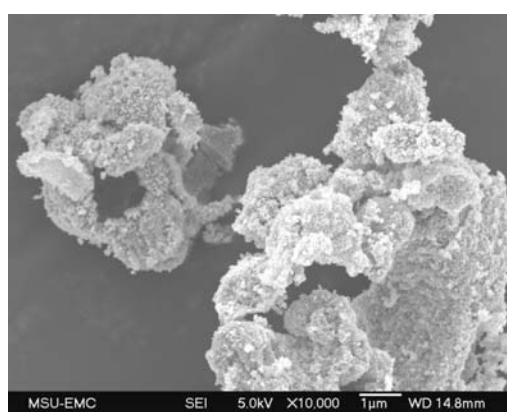
(a)

(b)

(c)

(d)

(e)

Figure D.9   SEM of products at 1,000× magnification with 67 h oven time, 4 mmol concentration, 250 $^{\circ}$C temperature: (a) **2**, (b) **3,** (c) **4,** (d) **5** and (e) **6**.
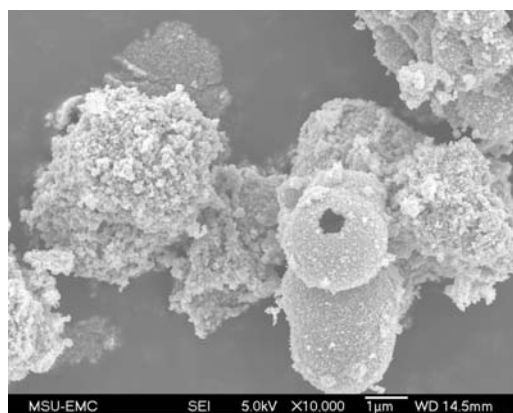
(a)

(b)

(c)

(d)

(e)

Figure D.10   SEM of products at 10,000× magnification with 67 h oven time, 4 mmol concentration, 250 $^{\circ}$C temperature: (a) **2**, (b) **3,** (c) **4,** (d) **5** and (e) **6**.

135

REFERENCES

(1)   Cao, G.; Editor *Nanostructures and Nanomaterials: Synthesis, Properties, and Applications*; Imperial College Press: London, 2004.

APPENDIX E

TRANSMISSION ELECTRON MICROSCOPY

de Broglie relation

The wave length (λ) of the electron can be calculated from de Broglie relation.[1]

$$\lambda = \frac{h}{mv}$$

Where,

$\quad$ h - Plank's constant $(6.6 \times 10^{-34} \text{ J s})$

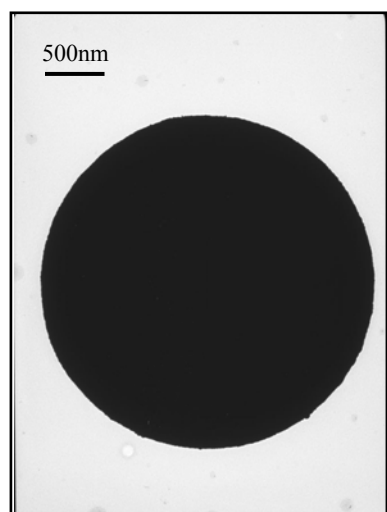$\quad$ m - mass of e^n

$\quad$ v - velocity of e^n

In TEM the wavelength (λ) of the accelerated electrons can be calculated from the following equation.[2]
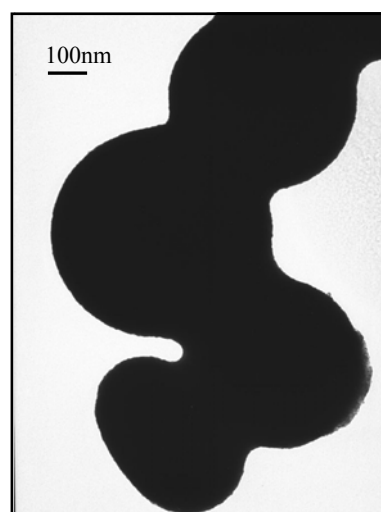
$$\lambda = \frac{h}{[2mqV]^{1/2}}$$
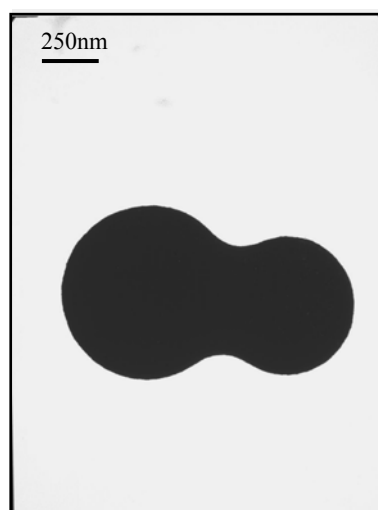
Where,

$\quad$ q - e^n charge

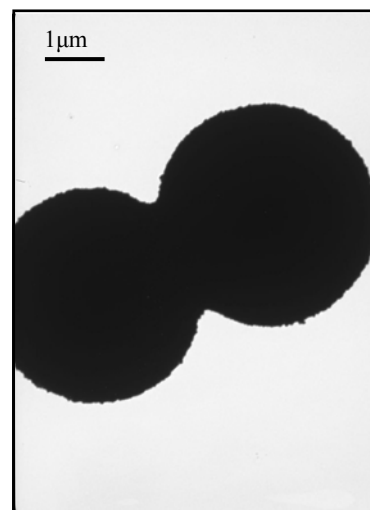$\quad$ V - potential difference through which e^{ns} are accelerated

(a)

(b)

(c)

(d)

Figure E.1   TEM bright field images (a) **2** (20,000×), (b) **3** (67,000×), (c) **4** (40,000×) and (d) **5** (10,000×).

REFERENCES

(1)   Atkins, P. W. *Physical Chemistry. 6rd Ed*; Oxford university Press: Oxford, 1998.

(2)   Cao, G.; Editor *Nanostructures and Nanomaterials: Synthesis, Properties, and Applications*; Imperial College Press: London, 2004.